UC Berkeley
UC Berkeley Electronic Theses and Dissertations

Title

Development of a Soft Gripper - Sensing, Actuation, and Controls

Permalink

https://escholarship.org/uc/item/2z70r12n

Author

YANG, WU-TE

Publication Date

2024

Peer reviewed|Thesis/dissertation

Development of a Soft Gripper - Sensing, Actuation, and Controls

By

Wu-Te Yang

A dissertation submitted in partial satisfaction of the

requirements for the degree of

Doctor of Philosophy

in

Engineering - Mechanical Engineering

in the

Graduate Division

of the

University of California, Berkeley

Committee in charge:

Professor Masayoshi Tomizuka, Chair
Professor Grace X. Gu
Professor Ronald S. Fearing

Fall 2024

Development of a Soft Gripper - Sensing, Actuation, and Controls

Abstract

Development of a Soft Gripper - Sensing, Actuation, and Controls

by

Wu-Te Yang

Doctor of Philosophy in Engineering - Mechanical Engineering

University of California, Berkeley

Professor Masayoshi Tomizuka, Chair

Soft robotics is an emerging field that offers adaptability and flexibility compared to rigid robots due to their inherent elasticity. Unlike rigid robots, soft robots exhibit distinct properties, kinematics and dynamics. This research, therefore, intends to introduce novel advancements in soft gripper design and control. Inspired by human skin, a dual-layer soft tactile sensor is proposed with pyramid-shaped sensing elements. It employs machine learning approaches to achieve superior sensitivity in detecting contact force, contact location, and other features. A novel design methodology for soft pneumatic actuators utilizes simplified cantilever beam approximations to develop kinematic and dynamic models. Model-based optimization design techniques are applied to determine optimal dimensional parameters, enhancing the actuator's properties such as force/torque, bendability, and controllability. To accurately capture nonlinear mechanical behavior, an alternative modeling approach using Ludwick's Law and data-driven parameter estimation is introduced and validated through experimentation. The approach optimizes the efficiency of parameter determination within dynamical models while improving accuracy. Addressing control challenges in under-actuated systems, this research explores coordination strategies for multiple soft actuators of a soft gripper, employing stable model inversion to a multi-finger soft gripper. Simulation and experimental validation demonstrate the effectiveness of this strategy in achieving precise and coordinated motions, thereby advancing the practical applicability of soft robots. Overall, these techniques aim to enhance the capabilities of current soft grippers, paving the way for their broader deployment in real-world scenarios.

To My Family and My Friends

Contents

List of Figures

List of Tables

Acknowledgments

I would like to express my sincere gratitude to my advisor, Professor Masayoshi Tomizuka, for his invaluable guidance throughout my research and the development of this thesis. His extensive experience and knowledge have significantly enhanced my work and my skills.

I am also deeply grateful to the members of my thesis committee, Professor Ronald Fearing and Professor Grace Gu, for their insightful and detailed feedback, which has greatly contributed to the refinement of my thesis.

My thanks extend to my research partner, Dr. Burak Kurkcu, for his expert advice on advanced control theories and research methodologies.

Additionally, I wish to acknowledge the support of lab members, Dr. Hsien-Chung Lin, Dr. Xinghao Zhu, Motohiro Hirao, and Boyuan Liang. Their assistance in conducting experiments and addressing research challenges was instrumental in the smooth progression of my work.

Lastly, I appreciate the encouragement and support from my supervisors of summer internship at ASML, Dr. Yi Zhao and Dr. Iman Khademi, whose emphasis on developing soft skills has been crucial for my professional growth.

Chapter 1

Introduction

1.1 Motivation

Soft matters are ubiquitous in people's daily lives, offering adaptability and comfort across a spectrum of human-made objects and natural organisms. From the plush cushions of sofas and beds that contour to our bodies, providing incomparable comfort, to the elastic resilience of rubber bands that securely wrap packages of diverse sizes, softness is deliberately engineered to enhance usability. Yet, beyond human design, nature exhibits a mastery of softness for survival and versatility. Consider the dexterous elephant trunk [93], endowed with remarkable flexibility, enabling the gentle giant to manipulate objects of various shapes and sizes deftly. Or the octopus can morph its body to fit multiple environments underwater [61]. Similarly, the human body [19], a marvel of biological engineering, boasts its soft structures. With their supple skin and agile joints, human hands empower humans to undertake an array of intricate tasks—from the precision of cooking and writing to the intricacies of artistic expression.

Referencing the advantages of soft matters, soft robotics, a new field at the intersection of engineering, materials science, and biology, has emerged as a revolutionary approach to designing and controlling robotic systems [51]. Unlike their traditional rigid counterparts, soft robots are composed of compliant materials that mimic the flexibility and adaptability of biological organisms. Soft matter's power lies in its ability to adapt to natural environments and its potential to revolutionize various industries, from healthcare to manufacturing. Soft robots provide a new solution to existing challenges.

Imagine a world where robots can safely interact with humans, navigate complex environments with ease, and perform delicate tasks with precision like humans. This vision is becoming closer to reality thanks to advancements in soft robotics research. By harnessing the unique properties of soft materials such as elastomers, hydrogels, and shape-memory polymers, engineers are pushing the boundaries of what is possible in robotics. Soft technology will empower robots and make them more intelligent.

The motivation behind this research stems from the recognition of the limitations of tra-

ditional rigid robotics and the desire to overcome them. While rigid robots excel in controlled environments and structured tasks, they often struggle in unstructured environments where flexibility and adaptability are important. Soft robots offer a solution to this challenge by providing inherent compliance and deformability, allowing them to navigate unknown environments, interact safely with humans, and manipulate delicate objects with fitness [51].

Moreover, the potential applications of soft robotics are diverse. In production lines, they offer new possibilities for agile and reconfigurable automation [141]. In exploration and rescue missions, they can explore challenging terrains and navigate confined spaces with ease, aiding in disaster response efforts [72]. In healthcare, soft robots hold promise for minimally invasive surgeries, targeted drug delivery, and rehabilitation therapies [1]. In the industry, soft hands show the potential to manipulate fragile objects or interact safely with humans [86].

With this background, this dissertation explores novel design and control approaches for soft sensing, actuation, and control to advance soft robots. The potential of soft robotics and inspired future research endeavors in this exciting field are showcased and discussed through theoretical insights, experimental demonstrations, and real-world applications. This dissertation research makes four key contributions: 1) the development of a multifunctional soft tactile sensor, 2) the optimal model-based design of a soft pneumatic actuator, 3) the mathematical modeling of the soft pneumatic actuator described in 2), and 4) an underactuated control algorithm for coordinating multiple soft fingers within a soft gripper.

1.2 Contributions

The research of traditional robots made of metals began around the 1960s [18]. Till now, conventional robots have relatively mature technologies of sensing, actuation, and controls. By contrast, soft robots are getting popularity during recent years [118, 117], and related technologies such as soft sensors, soft actuators, and control algorithms are under development [139]. Since soft materials have different properties than metals, new technologies are required. For instance, soft materials are significantly softer than metals [28]. Softness is quantified by Young's modulus [105], which for soft materials typically falls within the megapascals (MPa) range, while for metals it is measured in gigapascals (GPa). As a result, the mechanical properties of these materials differ markedly, leading to distinct dynamic behaviors in soft robots compared to their rigid counterparts. Additionally, soft materials often display nonlinearity and uncertainty due to their complex microstructures [23]. Addressing these challenges involves exploring novel design frameworks, modeling approaches, and control algorithms. This thesis advances the field of soft robotics through contributions in several key areas: the design of soft tactile sensors, the development of soft pneumatic actuators, mathematical modeling of these actuators, and the control of soft actuators. Detailed information on these contributions is presented below.

Soft Tactile Sensor Design

Sensing plays an essential role for robots, including soft robots, since sensing helps robots interact with the environments and make suitable decisions [19]. Several soft sensors are developed during the past ten years [20, 63, 27, 49]; however, the sensor design techniques can be further improved such as functions, sensing range, sensitivity, etc. The developed soft sensor usually focuses on a single function, such as detecting contact force, contact position, or contact features. The multifunctional soft tactile sensors that integrate various functions are seldom discussed and studied.

A multimodal soft tactile sensor design method is proposed in this thesis. Inspired by multifunctional human skin, the proposed design has a dual-layer structure. The top layer consists of a group of sensing elements that detect the contact location and contact feature enhanced by the bagging classifier based on the k-nearest neighbors. The sensor elements are biomimetically and analytically designed as a pyramid shape that mimics the mountain ridge-like structure in human skin to improve sensitivity. The bottom layer is made of a piece of Velostat sandwiched between conductive fabrics that can measure the contact force. The relationship between the sensing voltage and the contact force is modeled by the Nadaraya–Watson regressor. A repeatability test verifies the performance of the proposed sensor. Furthermore, the effectiveness of the proposed sensor on a robotic gripper is demonstrated. The experimental results show that this sensor can detect contact information of fragile objects.

Soft Actuator Design

Actuators generate robot motions. Traditional robots rely on electrical actuators such as motors to generate their motions. By contrast, soft robots count on soft actuators. There are a wide variety of soft actuators such as electroactive polymers, cable-driven, shape memory alloy, and pneumatic actuators [133]. Soft pneumatic actuators are favorable for building soft robotic systems because they are lightweight, low-cost, and provide high power density. The common design strategies [67, 65, 22, 87] usually consider single metric, either force/torque or bending angle. Furthermore, the dynamic properties are seldom discussed.

A novel design approach for soft pneumatic actuators (SPAs) is presented. The soft actuators' kinematic and dynamic models are built based on an approximation structure of the soft pneumatic actuator. The kinematic models can predict force, torque, and bending angle in response to varying pressures. The complex structure of the soft actuator is simplified by approximating it as a cantilever beam. This allows for deriving approximated nonlinear kinematic models and a dynamical model, which is explored to understand the correlation between natural frequency and dimensional parameters of SPAs. The design problem is then formulated as an optimization problem, where the kinematic equations serve as the objective function, and the dynamic equations are treated as constraints. By solving this optimization problem, the optimal dimensional parameters are determined. Six prototypes are manufactured to validate the proposed approach. The optimal soft actuator successfully generates

the desired force/torque and bending angle while its natural frequency remains within the constrained range. This project highlights the potential of using optimization formulation and approximated nonlinear models to improve soft pneumatic actuators' performance and dynamical properties.

Soft Robot Modeling

As soft robots' dynamics differ, novel modeling approaches are needed to describe their motions. The hyperelastic theories [84, 7, 4] are commonly adopted to model soft materials and soft robots. The hyperelastic models [62] exhibit high accuracy; however, they contain unknown parameters to be determined. Tensile tests are conducted to obtain the unknown parameters. The process usually consumes time and effort, and the tensile test machines, which are high-cost, are necessary to do the tests.

This project aims to suggest an alternative modeling approach that saves time and effort but maintains certain levels of accuracy. The research begins by introducing Ludwick's Law, providing a more accurate representation of the complex mechanical behavior exhibited by soft materials. Three key material properties, namely Young's modulus, tensile stress, and mixed viscosity, are utilized to estimate the parameter inside the nonlinear model using the least squares method. Subsequently, a nonlinear dynamic model for soft actuators is constructed by applying Ludwick's Law. The nonlinear model and Ludwick's Law can be simplified and degraded to the linear model and Hooke's Law. Experimental validations are performed to validate the proposed method's accuracy and effectiveness. Several experiments are conducted to demonstrate the model's capabilities in predicting the dynamical behavior of soft pneumatic actuators. This project contributes to advancing soft pneumatic actuator modeling that represents their nonlinear behavior.

Underactuated Control of Soft Robots

The motions of soft robots are usually slower than those of rigid robots. Also, soft robots tend to show uncertain motions due to the properties of soft materials [51, 28]. Some researchers developed reliable open-loop control strategies for soft robots, but limitations exist, such as noise and disturbance rejections [104]. To improve those issues, closed-loop control algorithms play a role in stabilizing the dynamics of soft robots. Several existing control methods are applied to control soft robots [96, 97, 95, 99, 130, 8]. Nonetheless, the underactuated control strategies are rarely mentioned and applied to soft robots [46].

This project introduces a novel approach to underactuated control of multiple soft actuators and experimentally verifying the effects of actuator uncertainties. This approach focuses on coordinating soft fingers within a soft gripper, using a single syringe pump as the actuation mechanism. The challenge of coordinating multiple degrees of freedom of a compliant system is addressed. The theoretical framework applies concepts from stable model inversion, adapting them to the unique dynamics of the underactuated soft gripper. Through meticulous mechatronic system design and controller synthesis, the efficacy and

applicability of this approach in achieving precise and coordinated manipulation tasks are verified in simulation and experimentation. Additionally, several experiments are conducted to explore the impact of parameter-varying uncertainties in soft actuators. These findings advance the field of soft robot control and provide practical insights into the design and control of underactuated systems, enhancing their applicability to real-world scenarios.

1.3 Dissertation Outline

The rest of this dissertation is organized as follows. Chapter 2 will present the design of a soft tactile sensor by bio-inspired strategies and machine learning approaches. Chapter 3 will introduce the optimal design of a soft pneumatic actuator considering both kinematic and dynamic during the mechanical design stage. Chapter 4 will discuss the design, modeling, and parametric analysis of a syringe pump used to drive the soft actuators designed in Chapter 3. Chapter 5 will display the linear and nonlinear modeling methods for the soft actuators in Chapter 3 via a data-driven parameter estimation. Chapter 6 will demonstrate underactuated control of multiple soft fingers within a soft gripper to achieve coordinated motions for reliable grasping tasks. The underactuated control of the soft fingers is achieved via stable model inversion. Chapter 7 will conclude this dissertation's primary results and contributions. Potential extensions of work will also be discussed.
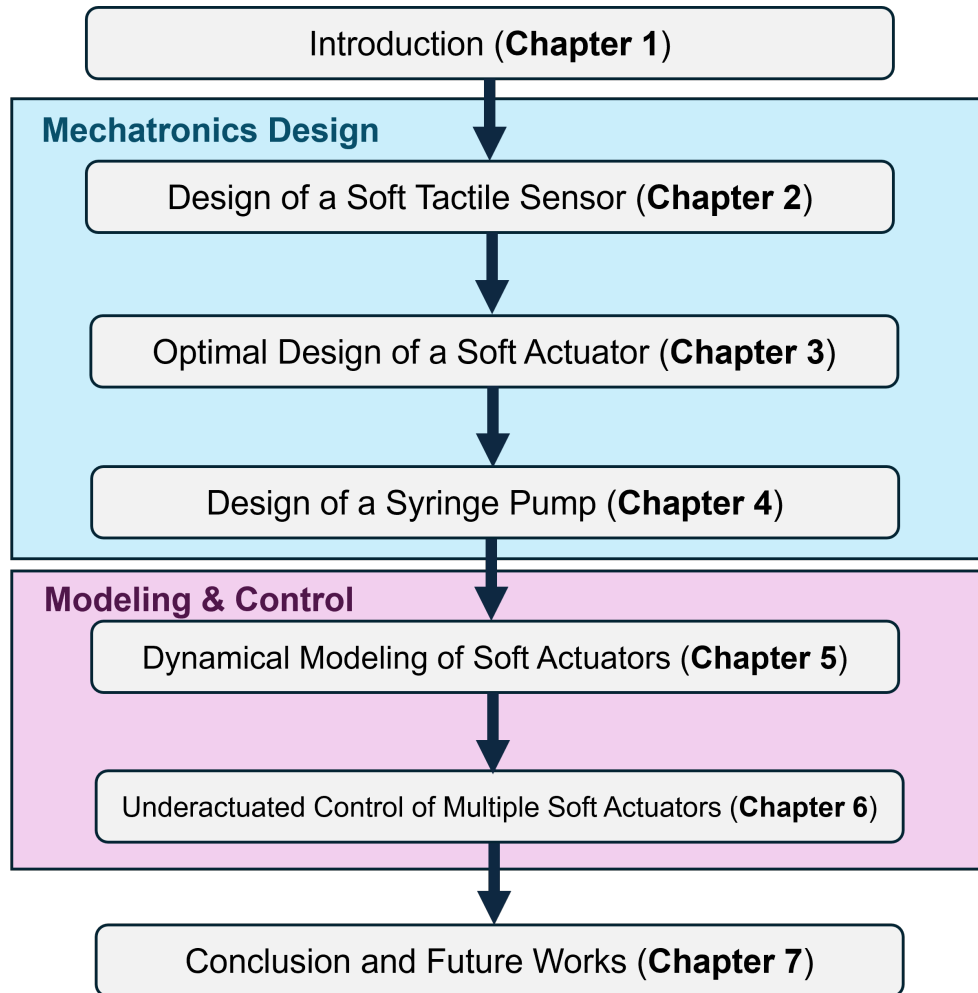
Figure 1.1: The framework of this dissertation.

Chapter 2

Design of a Multifunctional Soft Tactile Sensor

2.1 Introduction

Soft tactile sensors play a crucial role in soft robotics, enabling robots to sense and respond to delicate forces and pressures, much like human touch. This sensitivity is vital for tasks that require gentle manipulation of objects, such as handling fragile items or interacting safely with humans. The practical applications of these sensors are far-reaching, reducing the risk of damage or injury during interactions between robots and sensitive materials and improving safety in collaborative robotics applications. The importance and advantages of soft sensing have led to the initiation of this thesis project, which begins with the design of a soft tactile sensor.

This chapter focuses on designing a multifunctional soft tactile sensor that detects contact force, contact point, and contact features (i.e., point contact, line contact, and surface contact). The sensor is inspired by human skin and is designed to have a dual layer. In the dual-layer structure, the top layer is equipped with several pyramid-shaped sensor elements that mimic the mountain ridge-like structures in the dermis layer of skin to enhance sensitivity [132, 82, 140]. The sensitivity of the top layer is a crucial issue since it determines the ability of the sensor to react to the minimum force [19]. The pyramid shape elements are designed analytically by applying contact mechanics theories [32, 13] and validated to increase the sensitivity by finite element simulation and experimental tests. The bottom layer, consisting of a Velostat sandwiched between two pieces of conductive fabric, detects the contact force. Owing to the structure and nonlinearity of the design, machine learning approaches offer convenient solutions to model the sensor [6, 83, 102, 123, 69, 103, 44] and even augment the sensor's performance [124, 135]. This sensor design lacks functional algorithms for the top layer to identify contact features efficiently, so the bagging classifier is implemented to categorize the contact features with a classification rate of 96.25 %. The traditional regression method with feature engineering techniques fails to accurately model

the nonlinear relationship between sensing voltage and contact force in the bottom layer. Hence, it is modeled by the nonparametric technique, Nadaraya–Watson regressor, which achieves 95.4% average accuracy.

Several related multifunctional sensors have been developed in previous works. This research is inspired by [94], which included modes in a single sensor and had a multi-layer structure. De-Oliveira et al. [20] proposed a skin-inspired multimodal tactile sensor that perceived rich information by integrating multiple sensing units. In this study, the sensor features fewer sensing units and a more straightforward structure, yet it effectively captures tactile information through augmentation with machine learning algorithms. Li et al. [63] presented a similar design but worked differently. The multi-layer tactile sensor captured contact force and object temperature, fused by a neural network to determine object sizes, shapes, and materials. Integrating multiple sensors into a humanoid robotic hand achieved a certain level of accuracy, but this design enabled independent and accurate identification of contact points, geometric features, and contact force. In addition, both Drimus et al. [27] and Hughes et al. [49] developed multifunctional soft sensors by adopting similar design concepts. The former work dealt with the classification of rigid and flexible objects, while the latter addressed the applications of medical palpation. This work, however, emphasizes detecting richer tactile information of fragile or irregular-shaped objects, so it helps robotic hands identify characteristics of the objects and achieve stable grasping.

The rest of this chapter is organized as follows. Section 2.2 describes the design and fabrication of the soft sensor. Section 2.3 models the behavior of the sensor by machine learning methods. Section 2.4 demonstrates the experimental results of the soft sensor, and Section 2.5 concludes the work.

2.2   Design and Fabrication of Soft Sensor

Humans are successful in dealing with dexterous manipulation tasks because the human skin contains several types of delicate sensory receptors, including Meissner's, Pacinian, and Merkel's corpuscle, which detect light contact, vibration force, and object features as shown in Figure 2.1. Good touch sensitivity facilitates human hands to grasp unknown objects, identify their geometric features, and detect contact positions even without vision [19]. Imitating the structure of human skin, the proposed soft tactile sensor is multifunctional and is composed of two layers. The top layer of the sensor mimics the top dermis layer inside human skin as in Figure 2.1, where Merkel's and Meissner's corpuscles are located. The bottom layer references the bottom dermis layer where the Pacinian corpuscles are situated. The top layer is named the feature-detection layer, while the bottom layer is called the force-measurement layer.

The design of the sensor is shown in Figure 2.2. The feature-detection layer contains eight sensing elements as Figure 2.2 (a). The force-measurement layer has a piece of Velostat sandwiched by two pieces of conductive fabric. The appearance of the sensor is illustrated in Figure 2.2 (b). More design concepts are discussed below.
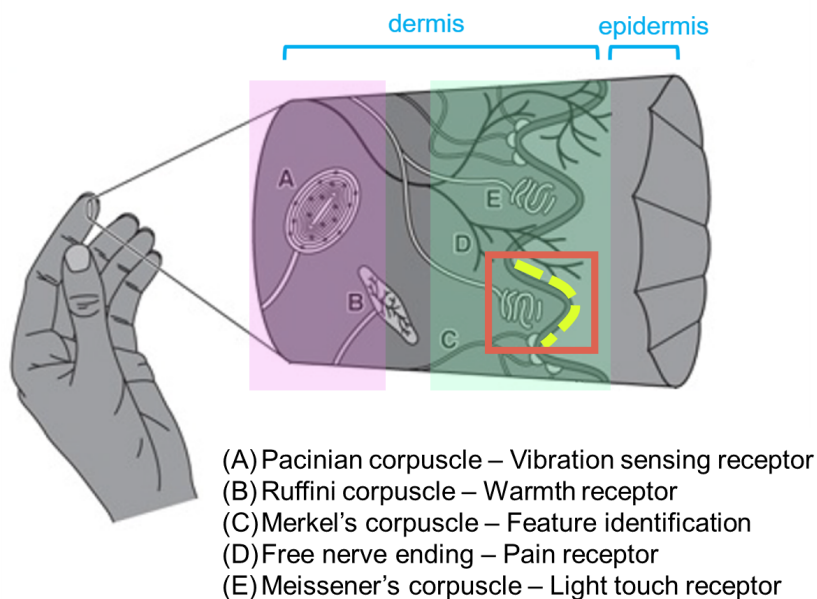
Figure 2.1: Human skin structure contains mountain ridge structures in the dermis layer as the yellow dashed line in the red rectangle and the descriptions of the functions of the mechanoreceptors are shown in (A)–(E) [52, 115]. In the proposed design, the feature-detection layer mimics the top dermis layer as the green highlighted area. In contrast, the force-measurement layer references the bottom dermis layer as the pink highlighted area.

Design of Feature-Detection Layer

The feature-detection layer intends to get local contact information such as contact locations, object poses, and contact features (i.e., point contact, line contact, etc.) The feature-detection layer comprises a sensor array of eight silicone rubber sensing elements, as shown in Figure 2.2 (a). They are designed as pyramid shapes to detect contact sensitively. The sensor array layout is inspired by Merkel's corpuscles, which are widely distributed inside human skin to detect static touch features [52]. The number of sensing elements is determined through experimental testing. These eight elements have been shown to detect desired contact features effectively, and the design is scalable for various applications, such as serving as the skin for robot manipulators.

The sensor elements are made of the liquid rubber, Smooth-on Ecoflex® 00-30, with conductive ink painted outside the surface as discussed in Section 2.3. The ink painted on the surface of the element is like a conductive surface, as demonstrated in Figure 2.3 (a). The carbon powders distribute on the element's surface and form a conductive channel, so the element becomes a resistive sensor. When the element distorts, the conductive channel on the surface would be squeezed and deformed. The conductivity of the channel, in turn,
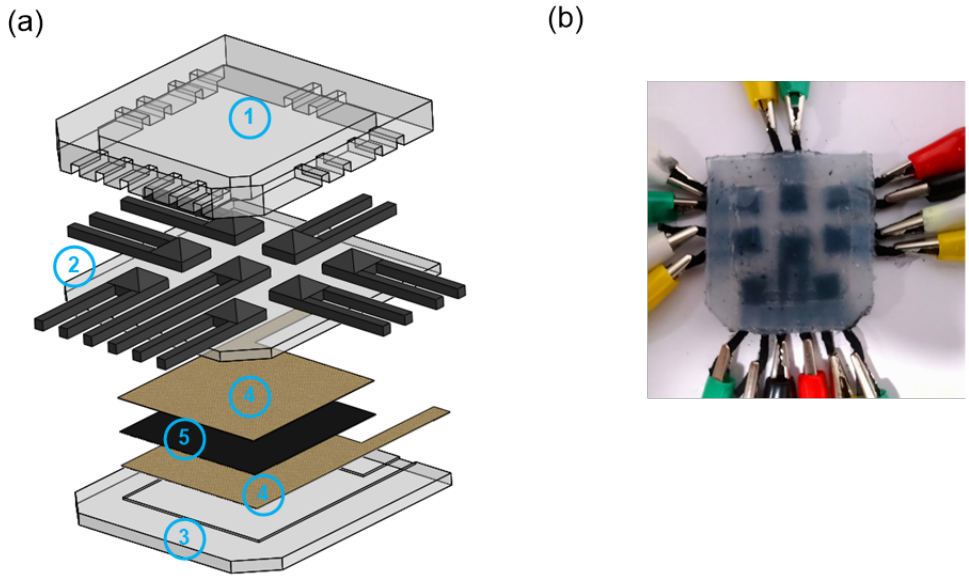
Figure 2.2: Structure of the soft tactile sensor is displayed in (a). Components labeled 1, 2, and 3 are made of liquid rubber with different molds. Components 4 and 5 are the conductive fabric, and Velostat is placed on component 3. The finished sensor is demonstrated in (b).

is influenced by the loadings and deformations. As the contact force and deformation rise, the resistance increases.

Following this design principle, the objective is to enhance the sensitivity (minimum detectable force) of the sensing element under identical loading conditions. It is observed that human skin is quite sensitive since it has mountain ridge-like structures in the dermis, as shown in Figure 2.1 (red rectangle). The ridge structures have been proven to amplify the contact force and increase skin sensitivity [132, 39, 82, 140]. Thus, the proposed design mimics the structure of human skin. A couple of different shapes of sensor elements are studied and tested to confirm the optimal design.

The geometric shape of the sensing element is designed based on its behaviors under loadings. The deformability of the sensing element under the same loading will influence its sensitivity. Therefore, three different shapes are considered, including cylinder, hemisphere, and pyramid shapes, which reference the ridge structures in human skin as in Figure 2.1. Generally, their deformations under loadings are described by

$$d\delta = \int_0^L \frac{F}{EA(y)} dy \tag{2.1}$$
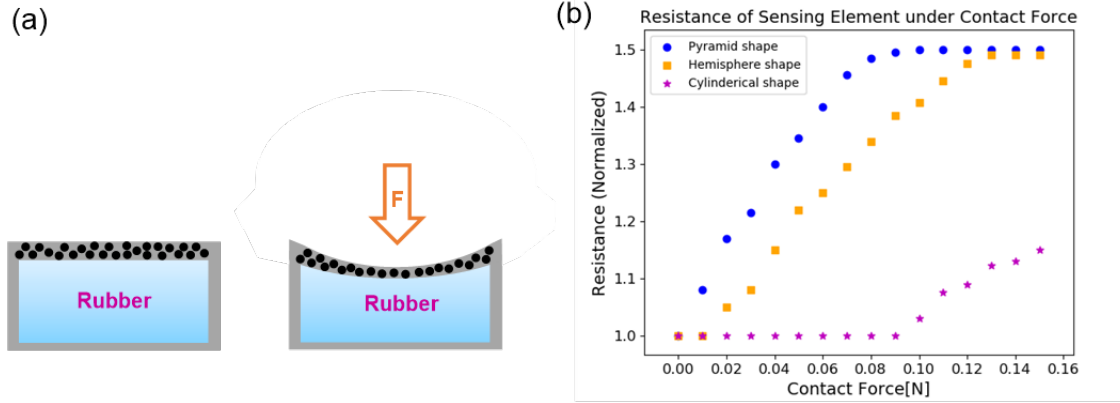
Figure 2.3: The sensing element is painted with conductive ink (gray color) outside its surface in (a). The top surface illustrates the distribution of carbon powders, which form a conductive channel. As the element is under loading, the conductive channel will deform and influence its resistance. The resistance changes of sensing elements under consecutive loadings are displayed in (b).

where $d\delta$ is the displacement of the sensing element under loading, F is the applied force, E is Young's modulus, L is the height of the element, and $A(y)$ is the cross-sectional area of the sensing element [13]. (The $A(y)$ of pyramid shape element is $(w - wy/L)^2$ and that of hemisphere shape is $((w/2)^2 - y^2)$ as shown in Figure 2.4).
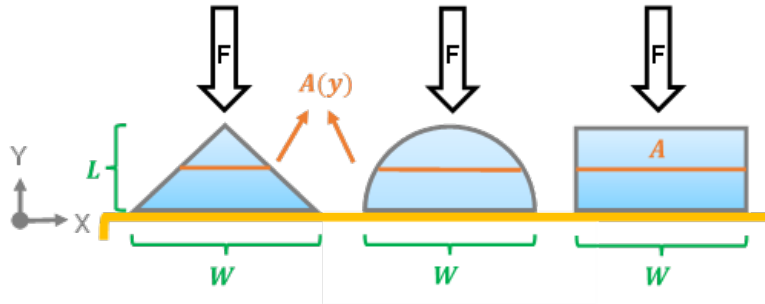
Figure 2.4: The schematic of different sensing elements of the soft sensor under loading F. The height and width of the element are L and W, and its cross-sectional area is $A(y)$.

The deformation of the hemisphere element can also be determined by the Hertzian contact model [32]

$$d = \left[\frac{3F}{4\sqrt{w}}\left(\frac{1 - v^2}{E}\right)\right] \qquad (2.2)$$

where d is the deformation along the direction of force, and w is the radius of the hemisphere element.

To further analyze the deformation under loadings, ANSYS (Release ANSYS Student 2020 R2) is utilized to simulate the behaviors of elements under various contact forces as displayed in Figure 2.5. The models are meshed by tetrahedron cells for the hemisphere shape element and hexahedron cells for cylinder and pyramid shape elements. The loads are applied at the top surface, and the bottom surface is fixed as the boundary condition for each element. The compliant material is assumed to be the isotropic linear elastic model. As the loadings are relatively small in the simulation, the linear model achieves good approximations, and the rubber behaves linearly [47]. The elastic modulus and Poisson's ratio of Smooth-on Ecoflex® 00-30 are set as 0.125 MPa and 0.49 [84].
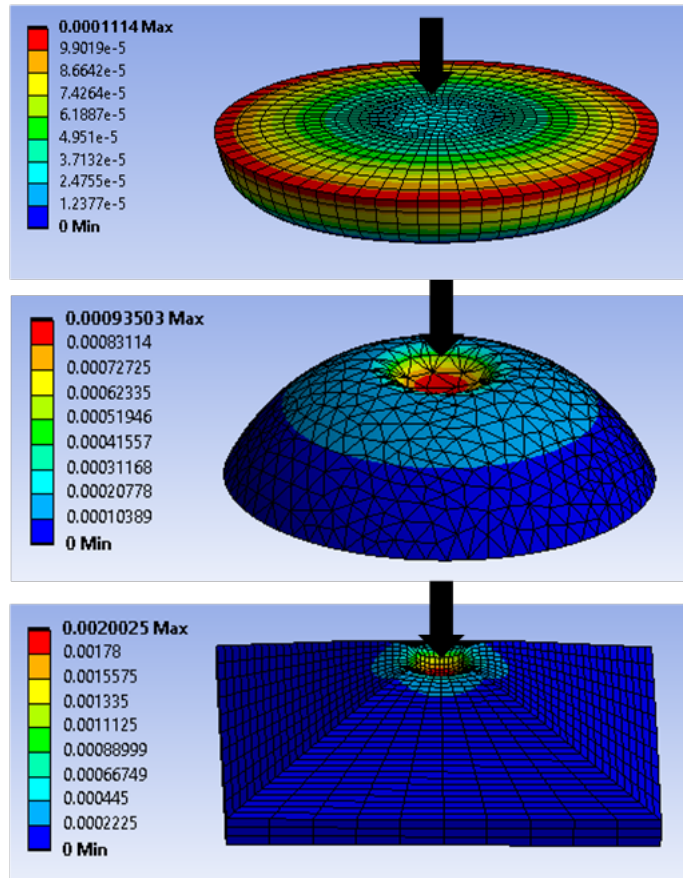
Figure 2.5: Finite element analysis of cylinder, hemisphere, and pyramid shape elements under loading. The color bar at the left of each subplot shows the deformation of each element (unit: m).

The simulation and analytical results are given in Table 2.1. The elements are under a

set of small contact forces, 0.1, 0.2, and 0.3 N. The table illustrates that the pyramid shape element had the most considerable deformation with the same loading, and its resistance change is expected to be the most responsive. By contrast, the deformation of the cylinder shape element is negligible, and so is its sensitivity. In the experimental test, the resistance responses of the sensor element are obtained to verify that the deformation influences the resistance. Thus, the experiment of the loadings versus resistance changes for different element structures is represented in Figure 2.3 (b). Since the deformation is proportional to the loading based on (2.1) and (2.2), the resistance value changes as the deformation or loading increases. The resistance of the sensing elements varied from 1 M to 1.5 $M\Omega$ in this design. The sensitivity of pyramid, hemisphere, and cylinder shapes are 0.01, 0.02, and 0.1 N, respectively, according to the test. The pyramid-shaped element has the best sensitivity and reacts actively to the loading changes. The experimental results matched the design principle that the deformation exhibits a relationship to the resistance change of conductive rubber. Note that the sensitivity is measured when the amplifying circuit is in a high gain. The value is the minimum force each element can perceive, respectively.

Table 2.1: Simulation and analytical results of the sensor element with different shapes.

Shape	Methods	0.1 N	0.2 N	0.3 N
Cylinder (mm)	FEM	0.037	0.074	0.111
	Analytics	0.038	0.076	0.115
Hemisphere (mm)	FEM	0.312	0.623	0.935
	Analytics	0.334	0.669	1.003
	Hertzian	0.477	0.757	0.991
Pyramid (mm)	FEM	0.667	1.335	2.003
	Analytics	0.694	1.389	2.083

Design of Force-Measurement Layer

The force-measurement layer is made of two pieces of conductive fabric sandwiching a piece of Velostat as shown in Figure 2.2 (a). This layer is inspired by the Pacinian corpuscle shown in Figure 2.1, which can detect vibration forces [52, 115]. The Velostat is made of polymeric foil impregnated with carbon black, so it becomes electrically conductive. The conductive fabrics and the Velostat form a resistive sensor. When there is no contact force, the resistance is relatively large. On the other hand, the resistance will reduce if a contact force is applied to the sensor. This property could be used to measure contact force, where the contact force is proportional to the sensing voltages. The current sensing range of the force-measurement layer is 0.7 N. The sensing range can be adjusted by increasing the thickness of the Velostat during the fabrication stage. For instance, by sandwiching two pieces of Velostat between the conductive fabric, the sensing range is increased to 1.3 N. In this design, the sensing

range of 0.7 N is selected since it satisfies the requirements of several grasping tasks with the high frictional coefficient of soft material [75].

Testing also included a single piece of conductive fabric as the bottom layer of the sensor. Since the material is the same as the previous one, they share a similar behavior, i.e., the larger the contact force, the larger the resistance of the sensor. However, the original design has poor repeatability, where the estimated force would vary significantly, and the standard deviation of measurements would go beyond 0.05 N easily. Hence, the force-measurement layer is designed as a sandwich structure, which improves the sensor's repeatability, and the deviation of measurements has been reduced to an average of 0.015 N as discussed in Section 2.2. In addition, the feature-detection layer could measure contact force, but its sensing range is too narrow and might be inaccurate. The 0.1–0.2 N hit the ceiling, and the measurement errors could go beyond ten % as the contact force is close to the upper limit of the sensing range.

Fabrication of Soft Sensor

The structure of the proposed soft tactile sensor is shown in Figure 2.2. The sensor body is primarily made of liquid rubber, Smooth-on Ecoflex® 00-30, by manually mixing part A and part B with a 1 to 1 ratio in weight. The cure time is 2 hr at room temperature. Components 1, 2, and 3 in Figure 2.2 (a) are fabricated from three different molds. The sensor elements are made of rubber with conductive ink painted on their surfaces. The conductive ink is made by mixing carbon powder and alcohol with a 1–4 ratio in weight. The size of the elements is 6 mm × 6 mm and 3 mm in height.

The sensing elements are laid out in the space inside the base (part 2 in Figure 2.2 (a)). The cover (part 1 in igure 2.2 (a)) is fixed on top of the base with the silicone adhesive, Smooth-on Sil-poxy®. Some space remains inside the top layer, so the element detects the contact force directly and locates the contact point accurately. It is worth noting that there are coupling effects between different sensing elements [31]. The gap spacing between sensing elements is critical to localizing the contact points. If force is applied and the gaps are filled inside the sensor, the stress would flow from the contact location to other sensing elements. Therefore, all elements would respond, and the coupling effect influences the accuracy of contact point detection. For simplicity, the the gap spacing is designed to prevents the transmission of of stress caused by external forces, ensuring each element operates independently without influence from others.

Figure 2.2 (a) also demonstrates the structure of the bottom layer. On top of the bottom rubber (part 3 in Figure 2.2 (a)) a piece of Velostat (part 5 in Figure 2.2 (a)) sandwiched between two pieces of conductive fabric (part 4 in Figure 2.2 (a)). Then, the bottom is bonded with the top layer by the silicone adhesive. The soft tactile sensor is finished, as shown in Figure 2.2 (b). The dimensions of the sensor are 40 mm in length, 38 mm in width, and 8 mm in height.

Design of Sensing Circuits

The sensing circuits attempt to amplify and convert the sensing signal. For the feature-detection layer, noninverting amplifiers are applied to convert the resistance change into an electrical signal for each element. Therefore, the sensor array employs eight noninverting amplifiers, each dedicated to one of the elements. In the force-measurement layer, the resistance variation is converted into a voltage signal using a Wheatstone bridge configuration. An amplifier, INA126, is used to enlarge the sensing voltage from the Wheatstone bridge.

2.3   Modeling of Soft Sensor

Mapping the sensing voltages to contact information precisely is vitally essential in the sensor design. Previously, an algorithm is created to identify contact features and positions. However, misclassification happens when the point contact occurs between two sensing elements. The algorithm would misclassify contact features. To reduce the misclassification rate, the algorithm could become overly complex and inefficient. To solve this issue, machine learning methodologies serve as a convenient solution for the feature-detection layer. In addition, the force-measurement layer would exhibit nonlinearity due to the characteristics of the sensor materials. Traditional regression methods with feature engineering techniques are adopted at first, and it is hard to achieve certain accuracy. Therefore, a machine learning algorithm is applied to address the issue in the bottom layer. Further detailed information will be discussed below.

Modeling of Feature-Detection Layer

As mentioned in Section 2.2, the feature-detection layer is designed specifically to identify contact points and features. Several objects, such as fruits and vegetables, which have various contact features, are used to contact this layer and collect the responses of the elements. Since there are eight elements, their responses form a vector V, which serves as an input for the classifier

$$V = [v_1, \ v_2, \cdots, \ v_8]^T \in \mathbb{R}^8 \tag{2.3}$$

where v_i is the response of $i-th$ element, and the subscript i represents the element number, and the responses are all normalized to 0–1. Since the resistance of every element might vary, normalized responses are easier to ensure the consistency of their sensitivity.

The contact features also form a vector C_f, which is labeled manually and acts as the output for the classifier. The categorical variables are coded by the one-hot encoding method [89] as in (2.4) and Figure 2.6.

$$C_f = [c_1, \ c_2, \ c_3]^T \tag{2.4}$$

where c_1, c_2, and c_3 correspond to the categorical variable of point, line, and surface contact, respectively. That is, the point, line, and surface contact is labeled as $[1\ 0\ 0]^T$, $[0\ 1\ 0]^T$, and $[0\ 0\ 1]^T$, separately.
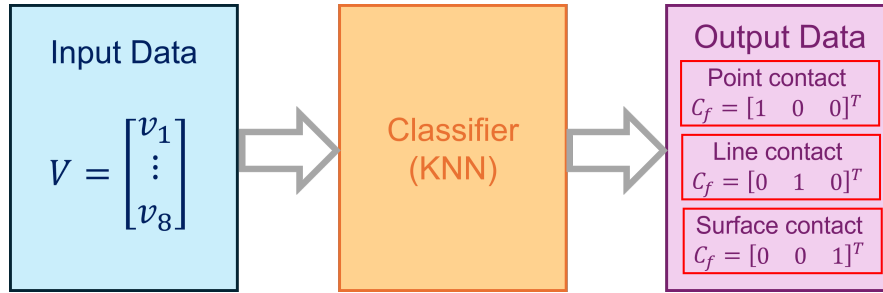
Figure 2.6: The classifier is trained by the input V and the corresponding output C_f with one-hot encoding labeled manually (i.e., the point contact is labeled as $[1\ 0\ 0]^T$, and the line and surface contact are encoded as $[0\ 1\ 0]^T$ and $[0\ 0\ 1]^T$).

After testing four different classification algorithms (support vector machine, k-nearest neighbors, Naive Bayes classifier, and logistic regression), it was found that k-nearest neighbors outperformed the other three algorithms in feature detection. Therefore, the k-nearest neighbors algorithm was selected as the classifier for contact features in the sensor.

To select a good parameter for the k-nearest neighbor's classifier, the performance of the classification accuracy in the range from k = 1 to k = 10 is evaluated. A total of 630 sensor responses are collected and they are labeled as a dataset. The dataset is split into training and testing sets with 80 % and 20 % ratios. The cross-validation method is applied to evaluate the performance of models. By using cross-validation, the overfitting and selection bias problems are avoided [36]. The evaluation result is shown in Figure 2.7. When k = 3, the average training and testing accuracy of the k-nearest neighbor's classifier is the best compared to other k values and is 96.43 % and 96.83 %, respectively. By contrast, the accuracy of other classifiers is all under 90 % in both training and testing data sets.

In real-world applications, a single classifier may exhibit a certain level of misclassification. To enhance prediction accuracy, the bagging classifier method is employed, as discussed in [10]. The bagging k-nearest neighbors classifier is configured with 25 estimators. Additionally, 85 % of the data is randomly sampled from the training set, and seven features from the input data in (2.3) are selected arbitrarily to train each base classifier. The prediction results of the bagging classifier are the average of all the base classifiers. The training (cross-validation) and testing accuracy are 94.84 and 95.24%, respectively. Although the training and testing accuracy of the bagging classifier is not as good as a single classifier, it does improve the accuracy in the experiments as discussed in Section 2.2.
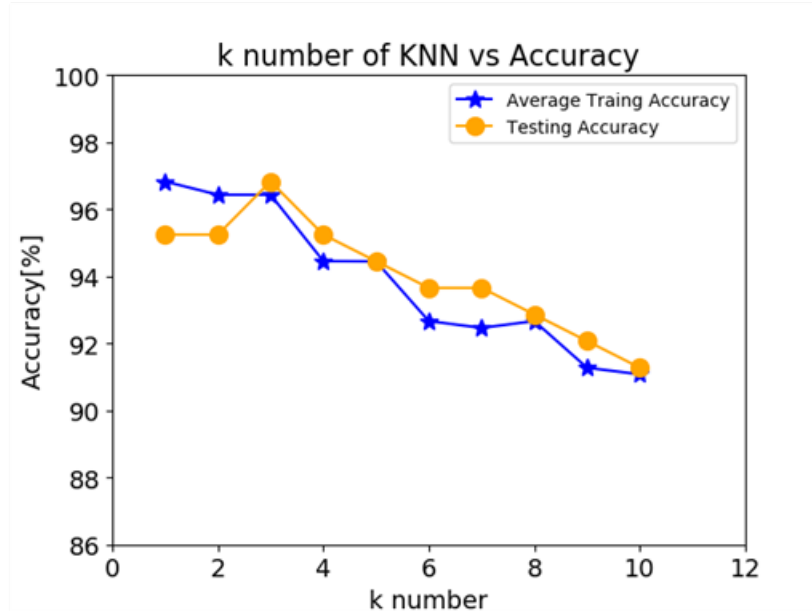
Figure 2.7: The average cross-validation training and testing accuracy versus various k numbers of the k-nearest neighbor's classifier.

Modeling of Force-Measurement Layer

To model the force-measurement layer, collecting data accurately is an important issue. A small deviation of collected data could lead to modeling bias in this design. Therefore, a set of calibration weights serves as the contact force since the set comes in a wide variety of weights and is more accurate. In this work, twenty-two various weights are used including 1, 2, 2.5, 3, 4, 5, 7, 8, 10, 12, 14, 15, 20, 25, 30, 35, 40, 45, 50, 60, 65, and 70 gw. The weights in the set are 1, 2, 5, 10, 20, 50, and 70 gw. The other weights are obtained by using two or three different weights together. They are all measured three times. The corresponding signal of 0 gw is also considered. Thus, 69 data points are collected.

The relation between the sensing signal and contact force (weights) is highly nonlinear as shown in Figure 2.8 (a). To convert the sensing signal to contact force, Nadaraya–Watson regression (NWR) [76, 113] is applied to find the model of the force-measurement layer. Consider that the sensor is modeled as

$$f_i = g(\bar{v}_i) + \epsilon_i \tag{2.5}$$

where f_i is the prediction of contact force, $\bar{v}_i$ is the sensing voltage of the bottom layer, and ϵ_i is the noise. The NWR is to find a nonlinear relationship between the observed pair of data.

The NWR estimator for $\hat{g}(\bar{v}_i) = E[f|v = \bar{v}]$ is
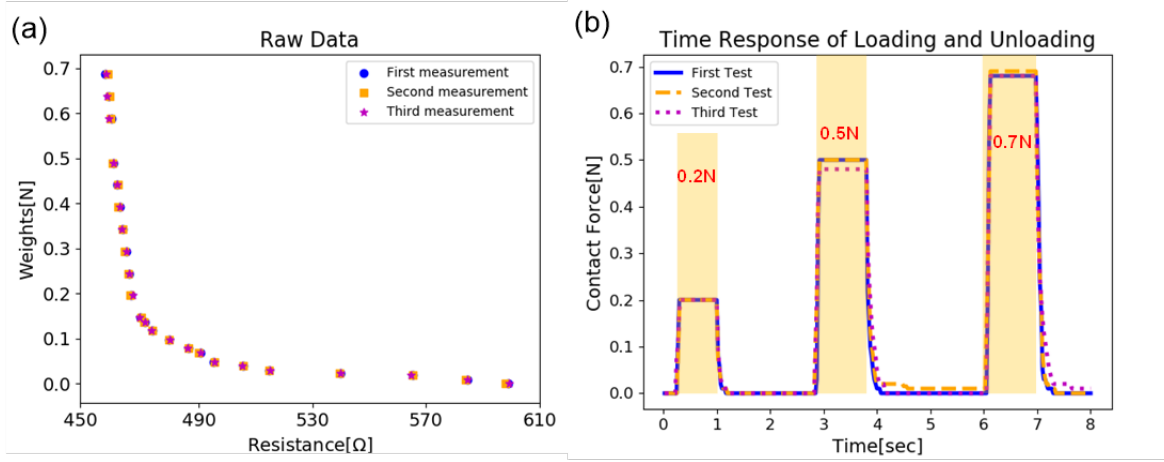
Figure 2.8: (a) Demonstrates responses of the force-measurement layer correspond to some selected weights. The loading and unloading time responses are conducted with forces of 0.2 N, 0.5 N, and 0.7 N, each repeated three times as depicted in (b). The three measuring cycles are performed and the data is synchronized to check the repeatability of time responses.

$$\hat{g}(\bar{v}_i) = \frac{\sum_{n=1}^{n} K(V_i, \bar{v}_i) \times f_i}{\sum_{n=1}^{n} K(V_i, \bar{v}_i)} \tag{2.6}$$

$$K(V_i, \bar{v}_i) = exp\left(-\frac{\parallel V_i - \bar{v}_i \parallel^2}{2\sigma^2}\right) \tag{2.7}$$

where $\hat{g}(\bar{v}_i)$ is the prediction force of NWR, $K(\cdot)$ is the Gaussian kernel function, σ is the covariance, and V_i is the $i-th$ observed data where $i = 1 \cdots m$. Note that there are m collected data.

The dataset is divided into training and testing sets using an 80 % to 20

Calibration of Sensor Drift Effect

In this design, the sensor drift effect degrades the accuracy of the force-measurement layer. The sensing signal is observed to drift linearly. The linear regression is used to remedy the drifting issue [80]. To be more specific, the 5, 20, 50, and 70 gw calibration weights are utilized to get the sensing signal at the beginning of every experiment. Therefore, the sensor's drift effect can be quantified and modeled using the linear regression method with the measured signal. Subsequently, the drift problem is compensated by the linear model.
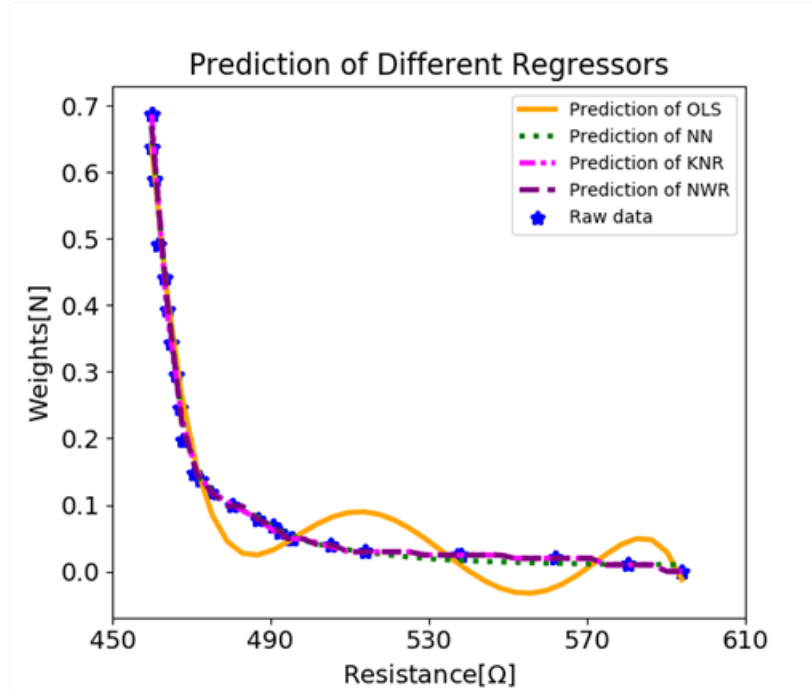
Figure 2.9: (a) The fitting results of four different regression methods including ordinary least square, neural network, k-nearest neighbors regression, and NWR.

2.4   Experimental Evaluation

Experimental Setup

The experimental setup is demonstrated in Figure 2.10. The sensing information from the circuits is processed using the Arduino MEGA 2560 (SparkFun Electronics, Niwot, CO). Arduino MEGA 2560 is a microcontroller based on the Microchip ATmega 2560. The Arduino board is equipped with 54 digital I/O pins and 16 analog I/O pins. The on-chip analog-to-digital converter is applied to sample information from those pins, and its resolution and sampling frequency are 10 bits and 9.6 kHz, respectively. Among the analog I/O pins, one pin read data from the force-measurement layer, and eight pins read the responses from the eight elements in the feature-detection layer. In addition, a custom-made two-fingered gripper is constructed to test this soft tactile sensor. The gripper is driven by a proportional derivative (PD) controller implemented in the Arduino board. The loop time is set as 25 ms to reduce force errors [125].

The Arduino board is connected to both the soft sensor and the gripper. The microcontroller is also synchronized with a computer to log sensing data. The logged data are further processed in Python to get contact force, contact features, and contact location.
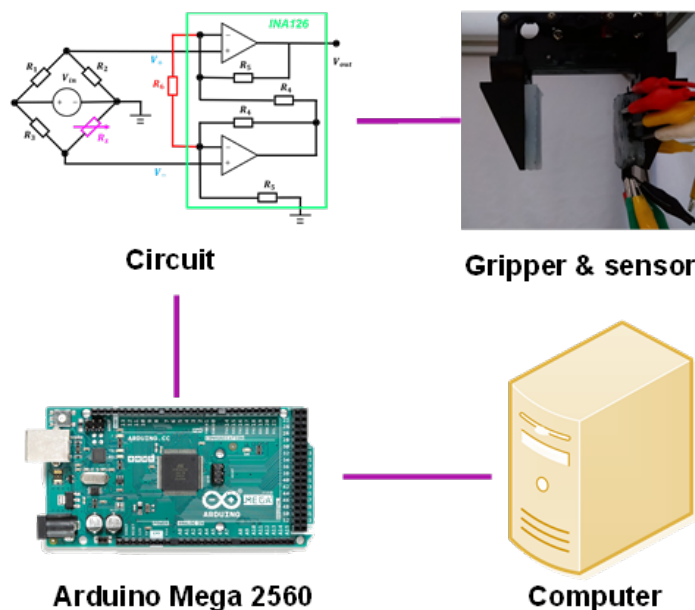
Figure 2.10: Experimental setup.

Sensor Tested Alone

To test the accuracy and repeatability of the soft sensor, a few objects whose weights are distributed in the sensing range of the sensor are chosen. The test result of the force-measurement layer is demonstrated in Table 2.2. Eggs, small carrots, tofu, sliced sausage, and a coin are used to test the sensor. Each object is repeatedly measured ten times to test its accuracy and repeatability. The measured forces are the objects' weights. The true weights are measured using a weight scale. The best case in these experiments achieved 98.9%, and the average accuracy was 95.4%. Note that the low stiffness of the object material would degrade the accuracy. If the object is quite soft such as tofu, the weight of the object cannot be directed into the sensor efficiently but leads to deformation on its own, which causes measurement errors. Moreover, the loading and unloading conditions are also conducted to observe the hysteresis effect as in Figure 2.8 (b). The responses of different measuring cycles are done, and the data is synchronized to examine the repeatability. The hysteresis effect does not influence the measurements considerably based on the results.

The testing results of the feature-detection layer are shown in Figure 2.11. More target objects are considered such as cherry tomato, egg, small carrot, sliced cucumber, sliced banana, hot dog, sponge, and tofu. The egg and cherry tomato correspond to point contact. The sponge and tofu are seen as surface contact. The other is treated as line contact. They are all measured 10 times, so the overall data is 80. The confusion matrix of the classifier, the k-nearest neighbors algorithm, can be observed in Figure 2.11 (a). The misclassifica-

Table 2.2: The accuracy and repeatability test of the force-measurement layer.

	Coin	Sliced carrot	Tofu	Sliced sausage	Egg
Measured weight (gw)	4.80±0.40	13.85±0.37	16.53±2.27	30.47±1.47	61.76±4.41
True weight (gw)	5	14	18	29	59
Accuracy (%)	96.0	98.9	91.8	94.9	95.3

tions occur in identifying point and line contacts, which causes the overall accuracy to drop to 92.5%. By using the bagging classifier, the accuracy of the experiment is improved to 96.25%. The confusion matrix of the bagging classifier is given in Figure 2.11 (b), where the classification rate of each feature increases.
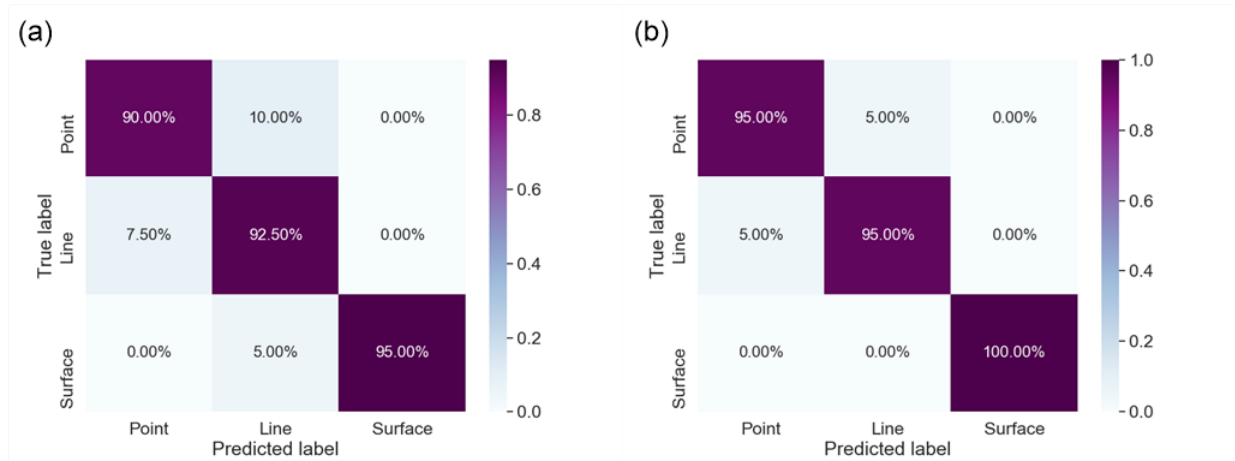
Figure 2.11: Confusion matrix of the k-nearest neighbor's classifier is represented in (a) and that of the bagging classifier based on the k-nearest neighbors is displayed in (b)

It is discovered that a few errors result from misclassifying point contact as line contact or misidentifying line contact as point contact. The main reason is that the point contact might happen between two elements, so multiple elements respond and are sometimes misidentified as line contact. On the other hand, line contact happens when two to three elements respond. Sometimes one of the elements responds faster or more responsive than the other since the surface of the object barely generates the perfect line contact. Moreover, the element is made of rubber and might exhibit nonlinearity which leads to misclassification. However, the error rate is reduced by the bagging classifier algorithm in this design.

Sensor Tested on a Robotic Gripper

To validate the sensing ability during grasping, the soft tactile sensor is mounted on a robotic gripper to perform a set of grasping experiments. The setup is demonstrated in the top-

right figure in Figure 2.10, where the soft sensor is attached to one finger of the two-fingered gripper, and the cured silicone rubber without sensing units is attached to the other finger. The block diagram of feedback control can be discovered in Figure 2.12. The target objects are the egg, the sliced carrot, and the tofu since they are more delicate and irregular-shaped compared to other objects in Section 2.4. The gripper with traditional tactile sensors can only sense limited tactile data since they cannot fit their profiles and have fine contact. Using a soft tactile sensor resolves the issue and allows for obtaining more contact information, as discussed below.

To grasp those objects stably, the gripper needs to provide enough normal force to resist gravity. The desired contact force of each target object was computed offline by

$$F_c = F_l/2\mu \tag{2.8}$$

$$F_{est} = 2\mu F_m \tag{2.9}$$

where F_l is the lift force determined by the user and should be greater than the object's weight. F_c is the desired contact force and μ is the coefficient of friction of rubber [75]. F_{est} is the estimated lift force. The friction force is generated by both fingers, so F_l is divided by 2μ, and F_m is multiplied by 2μ to obtain F_c and F_{est}. The F_c serves as a reference for the PD controller of the gripper as in Figure 2.12.
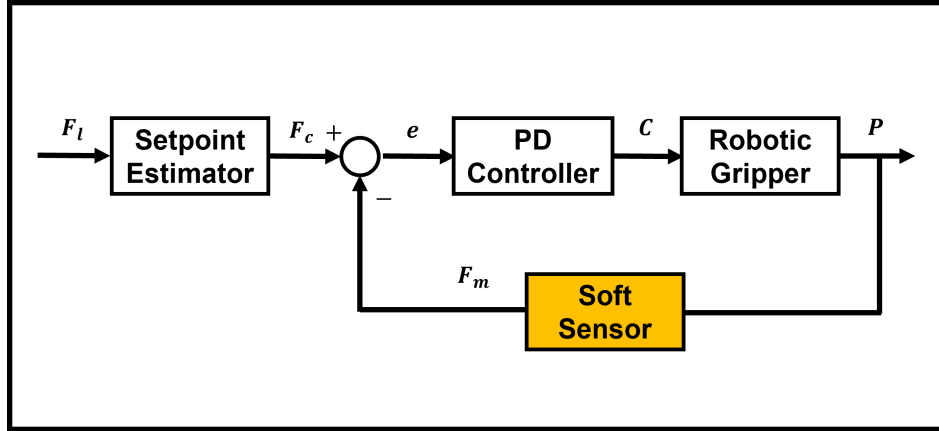
Figure 2.12: Scheme of the feedback control of the robotic gripper with the soft sensor. The F_l is determined based on the weight of the target object. With F_l, the F_c could be computed by Coulomb's law. The F_c will be compared with the measured force F_m from the soft sensor to get e. The PD controller will process e to generate the command C for the robotic gripper. Then, the measured force Fm changes with the position of the gripper P.

During the grasping process, the force-measurement layer monitors the normal force. The measured force F_m is compared with the reference, and the error e is fed into the PD controller to generate a command C, which drives the servomotor to adjust the position

of the gripper P. Simultaneously, the feature-detection layer identifies the contact feature, while the contact position is estimated based on the responses of the sensor elements.
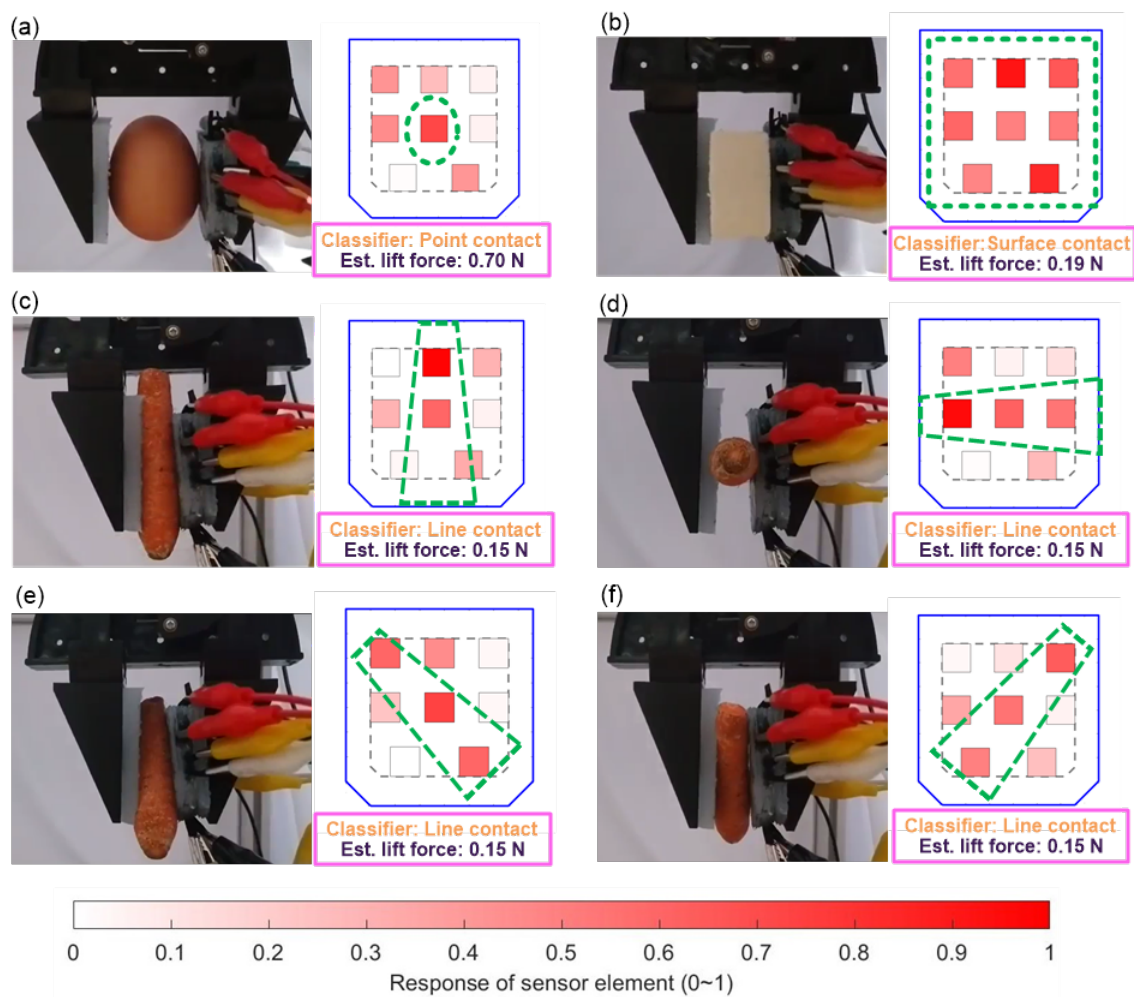
Figure 2.13: Testing results of the soft tactile sensor on a robotic gripper grasping the egg, the tofu, and the small carrot are displayed in (a)–(f). The responses of the feature-detection layer can be observed on the left side of each subplot, with the green dashed lines representing the contact profiles of the objects. Also, the corresponding contact feature and estimated lift force for each object are shown in the right-bottom box.

The responses of sensor elements are shown in Figure 2.13. If the sensor detects nothing, the color is white. If it detects contact, its color begins to turn red. The darker the element, the more responsive the element is as displayed in the color bar. The objects' contact profiles are indicated by the green dashed lines in Figure 2.13. The egg is classified as the point contact. The tofu is identified as the surface contact. The carrot is detected as the

line contact. Simultaneously, the pose of the carrot would be perceived by the responses of the sensor array as exhibited in Figure 2.13 (c)–(f). With the contact feature provided, the robotic gripper can identify the rough geometric features of objects, which is particularly useful in scenarios where no vision system is available, or the vision system is occluded.

The force profiles of grasping the egg, tofu, and carrot are shown in Figure 2.14 (a)–(c). The desired gripping forces are 0.3, 0.09, and 0.08 N, respectively. The controller tracks the setpoint with limited errors and generates enough lift force. The estimated lift forces, F_{est}; are 0.7, 0.19, and 0.15 N for the egg, the tofu, and the carrot as in the right-bottom block in every subplot of Figure 2.13. The lift force is controlled to be greater than their weights which are 0.6, 0.165, and 0.135 N. Furthermore, due to the softness of the grasped object and the latency of the sensor, the force profile may exhibit some noise, which can be mitigated by adjusting the gain of the controller.
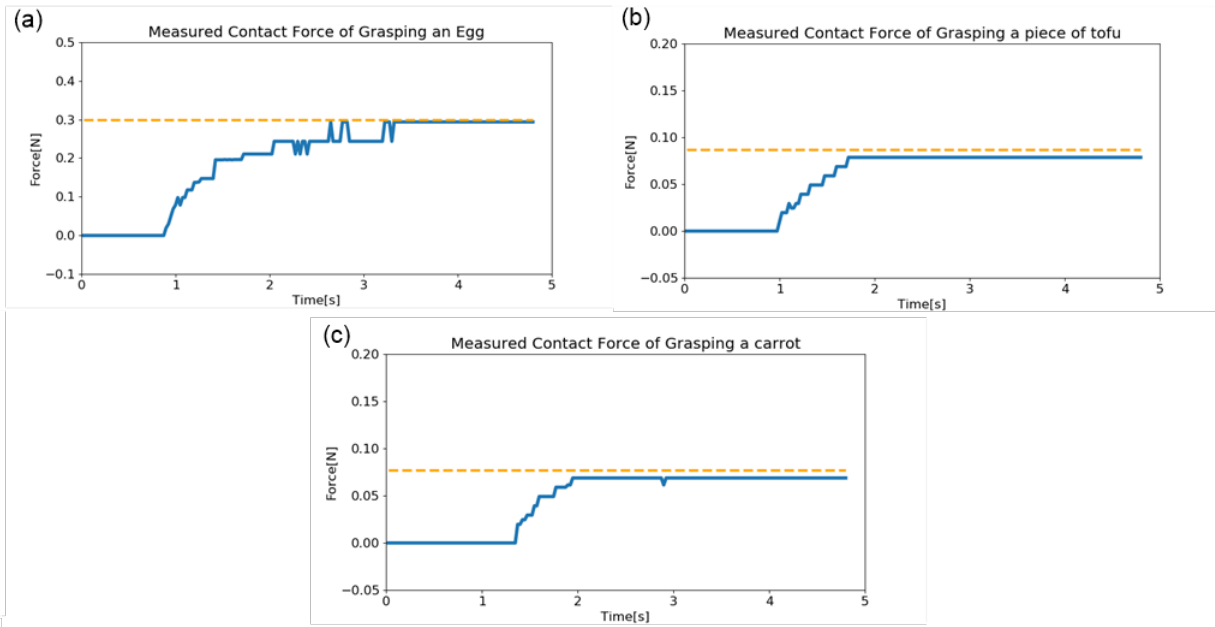
Figure 2.14: Force trajectories of the gripper grasping the egg, the tofu, and the small carrot. In each subplot, the orange line represents the reference for each object, while the blue line denotes the force trajectories measured by the force-measurement layer of the soft sensor.

2.5   Summary

This chapter introduces a new multifunctional soft sensor designed to mimic human skin. The sensor contains two layers of sensing units, the feature-detection layer, and the force-measurement layer. The feature-detection layer is a sensor array that detects the contact

features such as point, line, and surface contacts, and estimates the contact locations and poses of the grasped object. The bagging predictor using the k-nearest neighbors classifier achieves a categorization accuracy of 96.25 % in this study unit. On the other hand, the force-measurement layer can measure the contact force. The Nadaraya–Watson regression is adopted to map the sensing voltage to contact force. The average measurement accuracy is 95.4% in this unit. The measured force serves as a feedback signal for the PD controller of the gripper to control its position and grasp fragile objects such as eggs, carrots, and tofu stably. The top layer is capable of identifying objects' features and even their poses. The experimental results verify the performance of the proposed design. The soft sensor demonstrated its strengths in sensing tactile information of objects such as fruits and vegetables.

Chapter 3

Model-Based Optimized Design of a Soft Pneumatic Actuator

3.1 Introduction

Soft robots have gained attention in recent years. Their degree of freedom, adaptability, and compliance are superior to the traditional robots. Soft robots show potential to explore unknown environments such as underwater or outer space explorations [51, 100, 105, 129], deliver delicate components in medical industry [1], and manipulate fragile objects in the food industry [22, 141, 112]. The motion of soft robots relies on soft actuators, and soft pneumatic actuators (SPAs) are the most popular options [133, 28, 66]. They are easier to fabricate, cost-effective, and have high power density [128]. However, despite these advantages, the use of soft robots also presents challenges. Their elasticity reduces their generated force/torque and makes them hard to control. The task of optimizing force/torque, bending angle, and controllability of SPAs, which involves formulating an optimal design problem and defining suitable objective functions and constraints, poses a challenge to researchers [110].

In tackling these challenges, an intuitive design approach that draws inspiration from nature can be particularly effective [58, 91, 42]. Soft actuators are often inspired by natural forms, such as the human hand [142], octopus arm [70, 122], or elephant trunk [43]. This natural inspiration, combined with the use of finite element analysis (FEA) and optimization methods or machine learning algorithms, has been successful in exploring the dimensional parameters of soft pneumatic actuators [30, 48, 110, 134, 45]. However, these approaches have often focused on enhancing single performance metrics such as force/torque or bending angle. The optimal design of SPAs considering multiple performance indexes is a topic that is still seldom discussed. Additionally, these methods often rely on trial-and-error and time-consuming simulations or experiments [30]. This research, therefore, aims to optimize force/torque and bendability and improve controllability with a model-based optimization formulation, while staying true to the inspiration we draw from nature.

Moreover, determining the dynamical properties of SPAs, such as natural frequency, is

another challenge during the design stage. As the optimal parameters are determined by optimization formulation, the dimensional parameters directly influence the natural frequency, which in turn impacts its controllability [13, 128]. Determining the dynamic properties, such as natural frequency, during the design phase is useful for enhancing the controllability of SPAs, influencing the system's pole locations, response time, and control efforts to achieve the desired response. However, modeling those properties of SPAs is difficult due to their inherent compliance and nonlinearity [40, 5]. Recent studies [120, 95, 109] have addressed this challenge by simplifying SPA modeling, treating them as second-order systems where the natural frequency becomes a key parameter for improving controllability.

Extending these insights, this chapter introduces an optimal design approach for soft actuators considering multiple performance indexes. To simplify the complex geometry of the soft actuator, it is approximated by a cantilever beam, as illustrated in Figure 3.1. The optimization problem formulation links input air pressure to force/torque as well as bending angle while also exploring the relationship between natural frequency and dimensional parameters. The preliminary tests and experiments have validated the optimal design, showcasing enhanced output torque and bending angle compared to the previous work [128], while also modifying the dynamical properties. To the best of the author's knowledge, there is limited research that examines explicitly and considers the dynamical properties of soft actuators during the design phase. The main contributions of this research are significant and include:

- Deriving nonlinear kinematic and dynamic models based on approximated structure to facilitate a model-based optimal design formulation.

- Optimized design of a SPA, improving force/torque, bending angle, and system controllability concurrently, setting a new benchmark in multifaceted performance enhancement during the design phase.

- Validating the design and fabrication of SPA for controllability by linear quadratic optimal theory with achieved high-speed responses.

The proposed approach is compared with several design methods to position the contributions within the existing literature. The previous work [128] presented an optimal model-based design method to enhance the output force/torque of the soft actuator. However, the optimization formulation has been modified, which enhances force/torque, bending angle, and the system's controllability simultaneously. This paper improves the bendability and natural frequency of the SPA. Lotfiani et al. [67] proposed a similar model-based optimal design method for a soft pneumatic actuator. However, the model was based on the hyperelastic model. In contrast, this approach uses nonlinear approximated models that are more implementable. Liu et al. [65] introduced an energy-based method for searching optimal dimensional parameters, resulting in superior output torque compared to commercial soft actuators. Nonetheless, this method improves force/torque, bending angle, and the
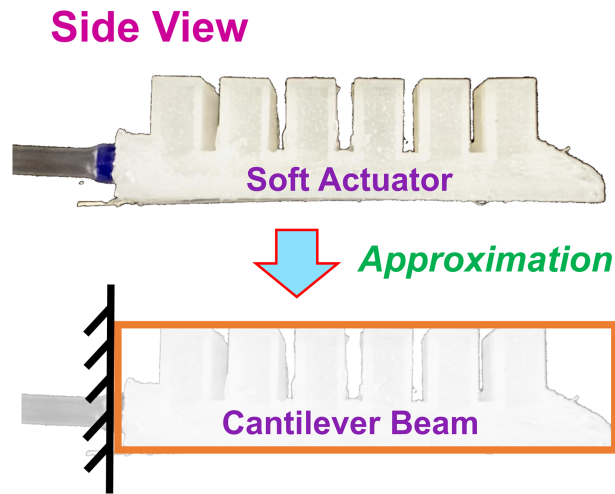
Figure 3.1: The soft pneumatic is analyzed mechanically by approximating its intricate structure as a cantilever beam.

system's controllability during the design phase. Demir et al. [22] employed a machine learning algorithm to model pneumatic actuator performance using FEA simulation data. Their model was utilized to search for optimal design parameters under various constraints. This work uses the mathematical models between input pressure and force/torque, bending angle, and natural frequency to identify the optimal parameters. Polygerinos et al. [87] attempted to correlate pressure changes and output torque in a soft pneumatic glove; however, their analysis relies on a mechanical model that requires the determination of multiple material properties through uniaxial tensile tests. In contrast, the proposed method approximates the structure to a simplified beam, reducing the number of parameters that need to be characterized. By simplifying the model, it is a trade-off between complexity and accessibility. In summary, this research aims to provide valuable insights to designers of a soft actuator design method that minimizes the need for trial-and-error methods. Meanwhile, the design approach enhances force/torque and bending angle and determines the system's dynamical properties, improving controllability.

The remainder of this chapter is organized as follows. Section 3.2 describes the kinematic and dynamic modeling of the SPA. Section 3.3 discusses the SPA's optimization formulation and optimal design. Section 3.4 uses experimentation to verify the optimal design approach, and Section 3.5 concludes the work.

3.2 System Modeling

In this section, nonlinear kinematic and dynamic models are constructed using an approximated structure, as shown in Figure 3.1. Using an approximated structure holds the merit of formulating a feasible and solvable optimization problem [9]. Although hyperelastic models are more accurate [67] than approximated models, the complexities of the models may present challenges in solving the optimization problem. Thus, nonlinear models with approximated structures are utilized. The comparisons between predicted and experimental results can be observed in Section 3.4.

Kinematic Modeling

The soft pneumatic actuator features a corrugated geometric shape characterized by a pattern of parallel ridges and grooves and contains multiple discrete chambers. To analyze the structure mechanically, the corrugated structure can be approximated by the cantilever beam in Figure 3.1. The following assumption grounds the approximation as in Section 3.3. Although some literature suggested linear model assumption [119, 1], this work considers a nonlinear model with an approximated structure.

Assumption 1. *[128] The generated force/torque of the soft actuator is analyzed when the pressure distributes uniformly (steady state) across every individual chamber interior.*

The approximated structure is analyzed by the theories of mechanics [13]. The obtained simplified models will serve as the objective function for the optimization problem in Section 3.3.

Pressure-to-Force/Torque Model

The mechanical analysis process is demonstrated in Figure 3.2 (a)–(d). A part of the cantilever beam (a chamber interior) is segmented for mechanical analysis [13]. The chamber is open on both sides because of the air channel. Although the chamber is open on both sides, it is treated as closed because of *Assumption 1* and pressure balances in the open areas. Pressure applied to the chamber leads to structural expansion and generation of force/torque and bending angle. Given the cantilever beam's continuity, the segmented parts' mechanical behaviors are presumed to be continuous along the structure. Then, equation (3.1) is used to analyze the force equilibrium along x direction in Figure 3.2, and (3.2) calculates the torque generated by the pressure supplied by the syringe pump [126]:

$$\sum F_x = \int_A p(y)dA \tag{3.1}$$

$$T = \sum T_z = \int_A y \times p(y)dA \tag{3.2}$$
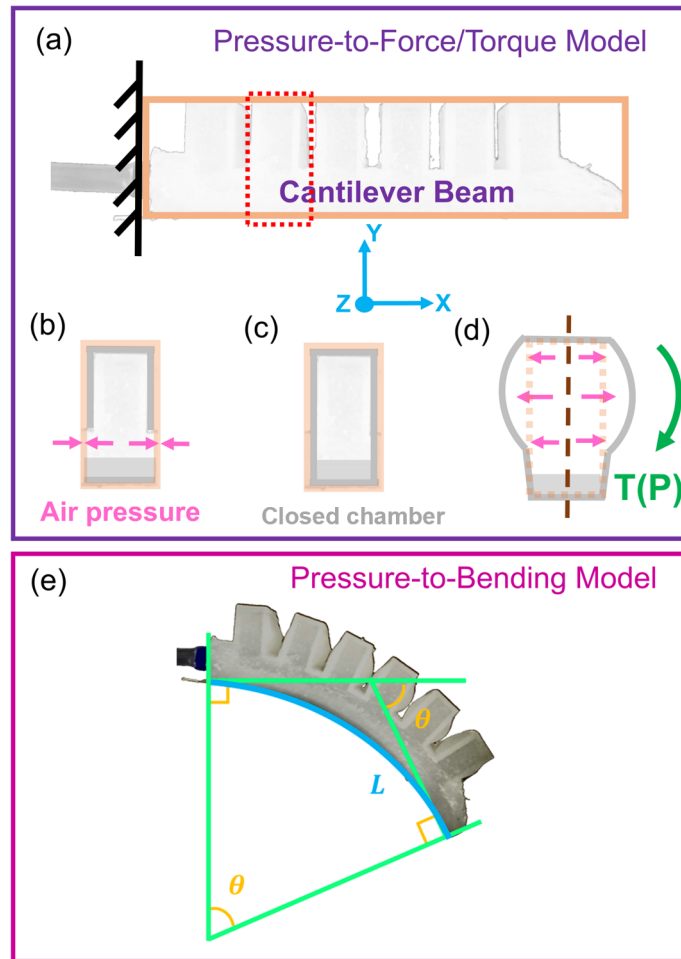
Figure 3.2: The mechanical analysis of the Pressure-to-Force/Torque model involves the
following steps (a)–(d). (a) Segmenting a chamber from the actuator for analysis. (b) Both
ends of the segmented chamber are open. (c) Treating the open chamber as a closed volume,
as the air pressure within the chamber is evenly distributed and balanced across the open
areas. (d) The supplied air pressure inflates the chamber and generates torques. The bending
geometric of the soft actuator for analyzing the Pressure-to-Bending model is shown in (e).

where F_x is the force inside the cantilever beam in the x direction, $p(y)$ is the pressure inside
the beam and is a function of y, T is the torque generated by the actuator, T_z is the torque
generated by pressure distribution function $p(y)$, and dA is the small area where the pressure
$p(y)$ is applied. Note that $p(y)$ becomes a constant under *Assumptions 1*.

The analysis of the force/torque generated by input pressure P is presented in the pre-
vious work [128]. The correlation between the input pressure P and the pressure generated
in the actuator's wall P_w is given:

$$P_w = \frac{(a - t)(w - 2t)}{bw + wt + 2at - 2t^2} P \tag{3.3}$$

where a is the distance between the neutral surface and the top of the actuator, b is the
distance between the neutral surface and the bottom of the actuator, w is the width of the
actuator, and t is the wall thickness as shown in Figure 3.3 (d). Equation (3.2) and (3.3)
then produce a relationship between P and generated torque $T(P)$. Therefore, the $T(P)$ can
be computed as

$$T(P) = T_P + T_{P_w} \tag{3.4}$$

where T_P is the torque contributed by P, and T_{P_w} is the torque created by P_w as shown in
Figure 3.3 (b). Since P_w can be replaced by (3.3), T_P and T_{P_w} are described by using (3.2):

$$T_P = \int_{A_c} y \times P dA_c \tag{3.5}$$

$$T_{P_w} = \int_{A_w} y \times \frac{(a - t)(w - 2t)}{bw + wt + 2at - 2t^2} P dA_w \tag{3.6}$$

where dA_c is the arbitrary small area in the cross-section of a chamber (yellow area) in
Figure 3.3 (c), dA_w is the small area in the cross-section of the wall of the actuator (light
orange and pink areas) in Figure 3.3 (c) and y is the location where the pressure acts as
Figure 3.3 (b). The material above the neutral surface is assumed to be in tension, producing
positive internal pressures.

Pressure-to-Bending Model

Regarding the design of soft actuators, bending angle, and force/torque are usually discussed
in tandem. The bending angle is another index to evaluate the performance of soft actuators.
Thus, enhancing the bending angle is another design objective.

The Pressure-to-Bending model will be built by referencing Euler's bending theory [13,
1]. The work inspires the Pressure-to-Bending model, but there are some differences, such as
the geometric shapes of SPA. Also, the torque in this model is computed by the Pressure-to-
Force/Torque model, while the torque in the work [1] is calculated by a geometric method.
Last but not least, the nonlinear bending model for large deflection components is consid-
ered [62], where the corresponding bending theory is given by
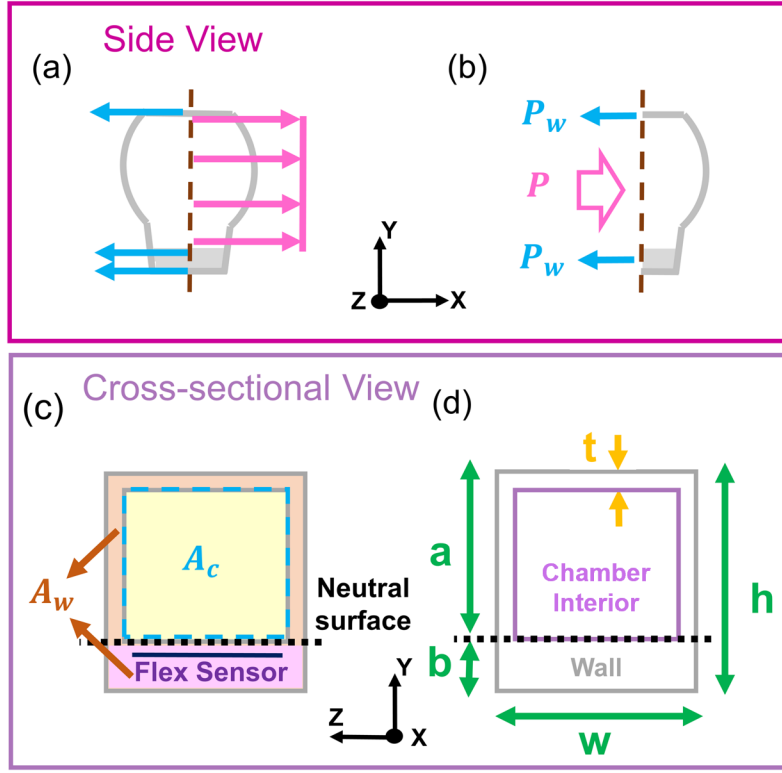
Figure 3.3: (a) The segmented chamber is halved to obtain the free-body diagram. (b) The
free-body diagram showcases the pressures, P and P_w, acting on it. (c) The cross-sectional
view of the chamber is presented, where the neutral surface is depicted by a dashed black
line, and a purple line indicates the embedded flex sensor. (d) The dimensional parameters
of the cross-section are established.

$$\theta(P) = (\frac{n}{n+1})(\frac{T(P)}{EI_n})^{\frac{1}{n}}L \tag{3.7}$$

$$I_n = (\frac{1}{2})^{(1+n)}(\frac{1}{2+n})w(a+b)^{(2+n)} \tag{3.8}$$

where $n \geq 1$ varies with soft materials and obtained through fitting the true $\sigma - \epsilon$ data
provided by [68], θ is the bending angle and is a function of P, E is Young's modulus, I_n
is the moment of inertia for large deflection component, and $T(P)$ is obtained by (3.4). If
considering the deformed length of the structure, the (3.8) becomes

$$\theta(P) = (\frac{n}{n+1})(\frac{T(P)}{EI_n})^{\frac{1}{n}}(L_i + \delta L) \tag{3.9}$$

where L_i is the initial length, L is the elongated length, and $\delta L = L - L_i$. Since $\delta L = PA_cL_i/A_wE$ in [13], (3.9) becomes

$$\theta(P) = (\frac{n}{n+1})(\frac{T(P)}{EI_n})^{\frac{1}{n}}L_i(1 + \frac{PA_c}{A_wE}) \tag{3.10}$$

As $T(P)$ includes P, the δL is also a function of P, bending angle is a function of P and P^2. Both Pressure-to-Bending and Pressure-to-Force/Torque models are the objective function in Section 3.3.
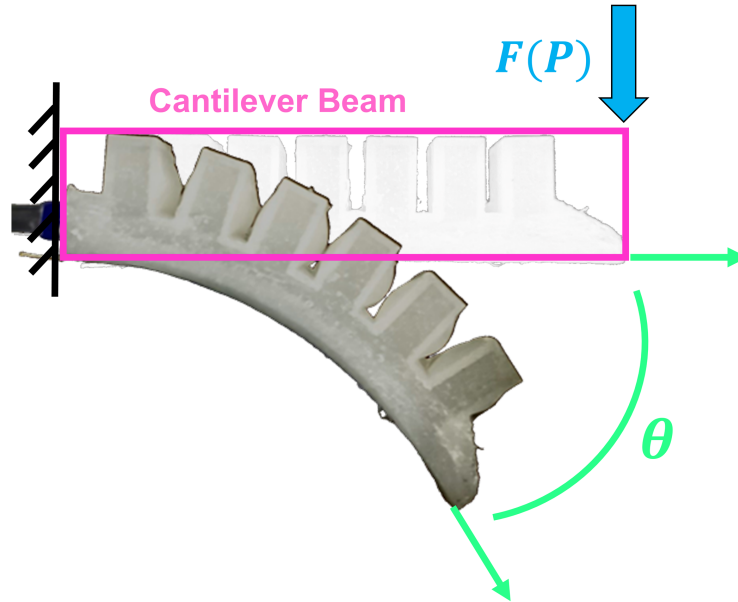
Figure 3.4: The approximated structure of the soft actuator generates a bending angle θ with a load F(P).

Dynamical Modeling

A second-order nonlinear model [62] is employed to represent the dynamics of the bending angle in the soft actuator. This model is chosen for its mathematical simplicity and its capability to capture key dynamic properties: inertia, damping, and stiffness. Note that neglected dynamics in the modeling are considered uncertainties, which can be compensated

for in the control design phase [120, 95, 109, 96]. The second-order dynamical model with
nonlinear spring can be represented in the form as:

$$\ddot{\theta} + \frac{C}{M_{eq}}\dot{\theta} + \frac{K}{M_{eq}}\theta^n = \frac{F}{M_{eq}} \tag{3.11}$$

Here, M_{eq} is the equivalent mass of the soft actuator, C represents the damping constant of
the system, K and F denote the spring constant of the system, and the force applied to the
beam due to the input pressure, respectively. The values $\frac{C}{M_{eq}}$ and $\frac{K}{M_{eq}}$ can also be expressed
as $2\zeta\omega_n$ and $\omega_n{}^2$, respectively, where ζ represents the damping ratio and ω_n denotes the
natural frequency. Hence, the equation can be rewritten in a compact form as:

$$\ddot{\theta} + 2\zeta\omega_n\dot{\theta} + \omega_n{}^2\theta^n = F/M_{eq} \tag{3.12}$$

The analysis can be visualized in Figure 3.4. When a force resulting from input pressure
is applied at the end of the beam, the beam structure undergoes deflection and exhibits a
bending angle θ. The static equilibrium bending angle can be described by the (3.13) [13,
62]:

$$\theta^n = \left(\frac{n}{n+1}\right)^n \frac{FL_i^{n+1}}{EI_n} \tag{3.13}$$

Here, θ represents the bending angle of the approximated beam under large deflection, and F
is the force applied at the end of the beam due to the input pressure. By manipulating (3.13),
it becomes:

$$\frac{F}{\theta^n} = \left(\frac{n+1}{n}\right)^n \frac{EI_n}{L_i{}^{n+1}} = K \tag{3.14}$$

In (3.14), K represents the equivalent spring constant of the approximated beam structure
under the bending force. Therefore, the spring constant is obtained for (3.11). For simplicity,
the damping term is temporarily neglected. Thus, equation (3.11) can be written as:

$$\ddot{\theta} + \left(\frac{n+1}{n}\right)^n \frac{EI_n}{M_{eq}L_i{}^{n+1}}\theta^n = \frac{F}{M_{eq}} \tag{3.15}$$

The term $\left(\frac{n+1}{n}\right)^n \frac{EI_n}{M_{eq}L_i{}^{n+1}}$ in (3.15) represents the square of the natural frequency, as shown
in (3.12). The natural frequency is given by:

$$\omega_n = \sqrt{\left(\frac{n+1}{n}\right)^n \frac{EI_n}{M_{eq}L_i{}^{n+1}}} \tag{3.16}$$

Remark 1. *The natural frequency of the system has a direct impact on its controllability.
Higher values accelerate response times but might increase energy consumption and other
practical constraints. Conversely, lower natural frequencies could pose control challenges due*

to slower responses. Therefore, selecting a natural frequency requires a careful balance between responsiveness, energy efficiency, and system constraints. Ultimately, while increased natural frequency can enhance controllability, it is vital to consider its implications on system requirements and limitations. It is important to note that considerations such as excitation and the proximity of frequencies necessitate the evaluation of natural modes for each design. In this study, we only focus on the first natural frequency, as the second one appears at a considerable distance (three times farther) where the digital controller does not excite this mode.

To complete the dynamical model (3.12), the damping ratio is estimated by second-order system identification over the step responses of the SPA. The damping ratio is not a constant but is accompanied by a perturbation term, $\zeta + \Delta\zeta = 0.7 \pm 0.1$, due to the nonlinearity and unpredictability of the soft materials. The completed dynamical model is needed and used for controller design in Section 3.4.

3.3 Optimal Design Analysis

Regarding soft actuator design, optimal design for the force/torque does not imply optimal design for the bending angle. Usually, an optimally designed soft actuator for bending may not generate large force/torque, and vice versa. This research tries to balance two performance indexes in the optimization formulation and design an optimal soft actuator.

Optimization Formulation

In this subsection, the objective is to identify the optimal dimensional parameters of SPA. By utilizing the derived models in Section 3.2, the design problem is transformed into an optimization problem based on the models, as presented by [105]. Consider the mathematical models, $T(P)$ (3.4) and $\theta(P)$ (3.10) as the objective function, subject to dimension constraints involving a, b, w, and t. Here, a and b represent the height of the chamber's cross-section, w denotes the width, and t signifies the wall thickness of the soft actuator. Figure 3.3(d) presents a schematic representation of the dimensional parameters within the actuator's cross-section. Additionally, since $T(P)$ and $\theta(P)$ are in different units, both equations should be normalized to put equal weight on both indexes. The $T(P)$ is normalized by 0.4 Nm and becomes $\bar{T}(P)$, while $\theta(P)$ is normalized by 1.4π $rads$ and becomes $\bar{\theta}(P)$. If different normalization factors are selected, different optimal parameters will be obtained. The optimization problem is defined as

$$\max_{a,b,w,t} \bar{T}(P) + \bar{\theta}(P)$$

$$\text{s.t. } \dot{P} = 0$$
$$a_1 \leq a \leq a_2$$
$$b_1 \leq b \leq b_2$$
$$h_1 \leq a + b \leq h_2 \tag{3.17}$$
$$w_1 \leq w \leq w_2$$
$$t_1 \leq t \leq t_2$$

where P is a constant value and the constraint parameters a, b, w and t are determined by referencing human fingers' dimensions [108, 65]. The parameters vary as follows: a ranges from 2 to 5 mm, b from 14 to 24 mm, w from 10 to 30 mm, t from 1.5 to 3.0 mm, and h from 15 to 25 mm. The similar results of (3.17) can be referenced in [128].

Considering System Controllability

Based on (3.16), the natural frequency of the soft pneumatic actuator is influenced by the dimensional parameters (moment of inertia). Equation (3.17) can be revised by adding constraint. Therefore, not only will the optimal dimensional parameters be identified, but the suitable natural frequency will also be determined in the design stage. By squaring (3.16), it is obtained

$$\omega_n{}^2 = (\frac{n+1}{n})^n \frac{EI_n}{ML_i{}^{n+1}} \tag{3.18}$$

and $I_n = (\frac{1}{2})^{(n+1)}(\frac{1}{n+2})w(a+b)^{(n+2)}$. Thus, the (3.18) can be manipulated as

$$Ew(a+b)^{n+2} = (\frac{n}{n+1})^n (2^{n+1})(n+2)M\omega_n{}^2 L_i{}^{n+1} \tag{3.19}$$

Since the L_i is constant, the designer can choose the ideal natural frequency range.

$$\max_{a,b,w,t} \bar{T}(P) + \bar{\theta}(P)$$

$$\text{s.t. } \dot{P} = 0$$

$$a_1 \leq a \leq a_2$$
$$b_1 \leq b \leq b_2$$
$$h_1 \leq a + b \leq h_2 \tag{3.20}$$
$$w_1 \leq w \leq w_2$$
$$t_1 \leq t \leq t_2$$
$$C_1 \leq Ew(a + b)^{n+2} \leq C_2$$

where the additional constraint of (3.20) with respect to (3.17) is

$$C_1 \leq Ew(a + b)^{n+2} \leq C_2 \tag{3.21}$$

Given that E is a constant, determined by the selected material, and w, a, b are bounded
as in (3.22), there are a_3, a_4, b_3, b_4, w_3, and, w_4 which are inside the ranges of (3.22), and it
can be said that the minimum value for $Ew(a + b)^{n+2}$ is $Ew_3(a_3 + b_3)^{n+2}$ and the maximum
value is $Ew_4(a_4 + b_4)^{n+2}$.

$$a_1 \leq a \leq a_2$$
$$b_1 \leq b \leq b_2 \tag{3.22}$$
$$w_1 \leq w \leq w_2$$

To ensure the added constraint does not render the problem infeasible, it is needed to
choose C_1 and C_2 such that:

$$C_1 = (\frac{n}{n+1})^n (2^{n+1})(n+2) M_1 \omega_{n1}{}^2 L_i{}^{n+1}$$
$$\tag{3.23}$$
$$C_2 = (\frac{n}{n+1})^n (2^{n+1})(n+2) M_2 \omega_{n2}{}^2 L_i{}^{n+1}$$

where M_1 and M_2 are the SPA's lower and upper bounds of mass. Since mass is related to
dimensional parameters of a, b, w and t (volume $\times$ density), the selection of the mass should
reference the ranges of dimensional parameters in (3.20) to avoid hitting their upper or lower
bounds.

Noting that $E > 0$ and all of w, a, b, and n are non-negative, the function $Ew(a+b)^{n+2}$ is
increasing with respect to w, a, and b. Therefore, the bounds for C_1 and C_2 are valid. This
ensures that a range of values of a, b, w, and t exists such that the additional constraint and
all the original constraints can be simultaneously satisfied.

The optimization problem (3.20) was solved using the solver *fmincon*, where the objective function and constraints were defined. The solver used interior-point algorithm [12] to search for the optimal solution, employing a searching step size of 4×10^{-12}. The solution, which represented a minimum and satisfies all imposed constraints, was obtained after 42 iterations. Additionally, the sequential quadratic programming algorithm [79] in *fmincon* was also applied, and the same parameters were obtained. Specifically, different initial value sets were tested, and the optimization algorithm obtained nearly the same optimal parameters. The optimal values for the design parameters a, b, w, and t are presented in Table 3.1. Note that the parameters have been rounded to integers for manufacturability.

Table 3.1: Optimal parameters and its variances

	b [mm]	a [mm]	w [mm]	t [mm]
Opt. parameters	4.0	20.0	30.0	1.5
Variance 1	4.0	20.0	29.0	1.5
Variance 2	4.0	20.0	28.0	1.5
Variance 3	3.5	20.5	30.0	1.5
Variance 4	3.0	21.0	30.0	1.5
Variance 5	4.0	20.0	30.0	1.75
Variance 6	4.0	20.0	30.0	2.0

Remark 2. *The mass is not explicitly considered in (3.20), as it is indirectly influenced by dimensional parameters $(a, b, w, \text{ and } t)$. The mass is calculated as the product of the volume and density of the soft material. With the density being a constant determined by the chosen material, the volume of the soft actuator is solely dependent on $a, b, w,$ and t. In addition, the constraints outlined in (3.23) dictate the allowable ranges (M_1 and M_2) of the SPA volume, thereby influencing the mass ranges.*

3.4   Experimental Evaluations

This section presents the analysis of both simulation and experimental results. To expedite the preliminary verification, predictions of kinematic models are implemented, allowing us to avoid the fabrication of all soft actuators listed in Table 3.1. The impact of (3.21) on the optimal parameters and controllability of the system is investigated. The results of essential performance metrics, namely torque and bending angle, are also presented. Lastly, an LQR controller is designed to achieve desired dynamical performance, focusing on reducing response time and minimization of steady-state error.
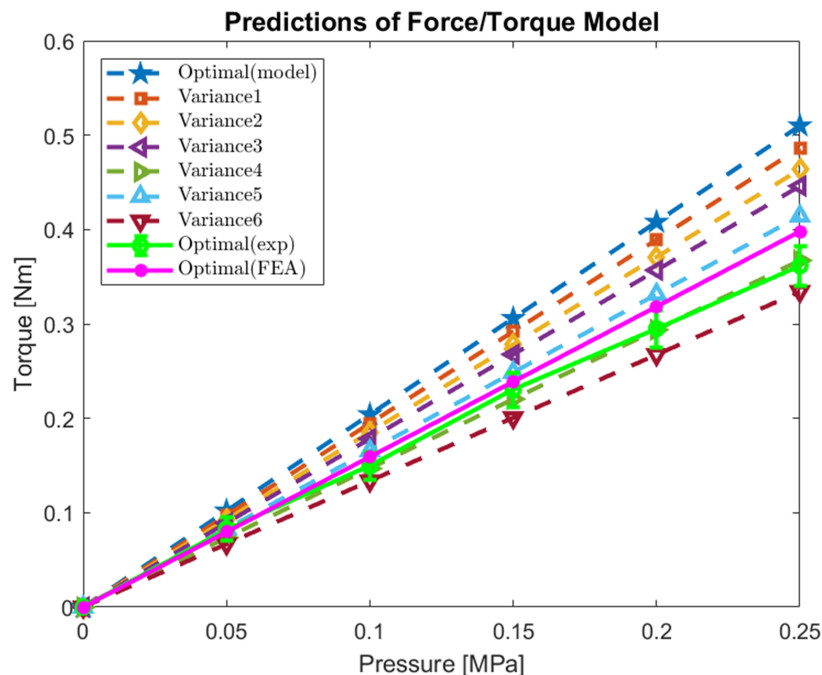
Figure 3.5: Preliminary verify the force/torque of optimal dimensional parameters using the Pressure-to-Force/Torque model and the FEA. The results are compared with the experimentation and Optimal(exp).

Preliminary Verification

This section aims to first evaluate optimal design performance and its variances in Table 3.1 and then avoid time-consuming fabrication when researchers design a soft pneumatic actuator. The popular pre-test tool for soft actuator design is the finite element method(FEA) [30, 45]. However, this research derives kinematic models of soft pneumatic actuators in Section 3.2. As the models are used to optimize the soft actuator's force/torque and bending angle in Section 3.3, the models are supposed to generate optimal force/torque and bending angle with optimal parameters. That is the combination of $\bar{T}(P)$ and $\bar{\theta}(P)$ of optimal parameters, the objective function in (3.20), is supposed to be maximum.

Note that the FEA formulation sets soft materials as an isotropic linear elastic. The elastic modulus and Poisson's ratio of the material, Smooth-on Ecoflex® Dragon skin 20, are 0.34 MPa and 0.49 [119]. The mesh size is approximately 1 mm.

Preliminary Verification of Force/Torque

The Pressure-to-Force/Torque model can evaluate the torque of soft actuators with input pressures. The model prediction, FEA, and experimentation results are displayed in Fig-
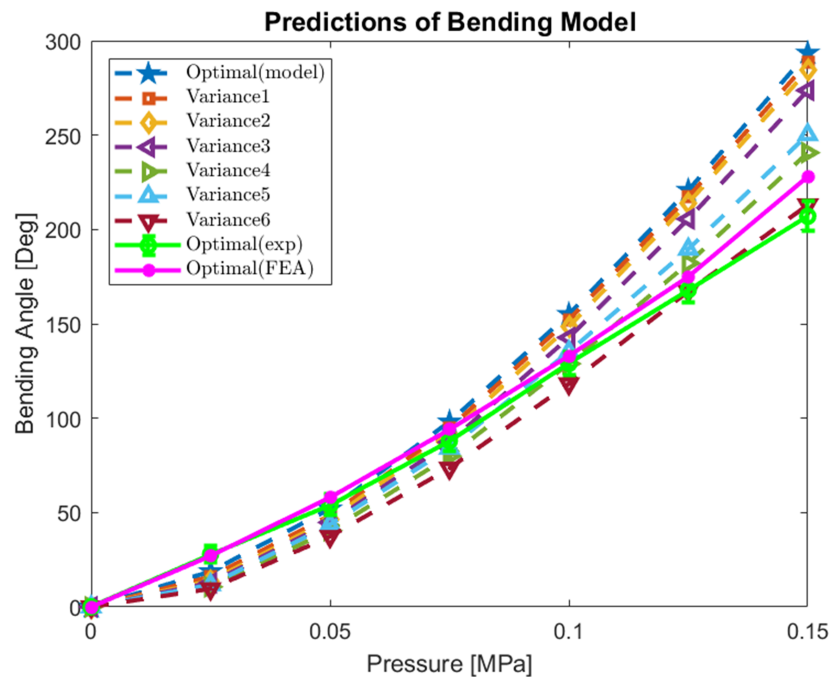
Figure 3.6: Preliminarily verification of optimal dimensional parameters' bending angle using the Pressure-to-Bending model and the FEA. The results are compared with the experimentation and Optimal(exp).

ure 3.6. Optimal design (blue solid line) outperforms all low and high-pressure variances, generating up to 0.5 Nm at 0.25 MPa. While the optimal design is superior, 'Variance 1' closely approaches its performance. Consequently, both optimal design and 'Variance 1' are selected to be fabricated and tested by experimentation.

Preliminary Verification of Bending Angle

The Pressure-to-Bending model is applied to predict the bending angles of soft actuators with input pressures. The model prediction, FEA, and experimentation results are displayed in Figure 3.7. Similarly, optimal design (the same as in Figure 3.6) outperforms all variances in low and high pressures. Optimal design generates up to 290 deg at 0.15 MPa predicted by the model. Consequently, the bending angle preliminary test also verifies the optimal design.

Based on the results of both models, the optimal parameter set (Design 1) generates a maximum combination of $\bar{T}(P)$ and $\bar{\theta}(P)$, which is 2.36 at 0.15 MPa. Because the results of Variance 1 (2.30 at 0.15 MPa) and optimal parameters are closed, both parameter sets in Table 3.1 are selected for manufacturing. Subsequently, those prototypes are utilized for

experimental validation in Section 3.4.

Study on Optimizing System's Controllability

In Section 3.3, in particular, (3.18)-(3.19), it is known that the dimensional parameters will affect the natural frequency of the soft actuator. Thus, the optimization formulation is modified as (3.20). This subsection explores the dimensional parameters' impact on the system's controllability. Generally, the multiplication of the damping ratio and natural frequency affects the system's pole location and response time based on (3.12). Since the damping ratio of the selected material is approximately 0.7, this research mainly studies the natural frequency ranging from 2 to 3.5 rad/s. Thus, the step responses of the designed SPA could be less than 2 to 3 sec by experimental tests. Four different constraint ranges of (3.21) are selected in Table 3.2. The interior-point algorithm [12] is used to search the optimal parameters with different constraint ranges of (3.21).

Table 3.2: The constraint ranges of natural frequency and the predicted natural frequencies are compared

ω_{n1} [rad/s]	ω_{n2} [rad/s]	Real ω_n [rad/s]	b [mm]	a [mm]	w [mm]	t [mm]
2.50	3.50	2.86	4.0	20.0	30.0	1.5
2.40	2.60	2.49	4.0	19.3	30.0	1.5
2.20	2.40	2.26	4.0	16.8	30.0	1.5
1.60	1.80	1.83	4.0	14.4	30.0	1.5

Various constraint ranges of (3.21) are displayed in Table 3.2. The corresponding optimal parameters are also listed in Table 3.2. Different constraint ranges of the natural frequency yield different sets of optimal parameters. The height of the soft actuator, which directly influences the moment of inertia, varies with the range of the natural frequency. Thus, the moment of inertia will influence the natural frequency as (3.18). The real natural frequency of the last prototype in Table 3.2 hit its upper limit. It is caused by applying an approximated structure in (3.20). The experimental results are demonstrated in Section 3.4. Note that real natural frequencies in Table 3.2 are obtained by system identification of the experimental step responses of those soft actuators.

Fabrication of Soft Actuator

Figure 3.7(c) gives the configuration of the proposed soft actuator. The actuator's body is primarily made of liquid rubber, specifically Smooth-on Ecoflex® Dragon Skin 20 and Smooth-on Ecoflex® Dragon Skin FX-Pro. The upper and bottom components shown in Figure 3.7 (c) are fabricated using two distinct molds, as illustrated in Figure 3.7 (a) and (b), respectively, inspired by [111].
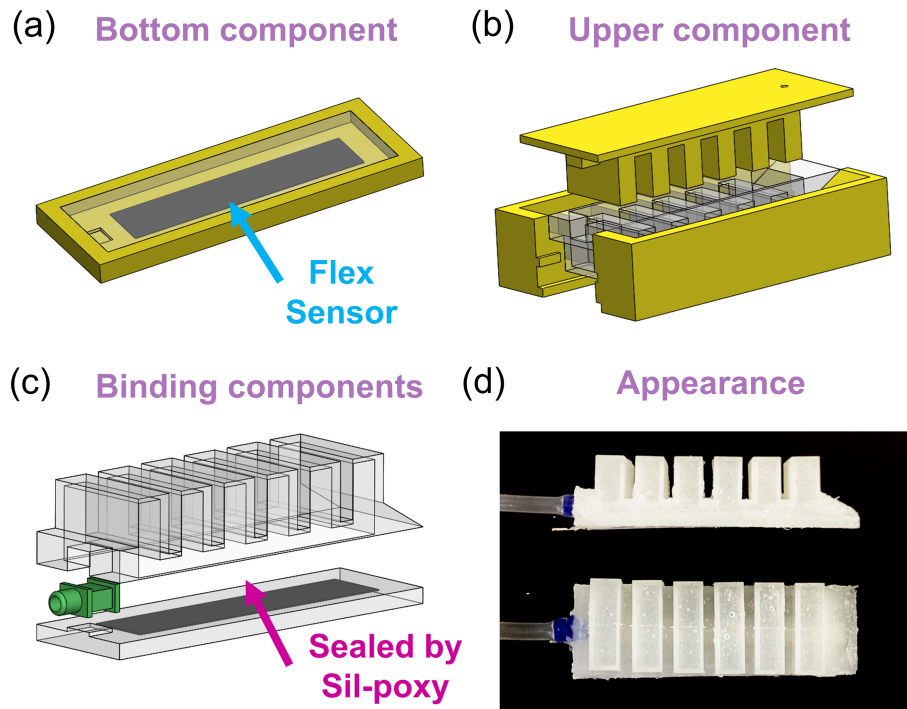
Figure 3.7: Both (a) and (b) illustrate the separate manufacturing of the bottom and upper components using distinct molds. (c) The soft actuator is demonstrated in an exploded view. The visual representation of the soft actuator's appearance can be seen in (d).

These components are then securely bonded together using the silicone adhesive, Smooth-on Sil-poxy®. The nozzle at the end is connected to a rubber tube, enabling the input of air from the syringe pump [126] into the chambers. Notably, the bottom component incorporates a flex sensor, inspired by [87, 29], which is embedded inside to regulate the position of the neutral surface. In Figure 3.3 (c), the thickness of the thin silicone layer between the flex sensor (indicated by the purple line) and the desired neutral surface (represented by the black dashed line) is precisely controlled during fabrication, ensuring a thickness of 0.5 mm. The resulting soft pneumatic actuator is presented in Figure 3.7 (d), with dimensions measuring 24 mm in height, 30 mm in width, and 94 mm in length.

Experimental Setup

The experimental setup is illustrated in Figure 3.8. The soft actuator is powered by a self-designed syringe pump, which is driven by a stepper motor. The pressure is regulated by the position of the stepper motor. Moreover, the embedded flex sensor (SparkFun Electronics, Niwot, CO) is used to monitor the bending angle of the soft actuator. To monitor the air
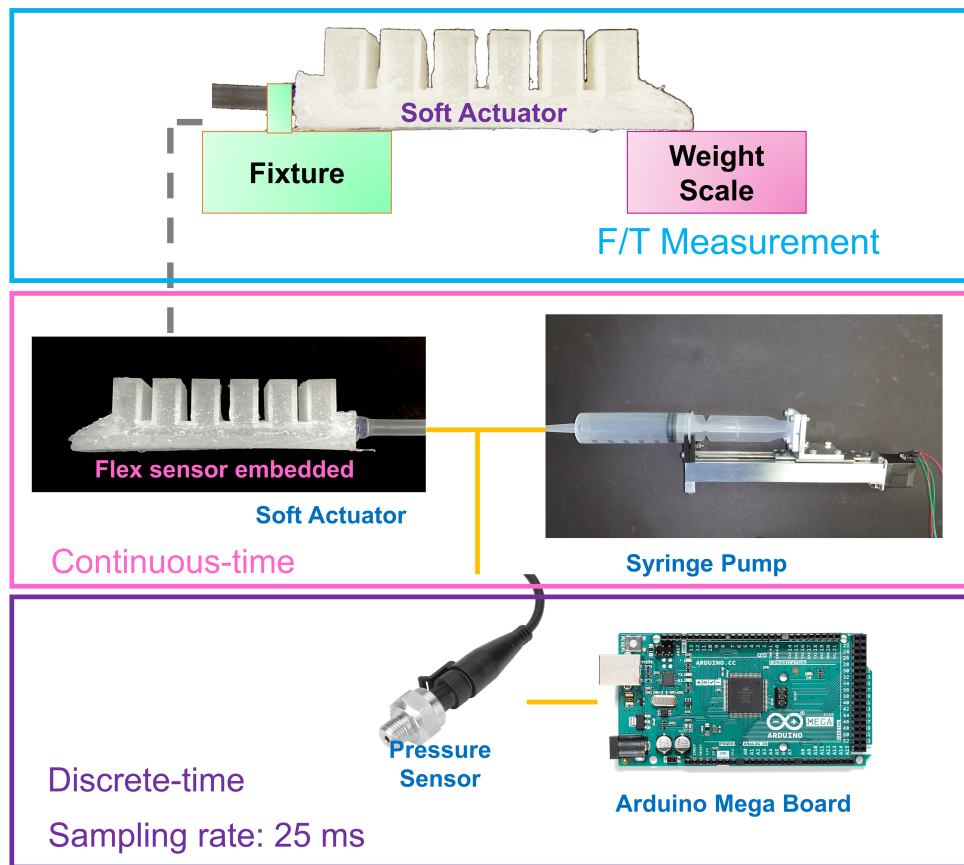
Figure 3.8: The schematic of the experimental setup.

pressure, a pressure sensor (Walfront, Lewes, DE) with a sensing range of 0 to 80 *psi* is
utilized, which is synchronized with an Arduino MEGA 2560 (SparkFun Electronics, Niwot,
CO). The microcontroller is based on the Microchip ATmega 2560 with a sampling time of
25 *ms*. Furthermore, serial communication between the microcontroller and a computer is
established by a USB cable.

Test of Torque

One of the proposed design approach's objectives is to optimize the soft actuator's output
torque. The fabricated soft actuator is fixed at the end of its structure as in the top of
Figure 3.8. The tip of the soft actuator is contacted on a digital weight scale (Etekcity,
Anaheim, CA) with a resolution of 0.01 *g* and a range of 5 *kg*. As the air pressure is pumped
into the actuator, the actuator inflates and exerts a force on the weight scale. The torque is

computed by using the equation below

$$T_m = F_m \times L_i \tag{3.24}$$

where T_m is the measured torque, F_m is the measured force, and L_i is the length of the soft
actuator. The results in Figure 3.9 show that the optimized design ('Design 1(E1)'), made
of Dragon Skin 20, matches the trend of model predictions ('Equation(E1)'). The maximum
torque of the optimal design is 0.359 Nm at the pressure of 0.25 MPa. By comparison,
the previous version [128] has a torque of 0.144 Nm at the same pressure. Note that E1
represents the Young's modulus of Dragon Skin 20, while E2 depicts that of Dragon Skin
FX-Pro.
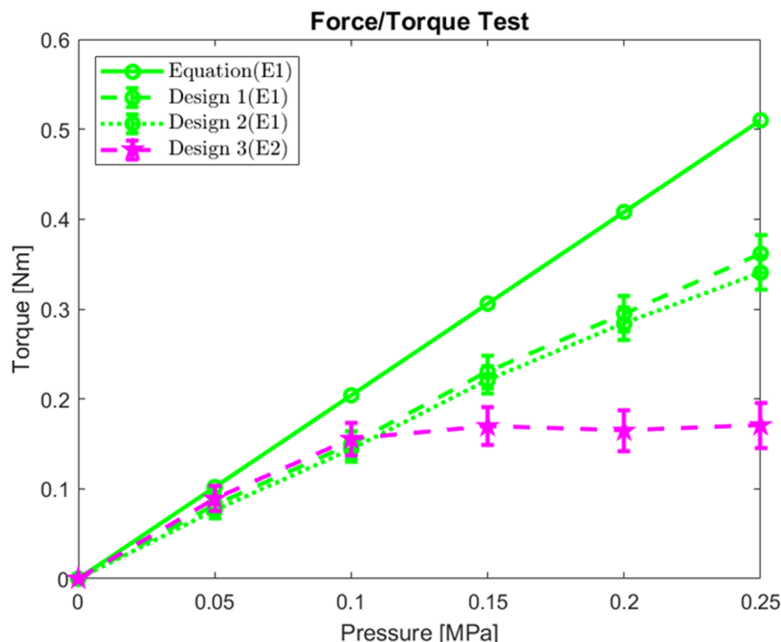
Figure 3.9: The experimental validation of optimal designed soft actuator, Design 1(E1).
Compared to Design 1(E1), Design 2(E1) has a slightly smaller width. Design 3(E2) uses a
softer material, and other dimensional parameters are the same. E1 represents Smooth-on
Dragon Skin 20, while E2 depicts Smooth-on Dragon Skin FX-Pro.

Once again, some tests are conducted on alternative designs as an initial test of their
sub-optimality, explicitly referring to 'Design 2(E1)' and 'Design 3(E2)'. In Design 2(E1) or
Variance 1 in Table 3.1, the width of the soft actuator is slightly smaller, 29 mm, in compar-
ison to Design 1(E1). The performance of Design 2(E2) drops slightly, but its performance
is close to that of Design 1(E1). In the case of Design 3(E2), Young's modulus is lower,
measuring 0.26 MPa, compared to Design 1(E1). Due to its softer nature, Design 3(E2)

experiences buckling under higher loads, resulting in a torque plateau of approximately 0.15 Nm. It is worth noting that all designs exhibit similar performance up to 0.1 MPa of pressure, indicating that the linear model assumption is most beneficial for applications under limited pressures.

Test of Bending Angle

The proposed approach also enhances the bendability of soft actuators. Also, the bending angle is another important indicator to evaluate the performance of a soft actuator [48, 110]. The flexibility of the soft actuator has been shown to have an impact on its output torque; when the actuator exhibits a larger bending angle under a fixed input pressure, it has the potential to generate higher torques [48, 110]. To test the bending angle, a defined approach is adopted as illustrated in Figure 3.2 (e), where the positions of the actuator's tip and end on a grid paper are marked. This method enables us to quantify the soft actuator's bending angle accurately.

As depicted in Figure 3.10, the results of the bending angle test reveal that Design 2(E1) exhibits a smaller degree of bendability. Design 3(E2) achieves a maximum bending angle of approximately 232 deg, whereas Design 1(E1) and Design 2(E1) reach 206 and 201 deg, respectively. The 'Equation(E1)' represents the predicted results of the Pressure-to-Bending model, considering Young's modulus of Ecoflex®Dragon Skin 20. This curve is compared with Designs 1(E1) and 2(E1), as they share the same material. In contrast, 'Equation(E2)' depicts the predicted outcomes of the model, considering the material properties of Ecoflex®Dragon Skin-FX Pro, and it is compared with Design 3(E2). Figure 3.11 illustrates the bending of 'Design 1 (E1).'

Compared to the experimental results, the predictions of the Pressure-to-Bending model underestimate low bending angles and overestimate high bending angles. However, the model still catches the trend of the bending angle of soft actuators, which is beneficial for optimization formulation. Notably, the combination of real $\bar{T}(P)$ and $\bar{\theta}(P)$ of Design 1(E1) surpasses that of Design 2(E1) and Design 3(E2). The combined values of $\bar{T}(P)$ and $\bar{\theta}(P)$ of each prototype are 1.44, 1.29, and 1.40 at 0.15 MPa, respectively. Therefore, experimental results validate the optimal design.

Verification of Natural Frequency and Pole Location

Section 3.3 and 3.4 discuss the relationship between dimensional parameters and the natural frequency. Firstly, this subsection aims to verify the accuracy of (3.16). If the error of the equation is minimal, it can serve as a reference. The error ranges from approximately 5.76 % to 16.86 % as in Table 3.3, which is influenced by the dimensional parameters and Young's modulus. Design 1(E1) and Design 2(E1) have the same shape, height, and wall thickness but have different widths. Design 2(E1) has the most minor error, 5.76 %. The softer the materials, the larger the errors of (3.16). For example, Design 3(E2) has an error of 16.86 % because its structure will buckle.
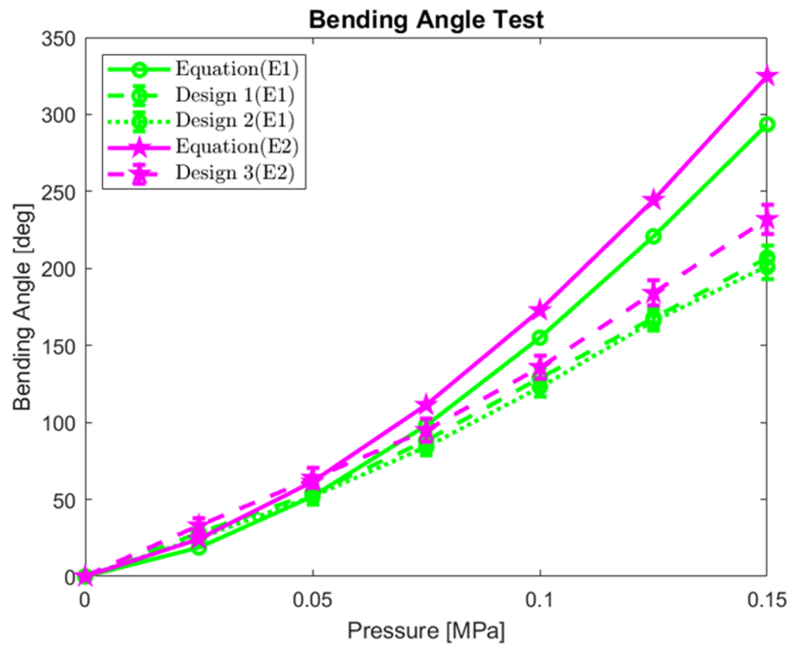
Figure 3.10: The test results for the bending angles of all designs are presented. 'Equation
(E1)' predicts the bending angles of the soft material used in the production of Design
1(E1) and Design 2(E1). 'Equation (E2)' simulates the bending angles of the soft material
employed in the fabrication of Design 3(E2).
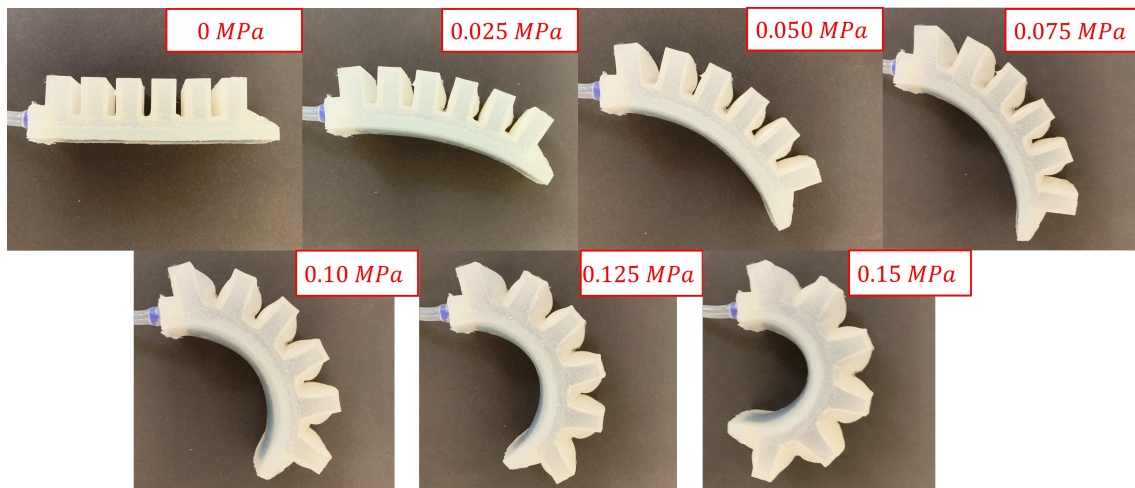
Figure 3.11: The visualization of the bending of the Design 1(E1) with various pressure from
0 MPa to 0.15 MPa.

Table 3.3: Comparisons of true natural frequencies and the estimations by the (3.16)

Unit [rad/s]	True ω_n	Estimated ω_n	Error
Design 1(E1) (E=0.34MPa, M=0.35N, L=0.94m)	2.86±0.052	2.62	8.39%
Design 2(E1) (E=0.34MPa, M=0.34N, L=0.94m)	2.78±0.048	2.62	5.76%
Design 3(E2) (E=0.26MPa, M=0.46N, L=0.94m)	1.72±0.061	2.01	16.86%

Then, the experiments are conducted to validate if the natural frequency lies within the desired range. In Table 3.2, the optimal parameters are obtained with a constraint range of natural frequency between 2.5 and 3.5 rad/s. The corresponding pole location of the SPA lies between -2.45 and -1.75. A second-order system identification over the responses of the soft actuator measures the actual natural frequency. The natural frequency is 2.86 rad/s as in Table 3.2. The complex pole locations are -1.99 ± j2.04. The other prototypes in Table 3.2 are also verified by experimentation. The natural frequency lies either within or close to the desired range. Therefore, the results show that the natural frequency and the pole location lie in the desired range.

Soft Actuator Control

Firstly, the (3.12) is linearized for controller design, which is valid even during a 90-degree bending. The damping ratio of the soft actuator is 0.7 ± 0.1 obtained by second-order system identification. The natural frequency is estimated by (3.16). The F in (3.11) is generated by input pressure P. Then, we have the dynamic model of the soft actuator with all the parameters in (3.12). In addition, the system is driven by a syringe pump which is a first-order system [126]. The full model, thus, is a third-order system as below.

$$T_{SYS} = \frac{lA_s\omega_m c/2\pi C_s M}{s^3 + 2\zeta\omega_n s^2 + \omega_n^2 s} \tag{3.25}$$

where Q_s is the air output flow rate of the syringe, A_s is the inside cross-sectional area of the syringe, C_s is the capacity of the soft actuator, ω_m is the motor speed, and c is a constant obtained by experimentation.

Since the full system is controllable and observable, a linear quadratic regulator (LQR) is employed because it can advantageously satisfy key performance specifications such as settling time and steady-state errors. The controller is implemented into a microcontroller equipped with a saturation to account for the motor's speed limit of 5 rev/s.

The state vector $\mathbf{x} = [\theta \ \dot{\theta} \ \ddot{\theta}]^T$ is defined. The full system model is then reformulated into a controllable canonical form as follows:

$$\dot{x} = \mathbf{A}x + \mathbf{B}u \tag{3.26}$$

$$y = \mathbf{C}x \tag{3.27}$$

with matrices defined as:

$$\mathbf{A} = \begin{bmatrix} 0 & 1 & 0 \\ 0 & 0 & 1 \\ 0 & -{\omega_n}^2 & -2\zeta\omega_n \end{bmatrix}, \mathbf{B} = \begin{bmatrix} 0 \\ 0 \\ 1 \end{bmatrix}, \mathbf{C} = \begin{bmatrix} \frac{lA_s\omega_m c}{2\pi C_s M} \\ 0 \\ 0 \end{bmatrix}^T \tag{3.28}$$

With the directly measurable, via embedded flex sensor, θ and robust differentiation methods for approximating $\dot{\theta}$ and $\ddot{\theta}$ [60] with the sampling time of 25 ms, LQR control emerges as a viable and effective solution.

The LQR design aims to determine an optimal state-feedback controller, u, by minimizing a quadratic cost function of the form $J = \int_0^\infty (x^T Q x + u^T \mathbf{R}u)dt$. This objective function signifies the trade-off between striving to achieve desired state values and expending control effort. The scalar $\mathbf{R}$ and the matrix Q in the cost function are weighting factors that can be adjusted to prioritize control effort versus state deviations. In particular, the diagonal elements of Q are chosen to penalize the deviation of states from their desired values. The off-diagonal elements of Q would introduce coupling between the states in the cost function, but they are kept zero for simplicity.

For the system, $\mathbf{R}$ is set to 1, and Q is defined as follows:

$$Q = p \begin{bmatrix} 1 & 0 & 0 \\ 0 & 0.3 & 0 \\ 0 & 0 & 0 \end{bmatrix} \tag{3.29}$$

With $p \in \mathbb{R}_+$, this choice of Q represents the independent treatment of each state. The highest weight is assigned to the bending angle θ, reflected by the first diagonal element. The speed of bending $\dot{\theta}$, although important, is considered less significant, as shown by the second element set to 0.3. The third diagonal element set to 0 indicates the changes in the acceleration $\ddot{\theta}$ is not penalized. The scalar $p = 100$ allows for global adjustment of state deviation tolerance against control effort. Depending on the system requirements, p can be increased or decreased. This decision hinges on whether to heavily penalize state deviations (with a larger p) or maintain low control effort (with a smaller p). The choice of Q should be customized based on the system's unique needs and may require iterative tuning for optimal performance.

Upon obtaining Y by solving $\mathbf{A}^T Y + Y\mathbf{A} - Y\mathbf{B}\mathbf{R}^{-1}\mathbf{B}^T Y + Q = 0$, the state-feedback controller is obtained as follows:

$$u = -\mathbf{R}^{-1}\mathbf{B}^T Y\mathbf{x} \tag{3.30}$$

Since the system is controllable and observable, that implies $Y > 0$ and ensures the stability of the system [92].

Figure 3.12 (a) and (b) depict the block diagram and experimental step response of the Design 1(E1), respectively. The LQR controller exhibits prompt and accurate response characteristics, with a settling time of approximately $0.8\ sec$ and an almost negligible steady-state error. These characteristics validate the LQR controller's ability to handle the presence of noise and system delays, as observed in our experiments, ensuring that the experimental results align closely with simulation results.
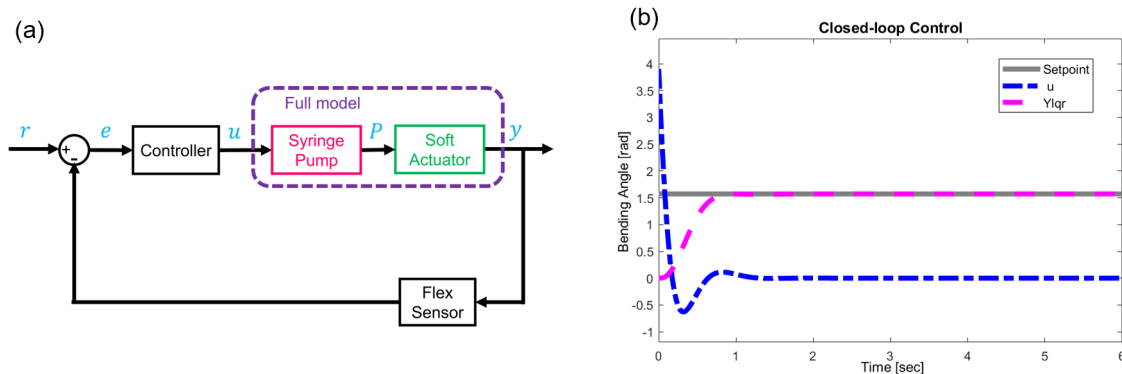
Figure 3.12: (a) The control block diagram of a real experiment is visualized. (b) The pink dashed line displayed the step response of the soft actuator(Design 1(E1)) controlled by the LQR controller, and the blue dashed line showed the control commands(u) of LQR from the microcontroller in Figure 3.8, and the gray solid line represented the reference.

3.5 Discussion and Summary

Discussion

The system parameter in (3.12) correlates with the dimensional parameters such as width, height, and wall thickness. The variations of the dimensional parameters will influence the natural frequency of the system. Thus, the constraint space of the optimization formulation of (3.16) is extended to place the natural frequency. The influence of the dimensional parameters is examined in Section 3.4. If the constraint space changes, the dimensional parameter, especially the height, will vary accordingly. The natural frequency will be moved as well.

The optimal designs in Table 3.2 barely excite the second natural frequency since it is far
away from their first natural frequency. Overall, this approach can not only enhance the
force/torque and bending angle of the soft actuator but also place the pole location of the
system. That is, this approach can determine the dynamical property in the design stage.

The performance indices of this design are compared with those of other designs presented
in the literature, as shown in Table 3.4. Since the dimensions of the soft actuators influence
their performance, including factors such as force/torque and bending capabilities, the table
includes only designs with comparable dimensions. The distinctive feature of this design is its
comprehensive approach, particularly its focus on multiple metrics, with a special emphasis
on controllability.

Table 3.4: The comparisons of this design with others in the literature. The considered
metrics include force/torque, bending angle, and controllability. ("N/A" represents the
design does not consider the metric.)

Design Approach	Force/Torque [Nm]	Bending [deg]	Controllability
Model-based optimization [127]	0.359	206	Included
Model-based optimization [128]	0.144	214	N/A
Machine learning + Finite element [22]	0.150	120	N/A
Mechanical design [64]	0.158	68	N/A
Model-based optimization [67]	0.332	270	N/A
Finite element method [87]	0.165	320	N/A
Finite element method [74]	0.450	150	N/A
Finite element method [78]	1.163	180	N/A
Finite element method [73]	$\sim$0.140	> 270	N/A

Since the natural frequency of the soft actuator varies with the dimensional parameters,
the constraints of dimensional parameters should be changed with the range of the natural
frequency. In Table 3.2, the dimensional parameter a exhibits a strong correlation with
the natural frequency range, thereby establishing its crucial role in the actuator design.
For instance, when the natural frequency range was defined as 3.0 to 3.5 rad/s, the actual
natural frequency deviated, reaching approximately 2.9 rad/s. Thus it was attributed to a
being at the threshold of its defined limit, 20 mm. To address this discrepancy and align
the natural frequency with the desired range, an adjustment was required in the parameter
a. Consequently, extending the upper limit of a to 24 mm successfully tuned the natural
frequency to the desired value of 3.15 rad/s. This underscores the importance of the iterative
adjustment of parameters in achieving optimal performance, particularly when it comes to
satisfying the constraints related to the natural frequency of the actuator.

Besides, Young's modulus of soft materials affects the bending angle and natural fre-
quency of soft actuators. According to (3.10), Young's modulus should be small to optimize
the bending ability of soft actuators. If the constraint of Young's modulus is added, it always
hits the lower bound. Meanwhile, Young's modulus, influenced by a, b, and w, is supposed

to be at a certain range to achieve the desired dynamical properties by (3.21). This will
lead to no solution when the intersection of (3.21) and the constraint of Young's modulus is
empty. In other words, the optimal Young's modulus cannot be found by the optimization
algorithm. Another issue is that smaller Young's modulus will cause soft actuators to buckle
as the Design 3(E2) in Figure 3.9. Therefore, equation (3.20) does not include the constraint
of Young's modulus, which is suggested to be selected by designers.

Last but not least, the number of chambers has an influence on the force/torque and
bending angle of soft actuators in different ways. Based on (3.10), an increase in the number
of chambers (longer L_i) enhances the bending ability of soft actuators. Even if the number of
chambers (L_i) does not affect the generated torque by referencing (3.4), an increased number
of chambers will result in the buckling of soft actuators. Thus, the generated torque will reach
a plateau above a specific pressure value, which is similar to Design 3(E2) in Figure 3.9. Since
the number of chambers influences force/torque and bending angle differently, this research
does not add the number of chambers as a constraint in (3.20). Instead, the designs in this
chapter maintain a fixed number of chambers and manage the length of soft actuators to be
approximately 100 mm, so those soft actuators can avoid the buckling issue.

Summary

The chapter introduces an innovative approach to optimize the design of soft pneumatic
actuators, focusing on enhancing force/torque, bending angle, and improving the system's
controllability. A cantilever beam approximation is implemented to analyze the complex
structure of SPAs. This approximation allows for the derivation of both nonlinear kinematic
and dynamic models. The design problem is converted to an optimization problem, with the
kinematic models serving as the objective function, and the dynamical model as a constraint.
This approach leads to the determination of optimal dimensional parameters for SPAs. To
validate the effectiveness of the proposed method, preliminary verification and several ex-
periments are conducted. The optimal soft actuator demonstrates the ability to generate a
torque of up to 0.359 Nm and a bending angle of 206 deg, while its natural frequency falls
within the desired range. The output force/torque and bending angle outperform that of
our previous design. Lastly, an optimal controller is designed to control the system which
achieves 0.8 sec settling time and almost 0 steady-state error. The relationship between
dimensional parameters and natural frequency has been studied and discussed. This opti-
mal model-based design strategy presents a novel method to enhance multiple performance
indexes of the soft pneumatic actuator. Since the optimal soft actuator design method is
proposed and verified, the next step is to design the syringe pump to drive the soft actuator.

Chapter 4

Design, Modeling, and Control of a Syringe Pump

4.1 Introduction

The compliant soft robots are favorable to work in complex and clustered environments [51, 129], ensure the safety of human-robot collaboration [22], and help them handle delicate objects in the food industry [77]. Instead of traditional motors, soft robots are actuated by electroactive polymers, cable-driven, shape memory alloys, or pneumatic actuators [133]. Among those choices, pneumatic actuators are becoming the preferred option to drive soft robotic systems [133, 50] because they have light weights, reasonable costs, and high power density. An optimal soft pneumatic actuator is designed and introduced in Chapter 3.

Despite their advantages, control and actuation of soft pneumatic actuators are still a challenge [91]. Since the pneumatic actuators rely on pressurized air to adjust their motions (bending angle), the common actuation strategies include an air pump with the pressure regulator and a solenoid valve [121, 109, 96] or syringe pump made of a linear actuator and a commercial syringe [55, 116]. The former method has an extensive operating range. It generates sufficient air pressure to drive soft actuators, but the control of the solenoid valve is relatively complex, and the air pump is bulky. The latter provides precise differential pressure control and is easier to control. Although the syringe's volume limits the operational range, this drawback can be mitigated by using a larger syringe [121]. Furthermore, several dynamic models for soft pneumatic actuators have been developed, but they are unable to catch all the motions. The errors are caused by ignoring the dynamics of pneumatic supply systems. The nonlinear and unpredictable pressure dynamics should also be considered, especially when designing controllers for soft actuators [120, 109]. Therefore, the controllers can regulate the errors, and systems can achieve higher accurate dynamics.

This chapter focuses on modeling and parametric analysis of a syringe pump to optimize its design parameters and output responses. First, a syringe pump is designed, and then its pressure dynamic model is built. According to the pressure model, the parametric analysis

is conducted to verify the derived dynamic model. Also, the optimal design parameters are determined, and the corresponding components, such as the linear actuator, size of the commercial syringe, and stepper motor, are chosen to build the system. Lastly, the pressure model includes a time-dependent parameter, the volume of the soft actuator, since it will change with the input pressure. The Kalman filter is used to estimate the volume change of the soft pneumatic actuator, enabling precise prediction of the system dynamics. The syringe pump is applied to drive a self-built soft actuator [128].

Several works have proposed a pressure dynamic model for pneumatic systems and the applications of the syringe pump. Kalisky et al. [55] implemented a set of syringe pumps to control a soft robot with three channels. The syringe pumps achieved differential pressure (small motions) control. However, this work did not consider the system's dynamic pressure model, which influenced the performance of the designed controller. Xavier et al. [71, 120] developed pressure dynamic models for their pneumatic supply systems. The controllers, which regulated the soft actuator's motions precisely, were designed based on the actuator's and pressure models. However, their pneumatic supply systems differed since they used an air pump with a pressure regulator and a solenoid valve. Besides, the volume of the soft actuator was time-dependent, which decreased the model's accuracy. This issue was solved using a buffer tank (increasing the volume), so the volume change is negligible. By contrast, this work utilizes the Kalman filter to estimate the volume change of soft actuators. Moreover, it has been discovered that volume change is related to the bending angle, which is used in the Kalman filter to estimate the desired state. Thus, the buffer tank is not needed. Joshi et al. [53] conducted the parametric analysis and optimized the design parameters. This research is similar but different in some aspects. The pressure dynamic model is derived, and the parametric optimization is conducted based on the model. Also, the configuration of our pneumatic supply system and design parameters are quite different. In addition, recent research [14, 24] proposed electro-pneumatic pumps that were compact and portable for the actuation of soft robots. Unfortunately, those pumps could not provide enough pressure ranges to actuate general soft actuators. Overall, this research intends to derive the pressure dynamic model for the syringe pump, optimize the system's parameters according to the model, and design an appropriate controller considering the pressure model. Thus, the derived model not only accurately predicts system dynamics but also aids in designing suitable controllers for soft actuators.

The remainder of this chapter is organized as follows. Section 4.2 introduces the derivation of the pressure dynamic model and parametric analysis. Section 4.3 discusses controller design based on the derived dynamic model. Section 4.4 demonstrates the experimental results, and Section 4.5 concludes the work.

4.2   System Design and Dynamic Modeling

The main configuration of the syringe pump includes a syringe and a linear actuator, as in Figure 4.2. The commercially available syringe can store air, which acts as the air pump
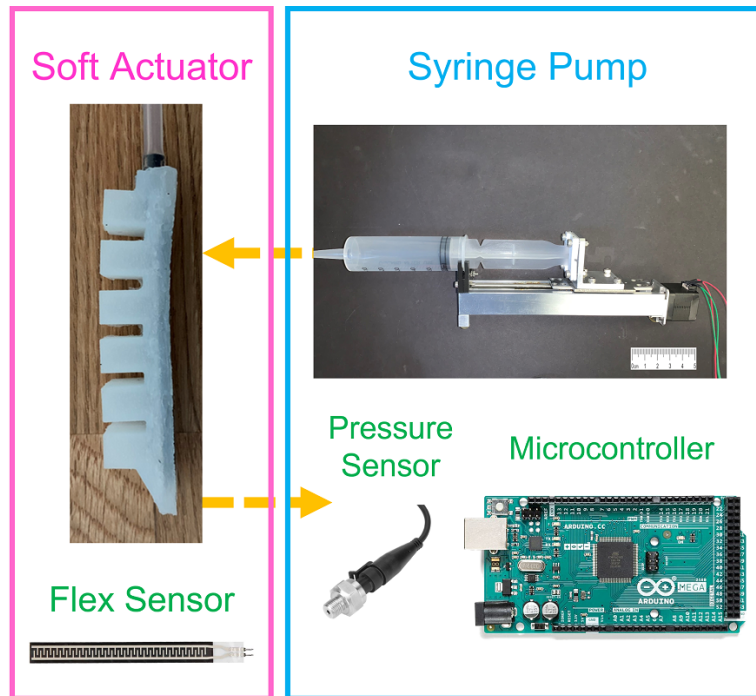
Figure 4.1: The configuration of the syringe pump (with scale bar), soft actuators, and the sensors such as flex and pressure sensors. The controller is programmed using the Arduino Mega board.

tank, but it has a smaller capacity and is not bulky. The slider of the linear actuator is connected to the syringe, and the linear actuator, driven by the stepper motion, can push and pull the syringe to regulate the air pressure inside the soft actuator.

System Modeling

Next, the dynamics of the syringe pump are modeled to do the parametric analysis and select an optimal size of the syringe, a suitable linear actuator, and the stepper motor. The modeling process begins with the linear actuator. The velocity of the slider on the linear actuator is influenced by the screw's lead inside the linear actuator and the speed setting of the motor speed, so the equation is described as

$$v_s = \frac{l}{2\pi}\omega_m \tag{4.1}$$

where v_s is the velocity of the slider in the linear actuator, l is the lead of the screw inside the linear actuator, and ω_m is the motor speed. As the slider moves, the air flows from the syringe to the soft actuator. The output air flow rate is
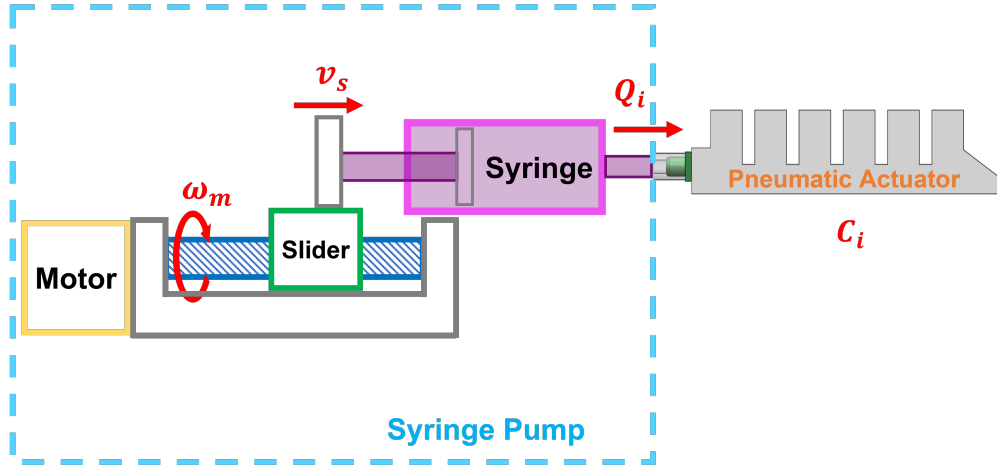
Figure 4.2: The structure of the syringe pump. It is mainly composed of a linear actuator driven by a stepper motor and a commercial syringe. The parameters used to derive the dynamic equation are labeled.

$$Q_i = Av_s = \frac{Al}{2\pi}\omega_m \tag{4.2}$$

where Q_i is the output air flow rate of the syringe, and A is the cross-sectional area of the syringe. The idea gas law indicates that $PV = nRT$.

$$PV = nRT \tag{4.3}$$
$$\Rightarrow P = nRT/V \tag{4.4}$$

where R is a constant, V is the volume of the container, n is the amount of air, and T is the chamber temperature, which is assumed in thermal equilibrium with the environment, so it could be considered as a constant. Taking derivative of (4.4), it is obtained that $\dot{P} = \dot{n}(RT/V)$. Similarly, the pressure changing rate is obtained

$$\dot{P} = \frac{Q_i}{C_i} = \frac{Al}{2\pi C_i}\omega_m \tag{4.5}$$

where C_i is the capacity of the soft actuator. The C_i is assumed to be a constant. Since the volume of soft actuator will vary, it will be justified in Section 4.4. This equation describes the pressure changing rate in the chambers of the soft actuator.

Design Parameter Analysis

Based on the (4.5), the equation consists of A, l, ω_m, and C_i as shown in Figure 4.2, which influence the pressure changing rate in the soft actuator. The capacity of the soft actuator will change with the input pressure, so we temporarily assume it is a constant in the analysis stage. This issue will be addressed in Section 4.3. The remaining parameters, A, l, and ω_m, represent the size of the syringe, screw lead of the linear actuator, and speed of the stepper motor inside the linear actuator, respectively. Different sizes of syringes and distinct leads of linear actuators are chosen to analyze the (4.5). The motor speed can be adjusted by setting the controller under the motor's speed limit.

Two variations for every parameter are chosen. Specifically, two linear actuators (Fulride and Monocarrier by NSK Ltd.) are selected. The Fulride has a screw lead of 8 mm, and the Monocarrier has a lead of 2 mm. Since there is the need for differential control of air pressure, it is not ideal to select the linear actuator with a large screw lead such as 20 or 30 mm. Another consideration is that a high-turnover motor is needed if a large lead is chosen. A higher torque motor usually has a slower speed and would reduce the pressure changing rate. Because of the sizes of the Fulride and Monocarrier, two commercial syringes whose volumes are 60 mL and 200 mL, respectively, are chosen. Larger or smaller volume syringes cannot fit into the selected linear actuators. Last but not least, the size of the stepper motor is also constrained by the selected linear actuators. The NEMA 17 stepper motor is chosen to drive the linear actuators.

Table 4.1: The variants of the parameters of pressure dynamic model

	$A[m^2]$	$l[m]$	$\omega_m\ [rev/s]$
Parameter 1	6.61e-4	0.008	1.65
Parameter 2	16.62e-4	0.002	3.30

The design parameters are shown in Table 4.1. The analytical results of the derived model are displayed in Figure 4.3 which is simulated by using MATLAB®. The default parameter set (blue lines in Figure 4.3) is $A = 6.61\text{e-}4\ m^2$, $l = 0.008\ m$, and $\omega = 1.65\ rev/s$. The analysis is conducted by changing A, l, and ω_m separately as Figure 4.3(a), (b), and (c). From the simulation results, the larger the cross-sectional area (A), the screw lead (l), and the motor speed (ω), the higher the pressure changing rate. Higher pressure changing rates could enable faster and more efficient responses of the soft actuator. Thus, the optimal parameter set is $A = 16.62\text{e-}4\ m^2$, $l = 0.008\ m$, and $\omega = 3.3\ rev/s$. Nonetheless, the higher cross-sectional area of the syringe will generate a larger reverse force if the pressure inside the soft actuator increases as discussed in Section 4.4. To deal with this problem, a high-torque stepper motor is required. Unfortunately, a high-torque motor usually has a slower operating speed. Therefore, the solution here is choosing a syringe with 60 mL whose cross-sectional area is smaller. The comparisons between analysis and experimental results will be introduced in Section 4.5.
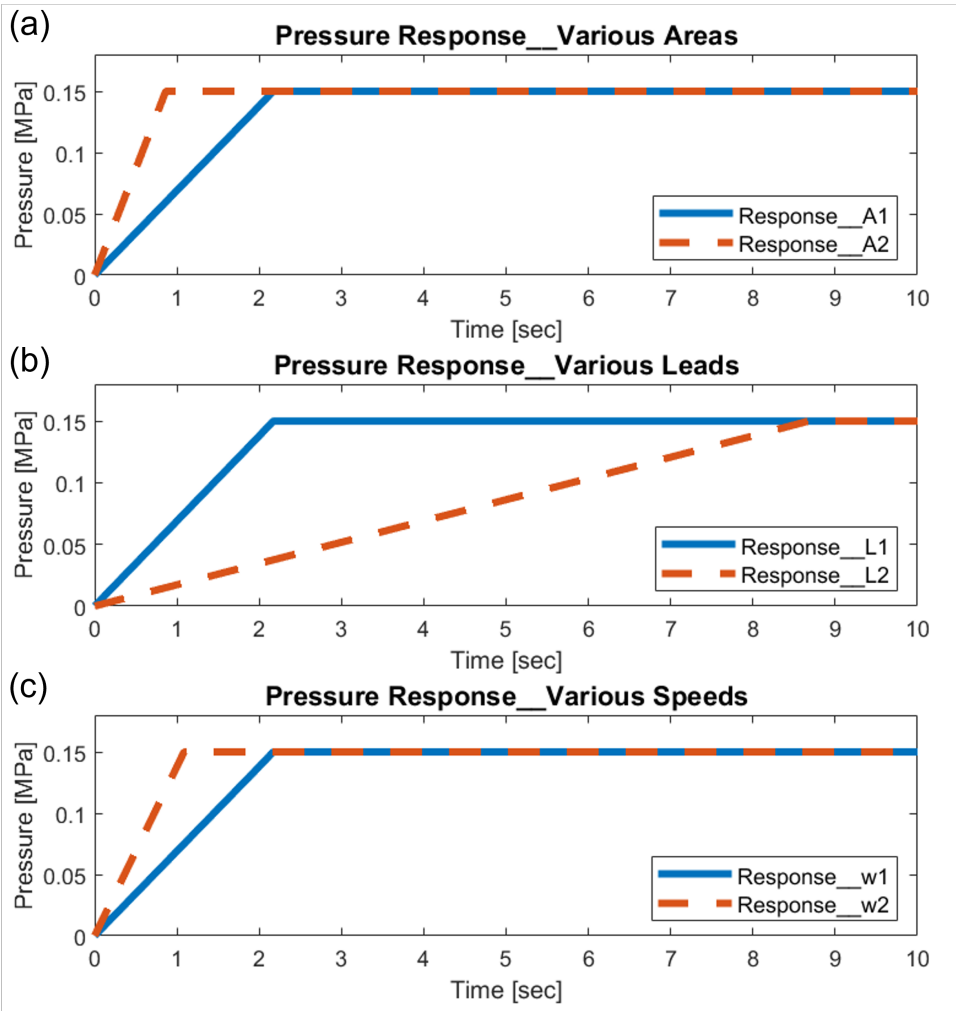
Figure 4.3: (a) The responses of syringe pumps with different cross-sectional area of syringes. (b) The responses of pumps with distinct screw leads of linear actuators. (c) The responses of a pump with different motor speeds.

4.3 Controller Design

The dynamic model of the air supply system is derived in Section 4.2. The transfer function can be obtained by taking the Laplace transform of (4.5)

$$\frac{\boldsymbol{P}}{\boldsymbol{\Omega_m}} = \frac{Al}{2\pi C_i} \frac{1}{s} \tag{4.6}$$

where $\boldsymbol{P}$ is the P in the Laplace domain, and $\boldsymbol{\Omega_m}$ is the ω_m in the Laplace domain. For simplicity and feasibility of analysis, the capacity of the actuator C_i is assumed as a constant, as discussed in Section 4.2. However, the volume of the soft actuator varies with the pressure. The following subsections will handle this issue.

Modified Model

The prediction of (4.5) (blue solid line) differs from the true response (red dashed line) as in Figure 4.4 (a). It is caused by the capacity change, so the model is modified by changing the C_i as the $C_i + c \cdot Q_i t$ because the C_i will change with Q_i and the (4.5) becomes

$$\dot{P} = \frac{Q_i}{C_i + cQ_i t} = \frac{Al}{2\pi(C_i + c\frac{Al}{2\pi}\omega_m t)}\omega_m \tag{4.7}$$

where c is a constant and is larger than 0 and smaller than 1 and the system's transfer function becomes

The pressure response of (4.7) (green dashed line) has been corrected, especially when the pressure is above 0.1 MPa. Unfortunately, the errors still exist compared to the true system response. The modified model tends to overestimate the capacity changes at higher pressures ($> 0.10\ MPa$). The error is around 10 % when pressure exceeds 0.10 MPa as in Figure 4.4 (a).

Kalman Filter Estimation

According to Figure 4.4 (a), the (4.7) is still unable to catch the dynamics accurately due to the imprecise estimations of the actuator's volume changes. Another solution is applying the state estimator, Kalman filter, to deal with this problem. The Kalman filter is an algorithm that uses the system's measurements to estimate unknown variables [114, 125]. Thus, the Kalman filter is implemented to estimate the time-varying capacity change during operations. What's more, it is observed that the capacity of the soft actuator relates to its bending angle. The capacity change is assumed to have a linear relationship with the capacity. The state vector includes capacity and bending angle, so the state space equation is
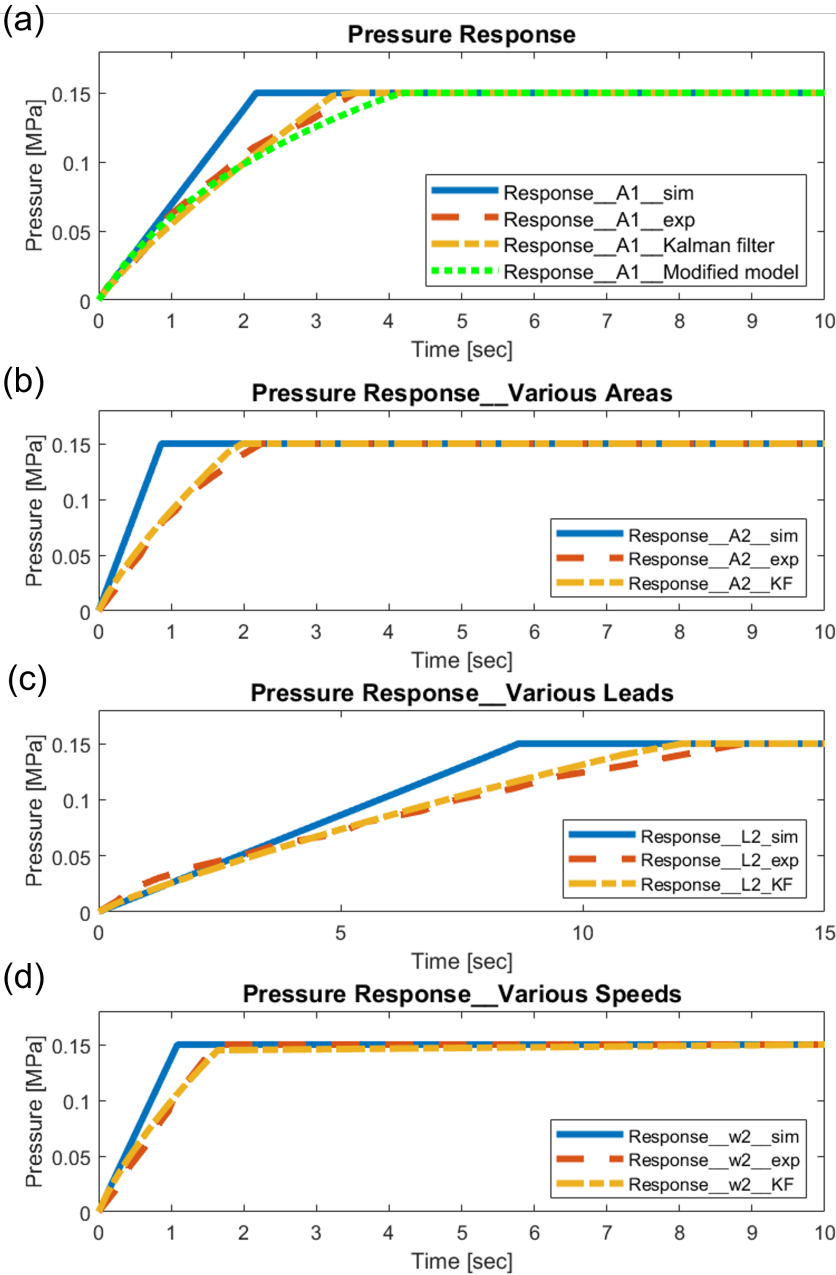
Figure 4.4: (a) The responses of the syringe pump's different models are compared. (b) The simulation and experiment involve using a larger syringe (larger A). (c) The simulation and experiment of the pump using a smaller screw lead of linear actuator. (d) The simulation and true responses of the system using higher motor speed.

$$\boldsymbol{x}_{K+1} = A\boldsymbol{x}_k + w_k \tag{4.8}$$

$$\boldsymbol{z}_{k+1} = H\boldsymbol{x}_k + v_k \tag{4.9}$$

where

$$\boldsymbol{x} = \begin{bmatrix} C_i \\ \theta \end{bmatrix}, A = \begin{bmatrix} 1 & k \\ 0 & 1 \end{bmatrix}, H = \begin{bmatrix} 0 & 1 \end{bmatrix}, \tag{4.10}$$

where k is a constant. The Kalman update process [114, 125] is operated to estimate the instant volume of the soft actuator based on the state space equation (4.9) and (4.10).

The Kalman filter estimation (yellow dashed line) is demonstrated in Figure 4.4 (a). The estimation nearly matches the true response of the syringe pump (red dashed line). The error, compared to the true response, is within 5 %. Thus, the Kalman filter is included in the control block diagram as Figure 4.6 (a). The syringe pump generates pressure to bend the soft actuator. The bending angle of the soft actuator is measured by an embedded flex sensor [38]. Then, the Kalman filter estimates the volume of the soft actuator by using the measured bending angle.

Dynamic Model of Soft Actuator

The syringe pump aims to control soft actuators. A soft actuator, which is optimally designed in Chapter 3 and manufactured in the previous work [128], is used to validate the accuracy of pressure dynamics. The dynamics of the soft actuator can be approximated as a second-order system [120]. The damping ratio and natural frequency are obtained by fitting the system's responses. The equation of the soft actuator is described as

$$\theta(t) = C_0 + C_1 e^{-at} + C_2 e^{-bt} \tag{4.11}$$

where C_0, C_1, and C_2 are constant coefficients, and a and b are related to time constants. Consequently, the dynamic equation can be rearranged as

$$\ddot{\theta} + (a+b)\dot{\theta} + (ab)\theta = F/M_{eq} \tag{4.12}$$

$$\ddot{\theta} + 2\zeta\omega_n\dot{\theta} + \omega_n{}^2\theta = F/M_{eq} \tag{4.13}$$

where ζ is the damping ratio, ω_m is the natural frequency, M_{eq} is the equivalent mass of the soft actuator and is obtained by applying system identification in MATLAB®, and F is the force at the tip of the actuator. By the linear model assumption, the F is assumed to have a linear relationship ($P \leq 0.15 MPa$) with the pressure P controlled by the syringe pump, $F = C \cdot P$. (When the material used to make a soft actuator deforms below 100 %, its deformation is still linear [119].) The parameter C is a constant obtained by experiments.

After taking the Laplace transform, the (4.13) is shown as

$$T_{spa} = \frac{C \cdot P / M_{eq}}{s^2 + 2\zeta\omega_n s + \omega_n{}^2} \tag{4.14}$$

The full model is the combination of the pressure dynamic model and the soft actuator's bending model.

$$T_{full} = \frac{lA\omega_m C / 2\pi C_i(t) M_{eq}}{s^3 + 2\zeta\omega_n s^2 + \omega_n{}^2 s} \tag{4.15}$$

where $C_i(t)$ is the time-varying parameter estimated by the Kalman filter. The equation is the third-order system.

PID Controller Design

Two PID controllers are designed for the (4.14) and (4.15) separately. The Ziegler-Nichols tuning method is implemented to design the proportional-integral-derivative(PID) controller for the pneumatic control system [2]. The time response tuning of Ziegler-Nichols is used. Trial-and-error is used to fine-tune the gains after obtaining the PID gains by the Ziegler-Nichols.

The simulations of the controllers are done in MATLAB®/Simulink to test the performance of the controller and system preliminarily. The step responses of the pneumatic with two PID controllers are displayed in Figure 4.5 (a) and (b). The controller based exclusively on the actuator's model achieves a steady state in about 5 *sec*. By contrast, the controller based on the full model has a settling time of around 2.5 *sec*. Thus, the pressure dynamics do influence the performance of the controller. Note that the volume of the soft actuator is assumed to be the initial value when designing the PID controller.

4.4 Experimental Evaluation

This section will verify the parameters determined in Section 4.2, and compare them with the experimental results. Also, the syringe pump is used to control a soft actuator to validate the influences of pressure dynamics on the controller design.

Hardware System Setup

Syringe Pump Setup

Since the parameters are determined, the corresponding components are the Fulride linear actuator (l=8 *mm*), a syringe of 60 *mL*, and a Nema 17 stepper motor. While the linear actuator limits the size of the stepper motor, the speed can be adjusted. Those components are assembled by using several 3D printed components and can be seen in the upper right of Figure 4.1.
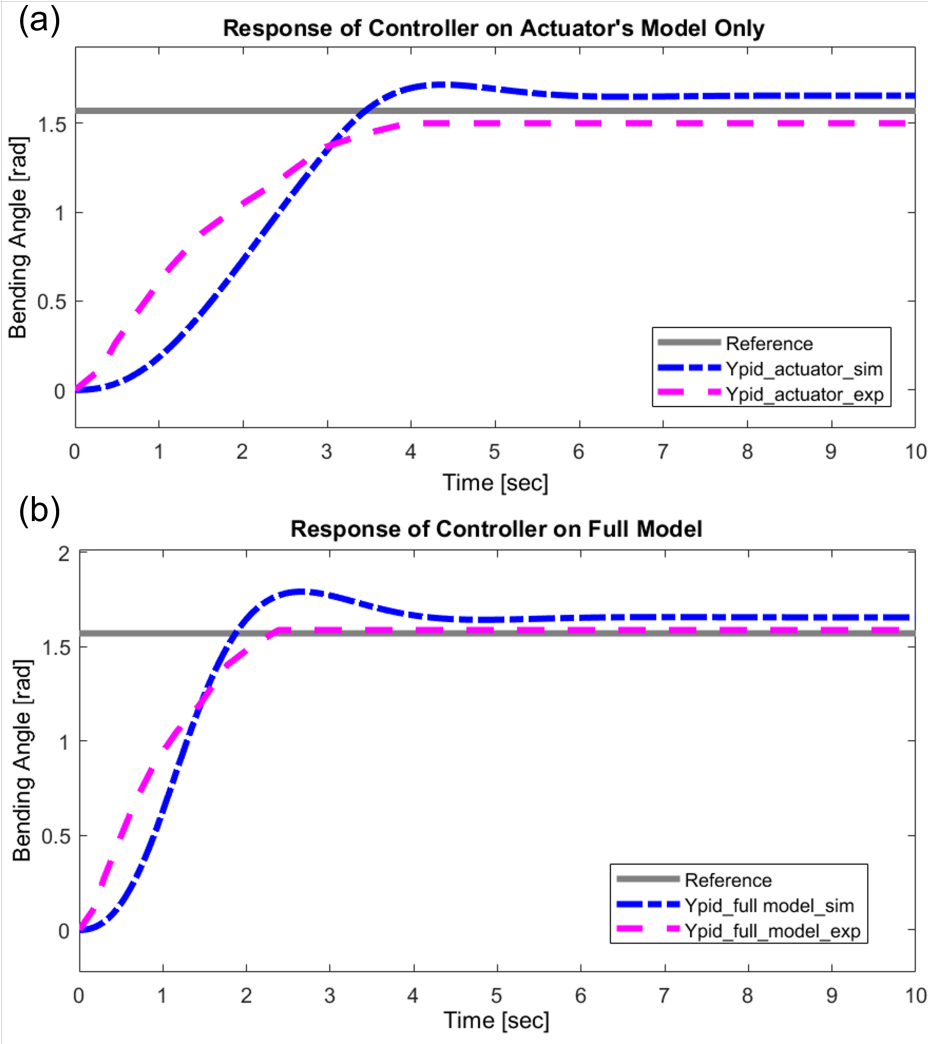
Figure 4.5: The MATLAB® simulations on two PID controllers. (a) The simulation and real responses of the controller are designed exclusively based on the actuator's model (b). The simulation and real responses of the controller are designed based on the full model.

Experimental Setup

The experimental setup is demonstrated in Figure 4.1. The syringe pump drives the soft actuator. A pressure sensor (Walfront, Lewes, DE) with a sensing range of 0 to 80 *psi* is implemented to monitor the air pressure and is synchronized with Arduino MEGA 2560 (SparkFun Electronics, Niwot, CO). The microcontroller is based on the Microchip ATmega 2560. The soft actuator has been embedded with a flex sensor [38] to get bending angle measurement, which is used to estimate the real-time volume of the soft actuator during operations. The microcontroller is also synchronized with a computer to log sensing data.

Verification of Parametric Analysis

The parametric analysis is completed in Section 4.4. There are three sets of simulations that change three parameters separately. This subsection attempts to verify the analytical results of simulations by experiments. Therefore, different syringe pumps are made corresponding to the design parameters discussed in Section 4.2, and then test their responses as shown in Figure 4.4 (b), (c), and (d). The results in Figure 4.4 (b) show that a larger cross-sectional area can increase the speed of responses. The volume change of the soft actuator also influences the accuracy and causes some errors. Then, the syringe pump with a smaller screw lead of the linear actuator is tested as in Figure 4.4 (c). The smaller screw's lead reduces the response time. Lastly, the validation of increased motor speed can be seen in Figure 4.4 (d). The error appears to be smaller at higher motor speeds. Generally, the responses are close to the model predictions in low pressures, but the errors can be up to 30 % at high pressures. Also, the volume change of the soft actuator makes the responses slower than the model predictions. However, the Kalman filter can correct the errors caused by volume change as the yellow dashed lines in Figure 4.4 (b), (c), and (d), and the errors are reduced to around five %.

Control of Soft Actuator

The importance of the pressure dynamics will be verified in this subsection since the pressure model has an influence on the responses of soft actuators. Two controllers are designed in Section 4.3 based on the actuator's model exclusively and the full model (pressure model + actuator's model). Their results are displayed in Figure 4.5 (a) and (b), and their performance is quite different. The controller designed based on only the actuator's model (4.14) has a longer settling time, around 3.95 *sec*. Its steady-state error is around 5 *deg*. By contrast, the controller designed based on the full system (4.15) has a shorter settling time, 2.38 *sec*. That is, it responds faster. The steady-state error also has been improved and is approximately 2 *deg*. Hence, considering the pressure dynamics assists in designing a better controller.

The differential motion control of the soft actuator is demonstrated in Figure 4.7. The reference function increases and decreases gradually, and the reference holds for 1.2 *sec* after

(a)

(b)
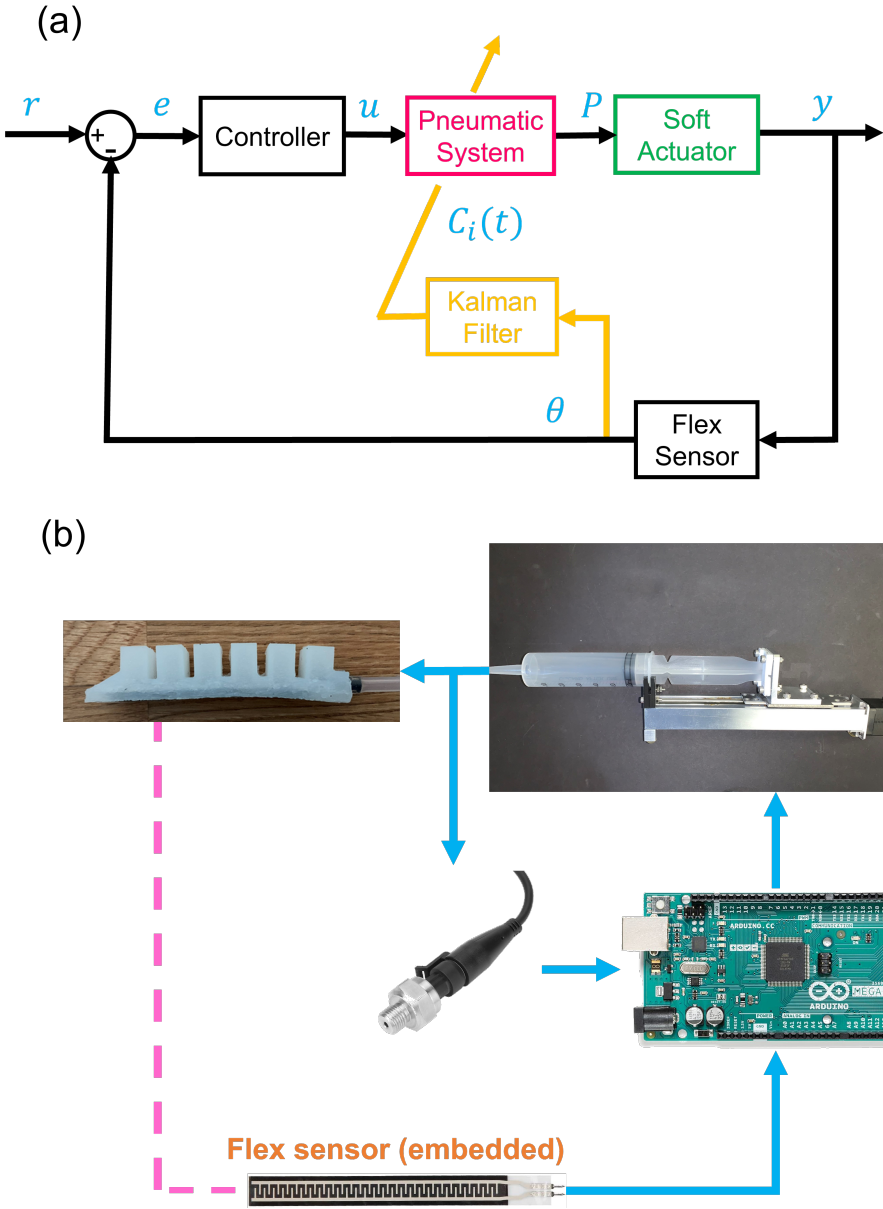
Figure 4.6: The control block diagram of the whole system.
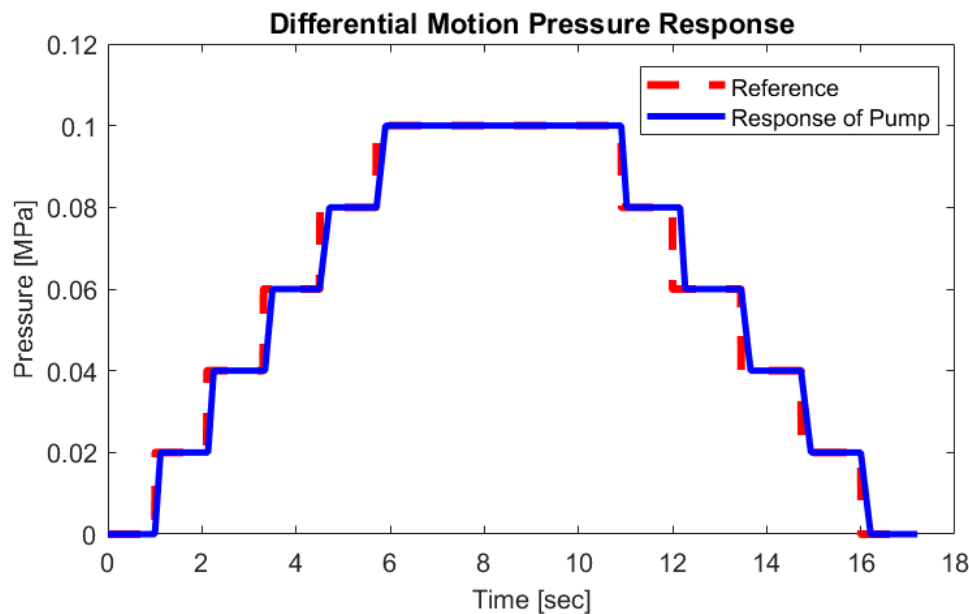
Figure 4.7: Differential motions control test of the syringe pump.

each increment or decrement. The syringe pump can track the reference, but there is a little delay during rising or falling edges. The pump takes around 0.2 *sec* to reach the desired command change. According to the performance in Figure 4.7, the syringe pump can track the reference and is suitable for differential motion control.

Discussion

Based on the results in Figure 4.3 and Figure 4.4, the optimal parameters of the syringe pump are a high cross-sectional area of the syringe, larger screw lead of linear actuator, and higher motor speed. However, the syringe pump does not use a syringe of 200 mL but a medium size (60 mL). Although the larger cross-sectional area of the syringe enables faster responses, the reverse force will act on a larger area. That causes non-smooth motions of the syringe pump, which influences the control accuracy. Also, it is expected that the syringe pump operates within a suitable pressure range ($\geq 0.15\ MPa$). A smaller volume implies a smaller operating pressure range. To summarize, a suitable cross-sectional area with a relatively longer syringe length might be an appropriate option for smooth motion control.

In addition, it is observed that a larger screw lead with a smaller cross-sectional area achieves the same pressure responses as the smaller screw lead with a larger cross-sectional area according to (4.5). The main difference between the two combinations is the volume of the syringe. The larger cross-sectional area of the syringe usually has a larger volume. The pump's operating pressure range becomes larger and it is suitable for soft actuators with a

larger volume.

4.5   Summary

This chapter presents a pressure dynamics modeling and parametric analysis methodology for a syringe pump. An air dynamic model has been built according to the configuration of the syringe pump. The time-dependent parameter in the model is estimated by the Kalman filter, which reduces the estimation errors to below five %. Then, the model is used to analyze the syringe pump to select an optimal set of design parameters. The optimal parameters enable the system to respond efficiently and smoothly and achieve differential motion control for soft actuators. The pressure model cascaded with the soft actuator's model is utilized to design a PID controller. The controller is superior to another one designed based solely on the actuator's model. The settling time has been reduced by 40 %, and steady-state error has also been decreased. This analytical modeling method provides a helpful and efficient tool for the study of a syringe pump. The syringe pump is implemented to control the soft pneumatic actuator designed in Chapter 3.

Chapter 5

Dynamical Modeling of a Soft Pneumatic Actuator

5.1 Introduction

The system's dynamical model is essential for model-based control. Both linear and nonlinear dynamical models will be studied and developed in this chapter to know the motions of the soft pneumatic actuator designed and fabricated in Chapter 3, and control algorithms will be implemented in Chapter 6.

Partial differential equations (PDEs) governed dynamics of soft robots are highly non-linear[4]. Therefore, with the complex nature of soft materials, identifying mechanical properties and representing the dynamics of soft robots are still challenging. The stress-strain curve of soft materials can be described by Hooke's Law [15, 1, 13]. The theory is valid when soft materials are under limited strains [2, 88], but the predicted errors increase in higher deformations. Several hyperelastic theories are presented to address the nonlinearity of soft materials [68, 17]. Hyperelastic theories show higher accuracy than Hooke's Law, especially in large deformations. Although parameters of hyperelastic models are provided in a recent work [68], hyperelastic theories complicate the kinematic or dynamic modeling of soft robots. In [62, 101, 11], Ludwick's Law equips the elongation term in Hooke's Law with a fractional power, making it applicable to high deformations. Ludwick's Law improves accuracy; however, to the best of the author's knowledge, there is no systematic approach for determining the fractional power of the model.

Dynamical modeling of soft robots is a common topic, including the construction of bending models for soft actuators using methods such as the piece-wise constant curvature approach [21], Cosserat rod model [25], and Lagrange equation [8]. While these methods yield accuracy, they entail complex modeling processes. Recent studies [120, 95, 109, 96] have proposed modeling soft pneumatic systems as second-order dynamic systems, determining damping ratios and natural frequencies through system identification. Second-order equations offer simplicity and accuracy at lower bending angles but become less accurate at
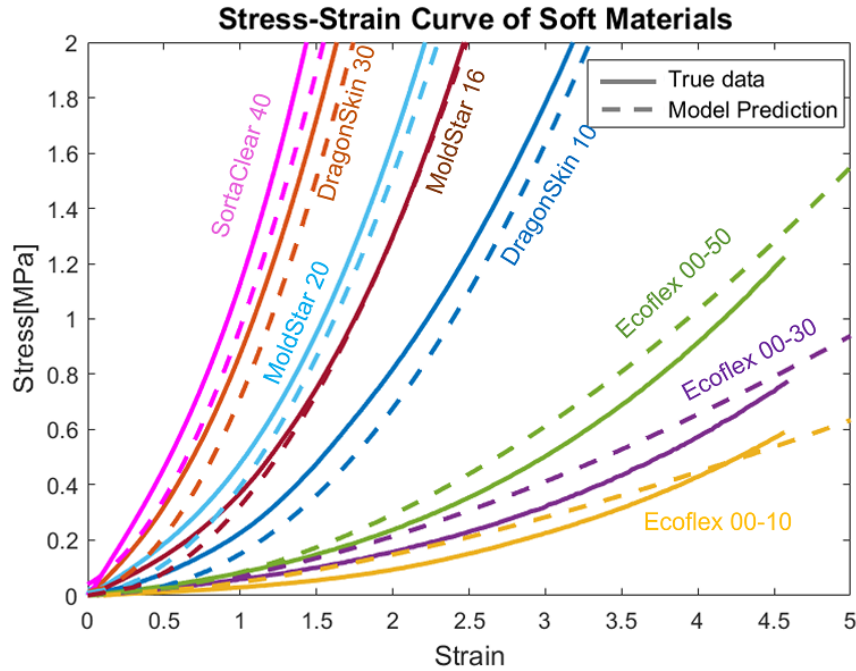
Figure 5.1: Stress-strain curve of soft materials (solid lines) [68] versus predicted stress-strain curve of Ludwick's Law (dashed lines).

higher angles. Combining Euler's bending beam theory [85] and Ludwick's Law [62] may provide a feasible, practical, and accurate dynamic model.

This project proposes a nonlinear modeling of soft pneumatic actuators and presents a data-driven method to estimate the parameters within the model. Firstly, Ludwick's Law, whose elongation term has fractional power, is introduced. The fractional power is influenced by material properties such as tensile stress, Young's modulus, and mixed viscosity. Those properties are used to build a least squares model for fractional power estimations. The theory is further implemented to construct a nonlinear dynamic model for two soft pneumatic actuators. The nonlinear model is proposed to improve accuracy for some soft materials. The responses generated by the nonlinear dynamic equation for two actuators closely match the experimental responses. Additionally, the nonlinear model is linearized to validate the limitation of the linear model and when the linear model is valid. In summary, the proposed method is an alternative modeling approach for soft pneumatic actuators.

Related works are discussed to understand the contributions of this paper in a comparative manner. Lee and Brojan [62, 11] proposed the idea of using Ludwick's Law to model large deflection components. This work extends the idea by proposing an approach to estimate the fractional power of various soft materials. Beda [7] utilized a mathematical method to estimate parameters in hyperelastic models. By contrast, this research aims to use mate-

rial properties to estimate a parameter within a nonlinear model. Porte et al. [88] studied the influences of temperature and humidity on material properties of soft materials. This work explores the influences of material properties on the nonlinearity and deformability of soft materials. Xaview [120] and Wang [109] modeled a soft robotic system as a second-order system, and the system parameters are obtained by using curve fitting. However, this research implemented a second-order nonlinear dynamic equation and the parameters are estimated by material properties. To conclude, this research aims to study the stress-strain relationship of soft materials and provide an alternative and functional modeling approach for soft robots.

The remainder of this chapter is organized as follows. Section 5.2 formulates the theories of mechanical properties of materials. Section 5.3 discusses the dynamical modeling of soft robots. Section 5.4 demonstrates the experimental results, and Section 5.5 discusses and concludes the work.

5.2 Theoretical Formulation

This section introduces Hooke's Law (linear model) and Ludwick's Law (nonlinear model). It discusses the relationship between the nonlinear model and material properties. Those properties are also utilized to build a least-square model that can estimate the fractional power within Ludwick's Law.

Stress-Strain Relationship

Generally, the stress-strain curve of materials is described by Hooke's Law [13].

$$\sigma = E\epsilon \tag{5.1}$$

where $\sigma = P/A$ is the stress and is defined as the applied force P divided by the cross-sectional area A, E is the Young's modulus, and $\epsilon = \frac{L-L_0}{L_0}$ is the strain and is defined as elongated length L minus initial length L_0 divided by initial length.

Equation (5.1) depicts the linear relationship between stress and strain. This equation is valid under small elongations or when it is applied to hard materials such as metals [13]. However, soft materials usually exhibit large elongations because of relatively small Young's modulus. The stress-strain curve of common soft materials is highly nonlinear [68]. The linear stress-strain curve is no longer valid since the curve is nonlinear [119]. As the materials are under large deformations, Ludwick's relation should be applied [62, 41, 11]

$$\sigma = E\epsilon^n \tag{5.2}$$

where $n \in \mathbb{R}$ is a fractional number and it varies with materials.

Based on (5.2), the stress-strain curve is nonlinear, and the power n is dependent on the properties of materials. The next issue will be proposing a systematic way to determine the

fractional power n. In contrast to the limited options available for integer values, finding an appropriate n as a fractional number often requires trial-and-error-based approaches. Optimization approaches may help, but a suitable problem formulation is needed [9].

Fractional Power and Material Properties

The n in (5.2) is usually obtained empirically or experimentally. Thus, this subsection aims to explore the relationship between material properties and the fractional power n of (5.2). With the relationship between n and material properties, the fractional power can be determined, and (5.2) has the potential to be applied in future research.

When it comes to material properties, there are a large number of choices, such as density, heat capacity, hardness, coefficient of thermal expansion, etc. However, key material properties could be selected according to (5.2). Tensile strength, Young's modulus, and mixed viscosity are chosen to study their relationship with the fractional power n. Tensile strength represents the maximum external force, σ in (5.2), that a material is capable of resisting. Young's modulus (E) characterizes its stiffness and ability to withstand stretching. Mixed viscosity quantifies the material's resistance to flow when soft materials are in a liquid state. The commonly used soft materials turn into a solid state by mixing liquid rubber with curing agents [119]. The effect of viscosity, thus, might influence the elongation term (ϵ) [107]. In Figure 5.3, each property shows a correlation with the fractional number n.

This research studies 10 commonly used soft materials, namely Smooth-on Dragon Skin FX-Pro, Dragon Skin™10 MEDIUM, Dragon Skin 20, Dragon Skin 30, Ecoflex™00-10, Ecoflex 00-30, Ecoflex 00-50, Mold Star™16 FAST, Mold Star 20T, and SORTA-Clear™40. Their properties are also provided on the supplier's website [98]. Their stress-strain curves are provided in the online library [68]. The true fractional power of each soft material is obtained by applying curve fitting the stress-strain curve in the library. The properties and fractional numbers of the materials are displayed in Table 5.1.

Fractional Power Estimation

Three properties, tensile stress, mixed viscosity, and Young's modulus, encapsulate the complex behavior of a material under stress, as illustrated in Figure 5.3. To utilize these findings effectively, the technique of least squares regression is employed to build a prediction model. Those selected properties serve as predictors, and the fractional power acts as a response. By doing so, the model mathematically captures the relationships between these properties and the fractional power, enabling them to make accurate forecasts about a material's performance under various stresses, which is invaluable in the field of soft robotics. Thus, a least-squared model can be utilized to predict the stress-strain curve (fractional number) when the properties of a soft material are given.

The standard least-square model [9] is described as

Table 5.1: Fractional power and material properties of selected soft materials [98]

Material name	Fractional power (n)	Young's modulus (MPa)	Mixed viscosity (Pa· s)	Tensile strength (MPa)
Dragon Skin FX Pro	1.538	0.26	18	1.99
Dragon Skin™ 10 MEDIUM	2.174	0.15	23	3.28
Dragon Skin 20	2.500	0.34	20	3.79
Dragon Skin 30	2.222	0.59	20	3.45
Ecoflex™ 00-10	1.538	0.06	14	0.83
Ecoflex 00-30	1.613	0.07	3	1.38
Ecoflex 00-50	1.818	0.08	8	2.17
Mold Star™ 16 FAST	2.000	0.38	12.5	2.76
Mold Star 20T	2.174	0.32	11	2.90
SORTA-Clear™ 40	2.500	0.62	35	5.51

$$y = Ax \tag{5.3}$$

where $A \in \mathbb{R}^{m \times n}$ is a matrix that contains the predictors of each experiment, $y \in \mathbb{R}^m$ is a column vector that includes the measured responses, and $x \in \mathbb{R}^n$ is a column vector whose parameters are to be solved. The m represents the data number, while n is the number of predictors.

The closed form solution of (5.3) is obtained by pre-multiplying A^T on both side and then pre-multiplying inverse of $A^T A$

$$A^T A x = A^T y$$
$$x = (A^T A)^{-1} A^T y \tag{5.4}$$

where $(A^T A)^{-1}$ is nonsingular, invertible, and exists.
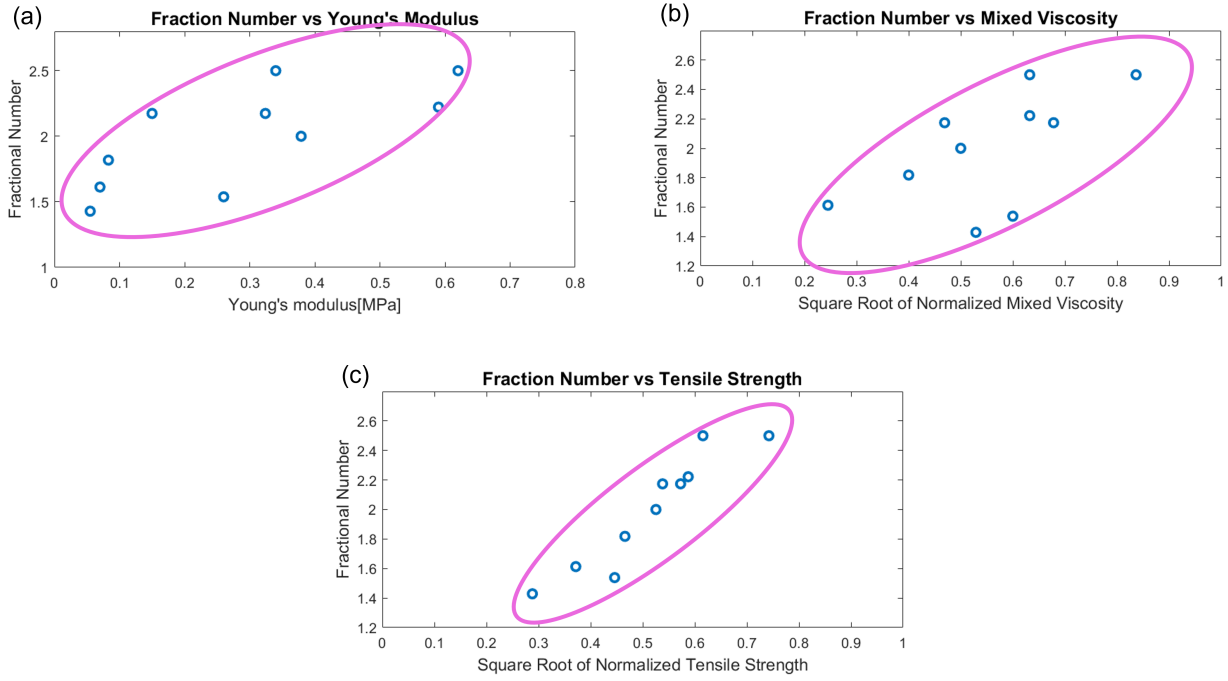
Figure 5.2: Selected material properties correlate to the fractional power n.

Based on (5.4), the y vector contains the fractional power of each selected material in Table 5.1 of Section 5.2

$$y = \begin{bmatrix} n_1 & n_2 & \dots & n_m \end{bmatrix}^T \qquad (5.5)$$

and the x vector contains the parameters to be solved and it is depicted as

$$x = \begin{bmatrix} x_1 & x_2 & x_3 \end{bmatrix}^T \qquad (5.6)$$

and the A matrix includes the material properties in Table 5.1 of Section 5.2

$$A = \begin{bmatrix} E_1 & MV_1^{0.5} & TS_1^{0.5} \\ E_2 & MV_2^{0.5} & TS_2^{0.5} \\ & \vdots & \\ E_m & MV_m^{0.5} & TS_m^{0.5} \end{bmatrix} \qquad (5.7)$$
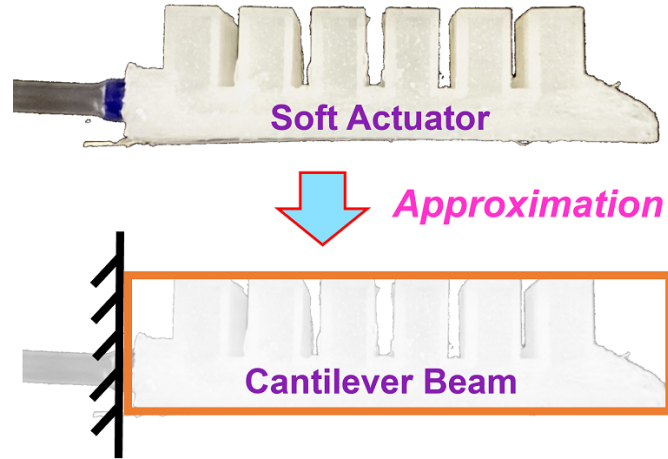
Figure 5.3: The irregular geometric structure of the soft pneumatic actuator is approximated by a cantilever beam.

where MV is the abbreviation of the mixed viscosity, which is normalized by 50 $Pa \cdot s$, and TS is the abbreviation of the tensile strength, which is normalized by 10 MPa. Since 10 soft materials are selected in Section 5.2, they are divided into 8 and 2. The 8 soft materials are used to build the least squares model. Thus, the m is 8 here and the other 2 materials (Smooth-on Dragon Skin FX-Pro and Smooth-on Dragon Skin 20) will be used to verify the least squares model.

With (5.5)-(5.7), the values of x vector is obtained by using (5.4), and least-square model is represented as

$$y = Ex_1 + MS^{0.5}x_2 + TS^{0.5}x_3 \tag{5.8}$$

This model will be used to predict the fractional number (n) given new or unknown soft materials. When the properties of Young's modulus, mixed viscosity (if applicable), and tensile stress are found, the (5.8) is applied to predict n of the soft material. The results will be displayed in Section 5.4.

5.3 System Modeling

Obtaining the parameter within Ludwick Law(5.2) is used to build the dynamic model of soft robotic systems. Here, this section will focus on modeling soft pneumatic actuators (SPAs) as discussed in previous work [128]. The MATLAB®️ simulation results are also demonstrated in this section.

SPAs have irregular geometric shapes since they consist of several discrete chambers as Figure 5.3. The nonlinear structure is approximated as a cantilever beam. The simplified structure makes the dynamic analysis possible. The analytical methods for a cantilever beam can be applied [128]. Instead of using Hooke's Law (5.1), Ludwick's Law (5.2) is applied, and the analytical method for a cantilever beam.

The approximated beam structure is shown in Figure 5.4. When a force is applied to the free end of the beam, the structure will bend, resulting in a bending angle. The bending angle can be depicted as [13]

$$P = (\frac{2EI}{L_0^2})\theta = K\theta \tag{5.9}$$

$$K = \frac{2EI}{L_0^2} \tag{5.10}$$

where F is the force acted at the free end and the force here is generated by the pressure, L_0 is the initial length of the structure, K is the spring constant, θ is the bending angle, and I is the moment of inertia which depicted as

$$I = (\frac{1}{12})bh^3 \tag{5.11}$$

where b is the width of the cross-sectional area of the beam, and h is the height of the cross-sectional area of the beam.

Equation (5.9), however, is derived based on linear model assumption [13]. It may not describe the dynamics of nonlinear soft materials. To apply the nonlinear model as (5.2), the model is adjusted according to [62]. When the pressure is applied to the soft actuator, it will bend as shown in Figure 5.5. The bending angle can be described as

$$P = (\frac{n+1}{n})^n(\frac{EI_n}{L_0^{n+1}})\theta^n = K_n\theta^n \tag{5.12}$$

$$K_n = (\frac{n+1}{n})^n(\frac{EI_n}{L_0^{n+1}}) \tag{5.13}$$

where K_n is the spring constant when $n > 1$, I_n is the modified moment of inertia for a large deflection component, and it is displayed as

$$I_n = (\frac{1}{2})^n(\frac{1}{2+n})bh^{(2+n)} \tag{5.14}$$

If $n = 1$, the (5.12)–(5.13) degrade to (5.9)–(5.11) and the model becomes linear.

With (5.12), the bending dynamic equation of the soft pneumatic actuator is built by
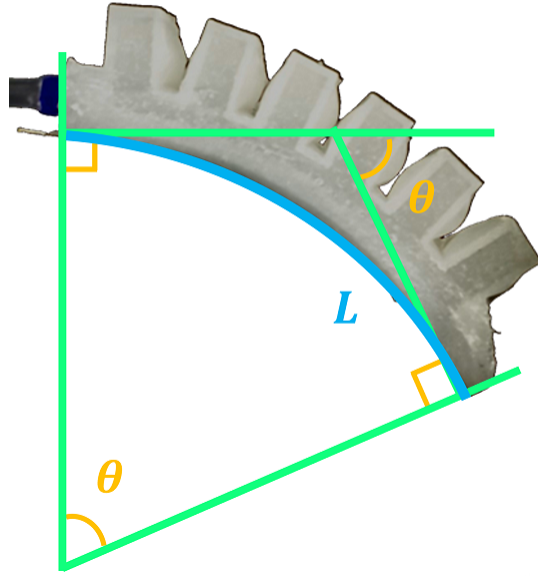
Figure 5.4: The bending geometric of the soft actuator when it is pressurized.

$$F - C_n\dot{\theta} - K_n\theta^{n+\Delta n} = M_{eq}\ddot{\theta} \tag{5.15}$$

where Δn represents the perturbation of soft materials. After manipulation, the nonlinear dynamic model of the soft actuator is shown as

$$M_{eq}\ddot{\theta} + C_n\dot{\theta} + K_n\theta^{n+\Delta n} = F \tag{5.16}$$

where M_{eq} is the equivalent mass of the soft actuator, C_n is the damper of the soft actuator, K_n is the spring constant obtained from (5.13). The M_{eq} and C_n currently are estimated by applying system identification through MATLAB®, which has an average fitting accuracy of approximately 95.3%.

The dynamic equation is similar to the second-order equation, but it has a nonlinear spring term based on Ludwick's Law (5.2). The fractional power (n) can be estimated by using (5.8) and the selected material properties.

Although the nonlinear model method is proposed for the soft pneumatic actuator, the linear model is also studied to understand its limitations. The nonlinear model is more accurate, while the linear one is in a simple form. The researchers, therefore, could evaluate whether to apply linear or nonlinear models for the soft robotic systems. If $n = 1$, the (5.16) becomes

$$M_{eq}\ddot{\theta} + C_n\dot{\theta} + K_n\theta = F \qquad (5.17)$$

The validation results of the linear model (5.17) and the limitation of the linear model can be observed in Section 5.4 and are compared with the results of the nonlinear one.

5.4 Experimental Evaluation

Soft Actuators Setup

In Section 5.2, eight materials are used to build a least squares model and the other two will be used to verify. Thus, two soft actuator prototypes are made of Smooth-on Ecoflex® Dragon Skin FX-Pro and Smooth-on Ecoflex® Dragon Skin 20 respectively. Two actuators have upper and bottom components which are fabricated by using two different molds [128, 127]. They are then bonded together by the silicone adhesive, Smooth-on Sil-poxy®. The nozzle at their end is connected to the syringe pump [126] to provide air pressure. The bottom component has a piece of flex sensor embedded inside [38]. Two soft actuators have the same dimensions.

The estimated fractional powers of Dragon Skin 20 and Dragon Skin-FX Pro are 2.365 and 1.727, respectively, as shown in Table 5.2. The estimated fractional powers are close to the true values but have limited errors. With the fractional powers, the dynamic equation of soft actuators is established.

Table 5.2: Comparison of estimated and true fractional powers

Material Name	True Value	Estimated Value
Dragon Skin 20	2.174	2.365
Dragon Skin FX-Pro	1.538	1.727

Experimental Setup

Figure 5.7 presents the control block diagram and the experimental setup. Soft actuators are powered by a custom-designed syringe pump introduced in Chapter 4 [126]. To facilitate open-loop control, an air pressure sensor (Walfront in Lewes, DE) is employed, offering a sensing range of 0 to 80 *psi* to monitor air pressure. Within the actuator, a flex sensor (Walfront in Lewes, DE) is integrated to measure the bending angle, enabling feedback control. Both sensors are synchronized with the Arduino MEGA 2560 microcontroller (SparkFun Electronics, Niwot, CO). This microcontroller is based on the Microchip ATmega 2560 platform. Furthermore, the microcontroller is connected to a computer to record the sensing data.
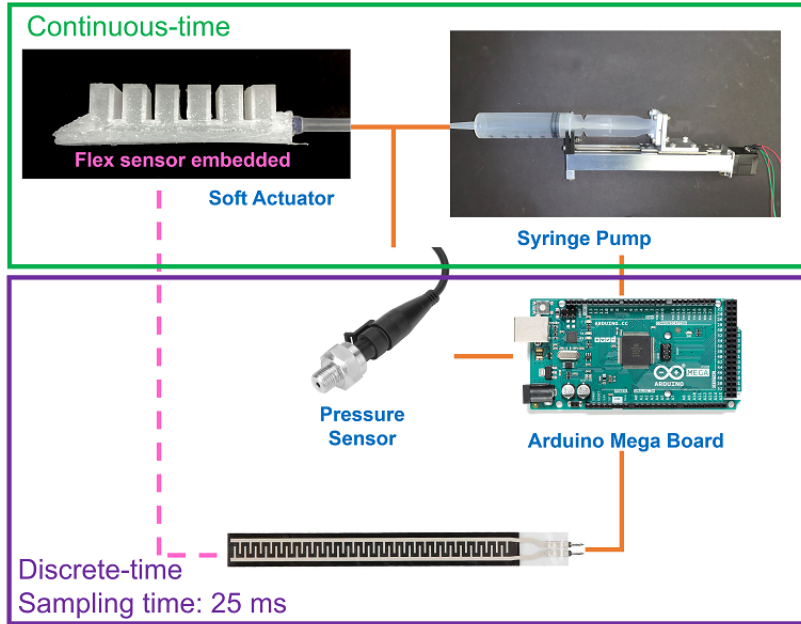
Figure 5.5: The schematic of the experimental setup.

Step Response Test

Step response tests intend to evaluate the proposed nonlinear model. Equation (5.16) is solved by MATLAB® solver "ode45" to get the system responses. The schematic of the bending angle of soft actuators is shown in Figure 5.4. The bending angles are measured by the flex sensor embedded inside the soft actuators. In addition, there are two soft actuators made of Dragon Skin 20 and Dragon Skin FX-Pro. The former one is named "Design 1", while the latter is called "Design 2".

Design 1 Test

The step response tests are visualized in Figure 5.6. In Figure 5.6 (a), the setpoint is 60 *deg*. Seven true responses are done and added to the figure to evaluate the model's accuracy. Additionally, a linear second-order dynamic equation was proposed to model soft actuators in the previous work [130]. The linear equation is plotted in the same figure. In Figure 5.6 (a), the nonlinear dynamic equation describes the system's responses better than the linear equation. The root-mean-square error (RMS) of the nonlinear equation and the average of true responses is 1.29 *deg* (2.2%), while the RMS of the linear equation and the average of true responses is 2.03 *deg* (3.4%).

Another step response test is conducted with a different reference (90 *deg*). This test tends to evaluate the model's accuracy with a higher bending angle. The results are demonstrated
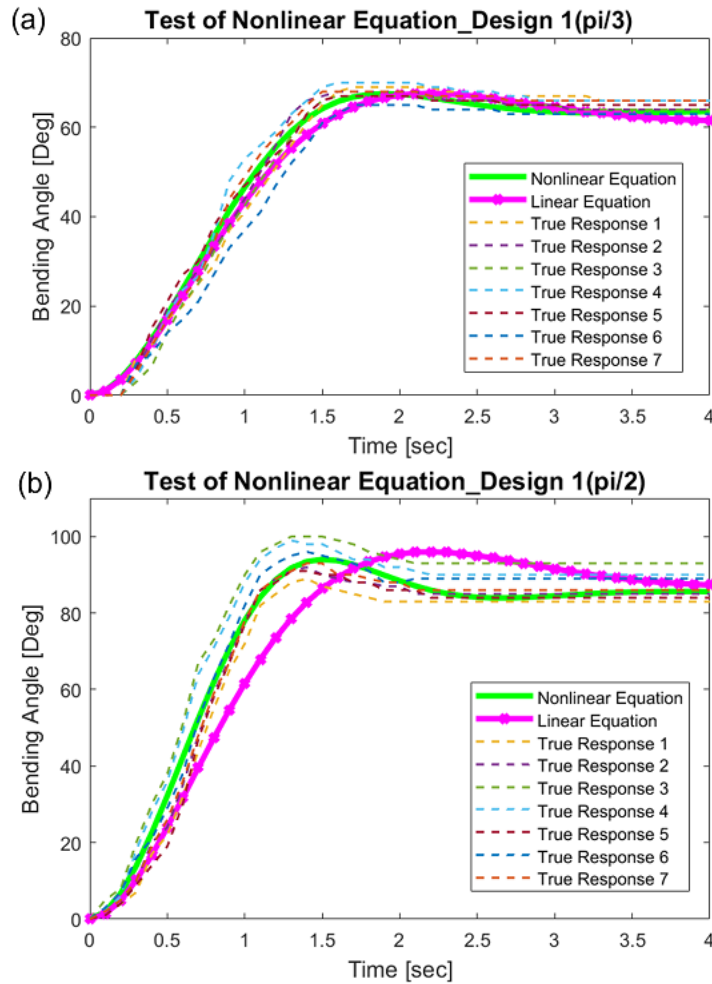
Figure 5.6: Comparisons between seven experimental data, linear dynamical equation and nonlinear dynamical equation of the soft actuator made of Smooth-on Dragon Skin 20.

in Figure 5.6 (b). The RMS error between the nonlinear model and the average of true responses is 3.17 *deg* (3.5%), while the RMS error of the linear equation with true response is 6.15 *deg* (6.9%). The nonlinear dynamic equation has smaller errors; thus, it is more accurate than the linear dynamic equation.

Design 2 Test

The step response tests are visualized in Figure 5.7. The reference is 60 *deg* in the first test (Figure 5.7(a)). The RMS error of the nonlinear equation and average of true responses is 1.46 *deg* (2.4%) and that of the linear equation and average of true responses is 3.49 *deg* (5.8%). The reference is 90 *deg* in the second test (Figure 5.7(b)). The RMS errors
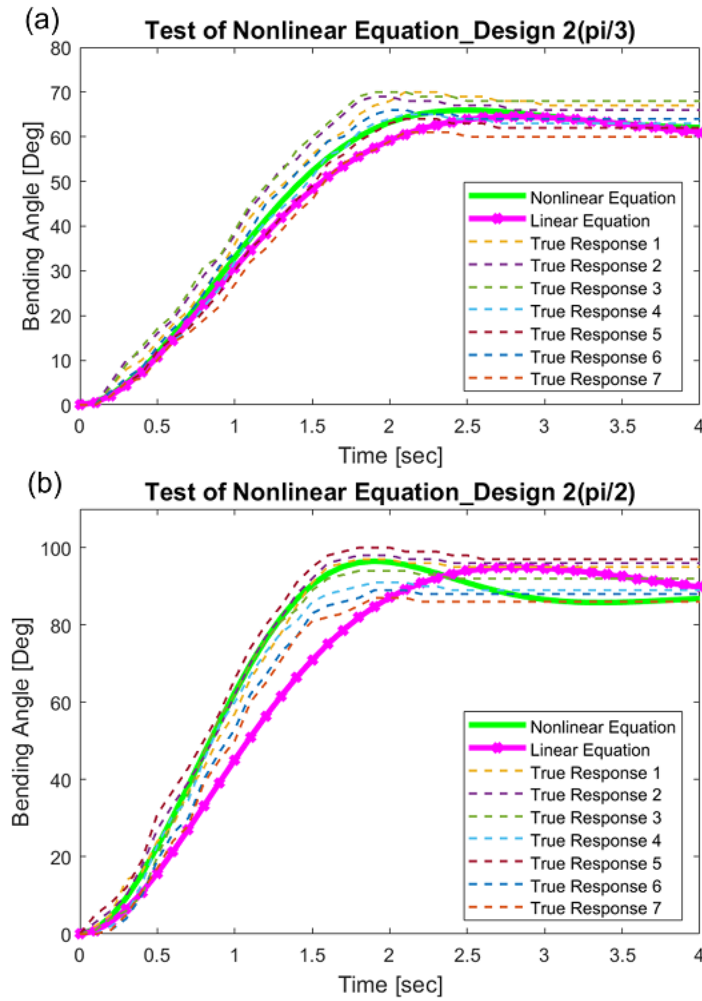
Figure 5.7: Comparisons between seven experimental data, linear dynamical equation and nonlinear dynamical equation of the soft actuator made of Smooth-on Dragon Skin FX-Pro.

between both equations and the average of true responses are 3.61 (4.0%) and 7.98 *deg* (8.9%) respectively. Again, the nonlinear dynamic equation outperforms.

The use of nonlinear models improves the accuracy when modeling soft actuators. However, as in Figure 5.6 and 5.7, limited errors still exist since soft materials exhibit uncertainty [88]. The uncertainty of soft materials contributes to the RMS errors, which range around 2-3 *deg* observed from the experimental results.

5.5   Discussion and Summary

Discussions

The results presented in Section 5.4 demonstrate the validity of the linear second-order equation under conditions of limited bending angles. When the bending angle remains within a limited range (60 deg), the elongation of the soft material remains relatively modest. This observation is corroborated by the stress-strain curve, where it is evident that Hooke's Law (5.1) closely approximates the experimental data. However, as the bending angle increases, so does the extent of elongation in the material. In such cases, the linear equation may no longer suffice, and it becomes necessary to consider the application of Ludwick's Law (5.2). This project mainly studies the commonly used soft materials, but this approach could be extended to other soft materials. This method saves time and effort, particularly since tensile tests are not needed to obtain unknown parameters. As the field of soft robotics continues to grow, new materials will likely be invented. The proposed approach will help model the dynamics of new soft materials.

Another benefit of using (5.2) lies in the fractional power (n) of the nonlinear equation. Since soft materials have uncertainty and their behaviors vary with environmental conditions [38], equation (5.16) could be modified as $M_{eq}\ddot{\theta} + C_n\dot{\theta} + K_n\theta^{n+\Delta n} = F$. The Δn represents the uncertainty of soft materials. The small perturbation term is added to finely adjust the dynamic model of soft robots. By contrast, if Δn is an integer number ($\Delta n \in \mathbb{N}$), it is hard to adjust the stress-strain curve. That is, the $n + \Delta n$ will be an integer such as 1, 2, 3, etc. The stress-strain curve changes obviously as the perturbation term is added, so the curve cannot catch true experimental data precisely. To sum up, the fractional power can be any real value and the perturbation term (Δn) is smaller than unity. Therefore, a nonlinear dynamic equation has more degree of freedom than an integer-order equation.

Conclusion

This chapter introduces a novel nonlinear modeling approach for soft pneumatic actuators and proposes an effective method for estimating the parameters within the nonlinear model. The approach involves describing the stress-strain curve of soft materials using Ludwick's Law, which accurately captures the true stress-strain data. Instead of relying on conventional curve fitting methods, the least squares method is employed to estimate the parameters within this nonlinear model. To facilitate parameter estimation, essential material properties such as tensile stress, Young's modulus, and viscosity are chosen as predictors in the least squares model. This approach yields predicted parameters that closely align with the true values, with an error margin of less than 10%. Furthermore, the application of Ludwick's Law is extended to formulate the dynamic equations for two soft actuator prototypes, each constructed from different soft materials. Experimental step response tests validate the accuracy and reliability of our nonlinear model. Specifically, it is observed that the RMS errors of the nonlinear dynamic equations remain within 3 deg even at higher bending angles.

In contrast, the linear dynamic equation exhibits larger RMS errors of up to 9 *deg*. In conclusion, this innovative modeling methodology and parameter estimation approach offer an alternative for modeling soft materials. The dynamical model will be utilized to design controllers for soft pneumatic actuator control in Chapter 6.

Chapter 6

Underactuated Control of Multiple Soft Fingers within A Soft Gripper

6.1 Introduction

Soft pneumatic actuator is optimally designed in Chapter 3, the air pump is designed in Chapter 4, and the dynamical model is built in Chapter 5. The soft actuator will be served as fingers within a soft gripper, pneumatically actuated by the air pump. The inherent compliance and adaptability of soft gripper show advantages for applications requiring delicate manipulation [77, 37] and interaction with complex or unknown environments [51, 129]. Compared to rigid-bodied robotic hands, soft grippers stand out for their ability to conform to a wide range of object shapes and sizes, making them indispensable in domains such as medical robots [1] and human-robot interactions [22]. However, achieving precise control over the motion and coordination of multiple soft fingers within a gripper remains a challenge [130]. The soft fingers in this project are pneumatic driven and air is supplied by air pumps. If the number of fingers exceeds the number of pumps, the system is under-actuated. Since the air pump is bulky, it is desired to minimize the number of air pumps [46, 106, 137].

Despite the recent development of soft robot control, achieving precise control under the underactuated control framework for soft robots is seldom discussed and remains a challenge. A couple of works addressed the soft robot control issues by applying nonlinear controllers [96, 97], adaptive controllers [95, 99], and optimal controllers [130, 8]. Those control strategies enable high-performance control of soft robots with high degrees of freedom. However, the control of these systems becomes increasingly complex as the number of degrees of outputs exceeds that of inputs (underactuated systems) [46]. Another factor contributing to this complexity is the dynamic uncertainty observed in soft robots [16]. To better understand the nature of uncertainty in soft robotics, several key factors have been identified through various studies: (1) epistemic uncertainties arising from limited or insufficient data and the inherent complexity of physical models [57]; (2) unknown environmental factors that influence the system's parameters; (3) unmeasurable physical properties of materials, such
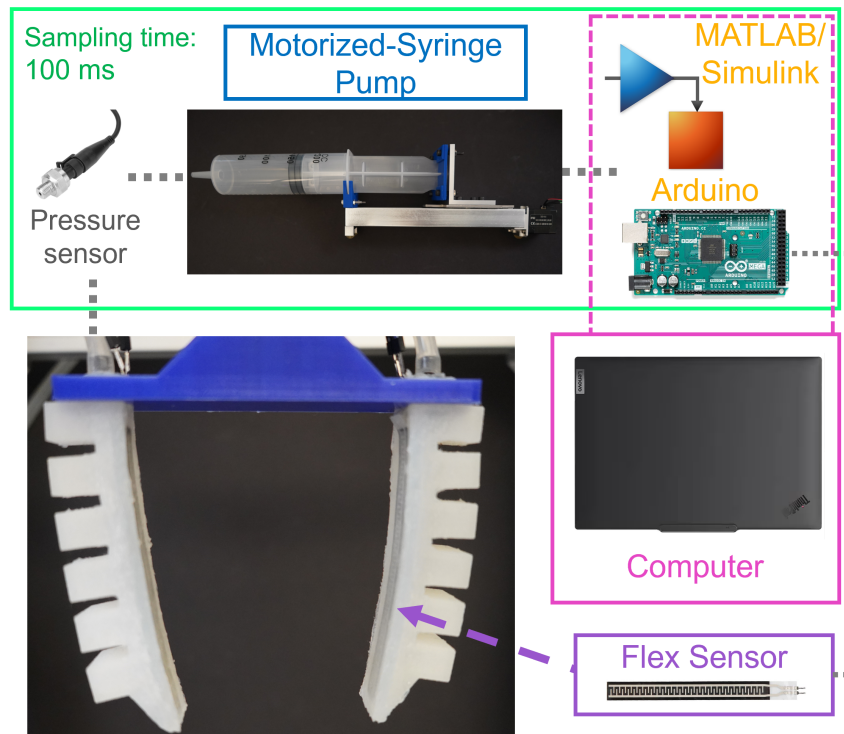
Figure 6.1: The soft gripper has two fingers and is driven by a single syringe pump to achieve underactuated control via stable inversion. The control commands are generated in MATLAB®/Simulink and are converted to PWM for the stepper motor in the syringe pump. The bending angles of both fingers are measured by the flex sensor embedded in each soft gripper.

as the tendency of polymer-based actuators and sensors to age or the time required to reach chemical stability [54]; (4) the parameter-varying nature of the material's internal bonding structure [35]; and (5) manufacturing tolerances. These factors contribute significantly to the challenges in developing accurate models for soft robotic systems. Consequently, the robustness of the controller becomes increasingly critical. Addressing this challenge may necessitate the development of novel control strategies capable of effectively coordinating multiple soft actuators within a soft gripper, enabling precise and adaptive manipulation tasks.

   One objective of this project is to develop control algorithms for achieving coordination in multi-finger soft grippers. Such systems are modeled as single-input-multi-output (SIMO) systems. This approach integrates both feedforward and feedback control loops. The feedforward control mechanism incorporates a stable model inversion technique that effectively controls the motions of multiple soft fingers. Given the inherent uncertainty of soft materi-

als, the feedback loop is adept at mitigating unexpected errors, noise, or disturbances that may arise between the mathematical model and the real system. Comprehensive validation of the control algorithms is conducted through simulations and experimentation. The theoretical framework underpinning these control algorithms is initially introduced in [59], where its efficacy is established by necessary and sufficient conditions. The contributions of this research lie in the innovative application of stable inversion algorithms to address uncertain soft robotic systems. Notably, the proposed controller achieves coordination of multi-finger soft grippers with a single input, thereby demonstrating the applicability of these control algorithms to SIMO control problems.

Another contribution of this work is the investigation of parametric variations in uncertainties associated with soft pneumatic actuators (SPAs). The experiments demonstrate that the multiplicative uncertainty envelope changes with the operational speed of the SPAs, indicating that the level of uncertainty varies as their speed varies. Furthermore, both theoretical and experimental investigations are conducted to explore how this uncertainty envelope correlates with the bandwidth of the closed-loop control system. This analysis provides insights into how adjustments in system parameters can impact the uncertainty bounds, potentially improving the performance and robustness of control strategies for SPAs.

To position the contributions, this research is compared with recent works. In the prior study [130], individual syringe pumps for each finger were employed within a multi-finger soft gripper (full-drive) to attain precise and synchronized motions, so the number of air pumps is equal to the number of fingers. In contrast, the present research adopts stable model inversion alongside a single air pump to achieve coordination across all fingers within the multi-finger soft gripper. The algebraic-related method was proposed in [56], which established input coordination transformation that made the underactuated soft robotic systems become quasi-fully actuated systems. Although the feedforward control uses a similar concept, there is a feedback loop to cope with the uncertainty of the soft robotic systems that ensures robustness of the system. Pustina et al. [90] studied the controllability and stability of the underactuated soft robots. But this work focuses on the SIMO problem of coordinating motions of multiple soft robots with a single input. Overall, this research studies the stable underactuation of soft robots with robust performance.

The remainder of this chapter is organized as follows. Section 6.2 introduces the mathematics preliminary and problem statement. Section 6.3 describes the full mechatronic design and algebraic controller design. Section 6.4 evaluates the feasibility and applicability of the controller by simulations and experimentation. Section 6.5 discusses the experimental results and concludes the work.

6.2 Problem Formulation

Mathematics Preliminaries

The set $\mathbb{R}$ is a real number field. Then, the set of all these rational functions in s over $\mathbb{R}$ forms a field, denoted by $\mathbb{R}(s)$ [33]. The sets of $n_y \times n_u$ matrices with elements in $\mathbb{R}$ and $\mathbb{R}(s)$ are denoted by $\mathbb{R}^{n_y \times n_u}$ and $\mathbb{R}(s)^{n_y \times n_u}$ respectively.

The rank of a matrix P over the field $\mathbb{R}(s)$ is defined as the maximum number of linearly independent subsets of its columns (or rows) [3]. This is denoted by $\operatorname{rank}_{\mathbb{R}(s)}(P)$. A set of vectors $v_1, v_2, ..., v_{n_u}$ is linearly independent in the field $\mathbb{R}(s)$ if and only if the condition $\sum a_i v_i = 0$ and $a_i = 0$ for every i with the scalars a_i in $\mathbb{R}(s)$.

Suppose the rank of $P(s) \in \mathbb{R}(s)^{n_y \times n_u}$ is r where $1 \leq r \leq \min(n_u, n_y)$. By choosing $P(s)$'s r linearly independent columns, a set of vectors is defined

$$\mathcal{L}(P) = \{p_i \mid 1 \leq i \leq r\} \tag{6.1}$$

with p_i being linearly independent over $\mathbb{R}(s)$. Now, the *Image (Range) Set* for the real-rational matrices in s is defined as follows.

$$\operatorname{Im}_{\mathbb{R}(s)}(P) = \left\{\sum_{i=1}^{r} c_i p_i : c_i \in \mathbb{R}(s), p_i \in \mathcal{L}(P)\right\} \subseteq \mathbb{R}(s)^{n_y \times 1} \tag{6.2}$$

Theorem 1. *(Rouche-Capelli Theorem) Consider $P \in \mathbb{R}(s)^{n_y \times n_u}$ with $\operatorname{rank}_{\mathbb{R}(s)}(P) = r$ and $Y \in \mathbb{R}(s)^{n_y \times 1}$. The solution(s) U for the equation $PU = Y$ is exist if and only if*

$$\operatorname{rank}_{\mathbb{R}(s)}(P) = \operatorname{rank}_{\mathbb{R}(s)} \underbrace{([P(s) : Y(s)])}_{\in \mathbb{R}(s)^{n_y \times (n_u+1)}} = r \tag{6.3}$$

Some notations used in the paper are: the $\Re(\cdot)$ represents the real part of the given complex number, and $\Im(\cdot)$ denotes the imaginary part of the number. $\mathcal{L}_\infty(j\mathbb{R})$ represents functions bounded on $\Re(s) = 0$ including at ∞, and $\mathcal{RH}_\infty$ is the Hardy Space and denotes the set of $\mathcal{L}_\infty(j\mathbb{R})$ functions analytic in $\Re(s) > 0$.

Problem Statement

The soft gripper, equipped with multiple fingers that can provide a human-like grasping experience, serves as the plant for the proposed control algorithms. Soft robotic systems, by their nature, exhibit nonlinear behaviors due to the compliance and deformability of their materials [16]. However, the nonlinearity of certain soft materials may not be evident under reasonably constrained deformations. Therefore, within the constraints of deformations, it

is feasible to approximate the behavior of soft robots using linear uncertainty models [130, 136].

The multi-fingered soft gripper can be considered a type of multi-input-multi-output (MIMO) linear time-invariant (LTI) system where the state-space realization follows as

$$
\begin{aligned}
\dot{x} &= Ax + Bu \\
y &= Cx, x(0) = 0
\end{aligned}
\tag{6.4}
$$

where $A \in \mathbb{R}^{n \times n}$, $B \in \mathbb{R}^{n \times n_u}$, $C \in \mathbb{R}^{n_y \times n}$, $x(t) \in \mathbb{R}^{n \times 1}$, $y(t) \in \mathbb{R}^{n_y \times 1}$, and $u(t) \in \mathbb{R}^{n_u \times 1}$.

Equivalently, by using the Laplace transformation, (6.4) can be expressed with Transfer Function Matrices (TFM) as follows

$$
\begin{aligned}
Y(s) &= C(s)(sI - A)^{-1}BU(s) \\
&\Rightarrow Y(s) = P(s)U(s)
\end{aligned}
\tag{6.5}
$$

Assumption 2. *The system given in (6.5) is assumed to have the following properties:*

a. *The system (6.5) is minimal, implying controllability and observability.*

b. *The system (6.5) is the minimum phase and Hurwitz, meaning all poles and transmission zeros are in the left half of the complex plane.*

c. *$Y(s) \in \mathrm{Im}_{\mathbb{R}(s)}(P)$, indicating that any output function is in the range space of P, making the output function achievable.*

These assumptions ensure that the system is well-posed and stable, facilitating the design and analysis of the control strategies. These assumptions will be validated through analysis and assess their applicability under real-world conditions in Section 6.4.

To achieve a less complicated design, enhanced energy efficiency, and reduced weight, a single input source is used to control all fingers with different dynamics and outputs. With this approach (having one input), the system described in (6.5) becomes a SIMO system

$$
\begin{bmatrix} Y_1(s) \\ \vdots \\ Y_{n_y}(s) \end{bmatrix} = \begin{bmatrix} P_1(s) \\ \vdots \\ P_{n_y}(s) \end{bmatrix} U(s)
\tag{6.6}
$$

where $P_i(s) \in \mathbb{R}(s)$, $Y_i(s) \in \mathbb{R}(s)$, $i = 1...n_y$, and $U(s) \in \mathbb{R}(s)$. Solving the algebraic equality for $U(s)$ gives the *exact left inverse*. Since $P(s)$ (where $P(s) \neq 0$) consists of a single-column real rational vector, the $\mathrm{rank}_{\mathbb{R}(s)}(P)$ is always equal to 1. Together with *Assumption 2. c.*, the condition for the existence stated in *Theorem 1* as

$$\text{rank}_{\mathbb{R}(s)}(P) = \text{rank}_{\mathbb{R}(s)}([P(s) \ : \ Y(s)]) = 1 \tag{6.7}$$

is met, which ensures that (6.5) has a unique solution. On the other hand, since $P(s)$ has
no unstable invariant zeros (*Assumption 2. b.*), the unique solution is also stable, i.e., U(s)
$\in \mathcal{RH}_\infty$.

6.3   Methodology

In this section, the mechatronic system design is thoroughly introduced including the soft
pneumatic actuators [128, 127] and syringe pump design [126]. The research delves into the
study of a soft gripper system formed by integrating those components. The soft pneumatic
actuators serve as the fingers driven by the syringe pump and the stable inversion algorithms.
The dynamical modeling of the systems based on mechanics and fluid dynamics theories
is presented in this section. The underactuated controller is also designed based on the
dynamical model as introduced in this section.

Mechatronic Design

The mechatronic system design is illustrated in Figure 6.2 (a), (b), and (c). The soft gripper
is composed of two main components, soft fingers and a syringe pump as in Figure 6.1. The
design methodology of each component will be elaborated in the following paragraphs.

Soft Actuator Design

The soft actuator is designed under an optimal model-based design framework which con-
siders force/torque, bendability, and controllability simultaneously during the design stage
as discussed in Chapter 3 [127]. The dimensional parameters of a soft pneumatic actuator
are as shown in Figure 6.2 (a), the cross-sectional view of the soft actuator's chamber room.
The optimal dimensional parameters are searched by the optimization framework below

$$
\begin{aligned}
\max_{a,b,w,t} \ & \bar{T}(p) + \bar{\theta}(p) \\
\text{s.t. } & \dot{p} = 0 \\
& a_1 \leq a \leq a_2 \\
& b_1 \leq b \leq b_2 \\
& h_1 \leq a + b \leq h_2 \\
& C_1 \leq Ew(a+b)^{n+2} \leq C_2
\end{aligned}
\tag{6.8}
$$
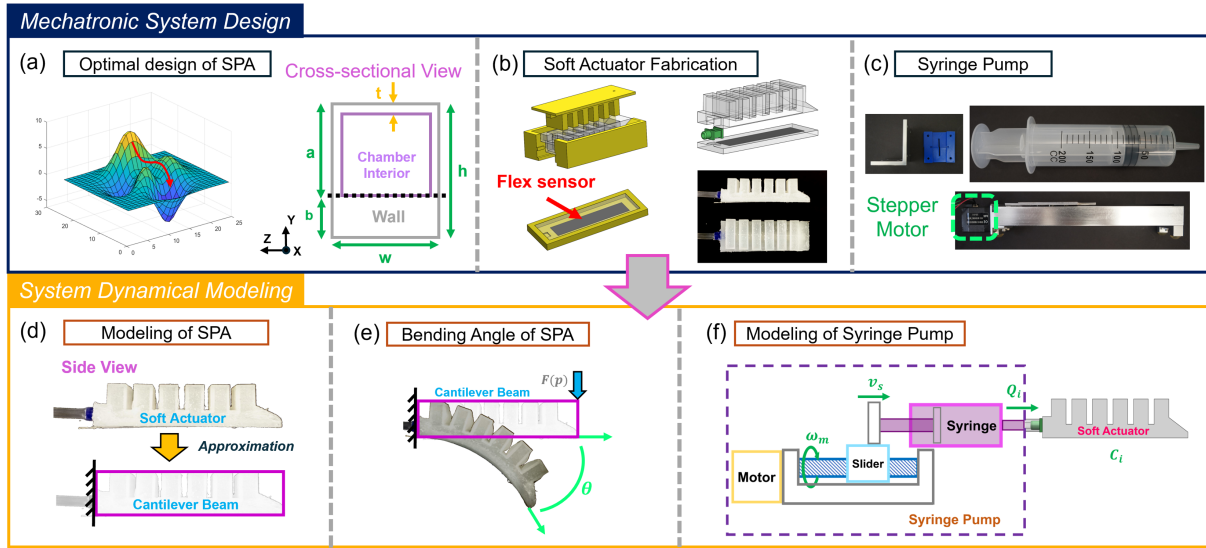
Figure 6.2: The design of the mechatronic system can be seen in (a), (b), and (c), while the system modeling is observed in (d), (e), and (f). (a) visualizes how the optimal dimensional parameters are searched in a non-convex space. (b) illustrates the fabrication process of the soft pneumatic actuator and the flex sensor is embedded during the fabrication process. (c) shows the appearance of the syringe pump, and it is made of a commercial linear actuator and a commercial syringe. The (d) and (e) visualize how the structure of the soft actuator is approximated by a cantilever beam and how the bending angle is measured. The modeling schematic of the syringe pump is displayed in (f).

where p is the pressure inside the chamber, a is the top of the chamber to the neutral surface, b is the neutral surface to the bottom of the chamber, $a+b$ is the height of the soft actuator as in Figure 6.2 (a), E is Young's modulus of the selected material, and n is a parameter related to soft materials and determined by experiments [62]. Note that w and t represent the width and wall thickness of the cross-sectional area (Figure 6.2 (a)). However, they usually hit the upper and lower bounds respectively, so they are not included in the (6.8) and determined by the designer.

The $\bar{T}(p)$ represents the Pressure-to-Force/Torque model which is obtained by mechanics analysis of the soft actuator [127], while the $\bar{\theta}(p)$ stands for the Pressure-to-Bending model which is derived by a nonlinear mechanics theory [62, 127]. Both $\bar{T}(p)$ and $\bar{\theta}(p)$ are functions of the dimensional parameters, a, b, w, and t as shown in Figure 6.2 (a). There exists an optimal parameter set that maximizes the objective function of (6.8), $\bar{T}(p)+\bar{\theta}(p)$ [127]. The parameter set is searched by optimization algorithms. The constraint of $Ew(a+b)^n$ aims to place the natural frequency of the soft actuator in the desired range. The remaining parameters which are not considered in the (6.8) include the Young modulus, length of the

structure, and number of chamber rooms. They will be discussed in the following paragraph.

The range of dimensional parameters is selected by referencing the size of human fingers [110, 108], so the constraint of a, b, and the value of w are determined and n is decided by the selected soft material. To position the natural frequency in the desired range (2 - 3 rad/s), the Smooth-on Ecoflex® Dragon Skin 20 is selected and its Young's modulus is 0.34 MPa. The length of the soft actuator and the number of chambers are coupled. The more the number of chambers, the longer the length. The length of 100 mm is chosen to avoid the buckling effect caused by the long structure and the corresponding number of the chamber rooms is 6.

The soft actuator is fabricated by two molds as illustrated in Figure 6.2 (b). There are upper and bottom components on the left side of Figure 6.2 (b). The Ecoflex® Dragon Skin 20 is in the liquid state, and its curing time is around 4 hours. A flex sensor is embedded into the bottom component as shown Figure 6.2 (b) before the liquid rubber becomes a solid state. When the two components are removed from the molds, they are bonded by the silicone adhesive Smooth-on Sil-poxy®, as shown in the top right of Figure 6.2 (b). The appearance of the soft actuator is as shown in bottom right of Figure 6.2 (b).

Syringe Pump Design

The schematic of the syringe pump is shown in Figure 6.2 (c), which is used to pressurize soft pneumatic actuators. The design of the syringe pump attempts to reduce the complexity of the pressure control and reduce the weight and size compared to traditional air pumps as introduced in Chapter 4. The syringe pump, inspired by the hydraulic system, is made of a commercial syringe and a commercial linear actuator. The syringe pump is driven by the linear motor in the linear actuator [126]. The pressure is adjusted by controlling the position of the slider.

The precision of the linear actuator and the volume of the syringe have an influence on the accuracy and controllability of the syringe pump. The linear actuator, Fulride by NSK Ltd., and a syringe with 150 mL are chosen to fabricate the syringe pump. The accuracy of the Fulride could be μm scale and the volume of the syringe could provide pressurize up to three soft actuators to generate $\pi/2$ rad. Some custom-made components are manufactured by 3D printers in order to assemble the syringe and the linear actuator.

Multi-finger Soft Gripper

Multiple soft pneumatic actuators and the syringe pump form a soft gripper module, which is assembled by 3D-printed connectors and rubber tubes. The detailed compositions of the soft gripper including sensor setup will be described in Section 6.4.

System Modeling

Prior to designing the proposed controller for the soft gripper, the full system dynamical model of both the soft actuators and the syringe pump is needed. The models of soft actuators and the syringe pump are cascaded to obtain the full system model matrix. The model of each component is developed in the following subsection.

Modeling Soft Actuators

The dynamical model of the soft pneumatic actuator is obtained by modeling its approximated structure as shown in Figure 6.2 (d). Since the linear model can capture the behavior of the real system within $\theta = 0$ to $4\pi/9 \ rad$ [131], a linear second-order model is utilized to model and capture its motions. The linear second-order model is described as [131]

$$\ddot{\theta} + (C_n/M_{eq})\dot{\theta} + (K_n/M_{eq})\theta = c \cdot p/M_{eq} \tag{6.9}$$

The state-space form is therefore written as

$$A_1 = \begin{bmatrix} 0 & 1 \\ -\frac{K_n}{M_{eq}} & -\frac{C_n}{M_{eq}} \end{bmatrix}, B_2 = \begin{bmatrix} 0 \\ 1 \end{bmatrix}, C_2 = \begin{bmatrix} \frac{c \cdot p}{M_{eq}} \\ 0 \end{bmatrix}^T \tag{6.10}$$

where $F(p)$ is represented as $c \cdot p$, c is a constant affected by a, b, w, and t [128]. If the system model of n_y fingers are stacked, the state-space form becomes

$$A_{stk} = \begin{bmatrix} A_1 & 0 & 0 \\ 0 & \ddots & 0 \\ 0 & 0 & A_{n_y} \end{bmatrix}, B_{stk} = \begin{bmatrix} B_1 \\ \vdots \\ B_{n_y} \end{bmatrix}, C_{stk} = \begin{bmatrix} C_1^T \\ \vdots \\ C_{n_y}^T \end{bmatrix} \tag{6.11}$$

According to (6.5), the system equation in the Laplace domain is obtained. Thus, the system model matrix $P(s)^{n_y \times 1}$ is described as

$$P(s) = \begin{bmatrix} \frac{c \cdot p/M_{eq}}{s^2 + (C_{n\_1}/M_{eq})s + K_{n\_1}/M_{eq}} \\ \vdots \\ \frac{c \cdot p/M_{eq}}{s^2 + (C_{n\_n_y}/M_{eq})s + K_{n\_n_y}/M_{eq}} \end{bmatrix} \tag{6.12}$$

where the equivalent mass of the soft actuators is almost the same and the same symbol M_{eq} is used. Although the two fingers share the same dimensional parameters such as height, weight, etc., their C_n and K_n in (6.9) are slightly different due to fabrication errors and uncertainty of soft materials.

$$
\begin{aligned}
C_1 &\leq C_n \leq C_2 \\
K_1 &\leq K_n \leq K_2
\end{aligned}
\tag{6.13}
$$

This nature leads to asynchronized motions when a feedback controller is applied. The different motions further lead to grasping failure [130]. One of the aims of this study is to address such grasping failures by utilizing the algebraic stable inversion approach for SIMO setting, and the experimental results will be presented in Section 6.4.

Modeling Syringe Pump

The configuration of the syringe pump is visualized in Figure 6.2 (f). The dynamical modeling of the syringe pump is shown in Section 4.2 of Chapter 4 [126], and the dynamical model is described as

$$
\dot{p} = \frac{Q_i}{C_i} = \frac{A_s l}{2\pi C_i} \omega_m
\tag{6.14}
$$

where A_s is the inner cross-sectional area of the syringe, l is the lead of the screw inside the linear actuator, Q_i is the output air flow rate of the syringe, C_i is the capacity of the soft actuator, and ω_m is the motor speed. The dynamics of the syringe pump is the first-order system. The maximum angular velocity of the motor is $5\ rev/s$. The C_i will expand as it is pressurized; however, its effect can be ignored as the input pressure is below $0.1\ MPa$ and the bending angle of the soft actuator is below $2\pi/3\ rad$. The C_i here is considered as a constant.

Full Model

The full model of a single soft actuator is the cascade of the (6.9) and (6.14).

$$
A_1 = \begin{bmatrix} 0 & 1 & 0 \\ 0 & 0 & 1 \\ 0 & -\frac{K_n}{M_{eq}} & -\frac{C_n}{M_{eq}} \end{bmatrix}, B_1 = \begin{bmatrix} 0 \\ 0 \\ 1 \end{bmatrix}, C_1 = \begin{bmatrix} \frac{c \cdot p A_s l}{2\pi C_i M_{eq}} \\ 0 \\ 0 \end{bmatrix}^T
\tag{6.15}
$$

The resulting systems from ω_m to θ are third-order and have a pole at the imaginary axis. Hence, the full system model matrix $P(s)^{n_y \times 1}$ in Laplace domain can be obtained by referencing (6.6) and (6.11)

$$
P(s) = \begin{bmatrix} \frac{c \cdot p A_s l / 2\pi C_i M_{eq}}{s^3 + (C_{n\_1}/M_{eq})s^2 + (K_{n\_1}/M_{eq})s} \\ \vdots \\ \frac{c \cdot p A_s l / 2\pi C_i M_{eq}}{s^3 + (C_{n\_n_y}/M_{eq})s^2 + (K_{n\_n_y}/M_{eq})s} \end{bmatrix}
\tag{6.16}
$$

The full system matrix is causal and the minimum phase.

Even though all finger angles (θ) remain within $[0, 4\pi/9]$, equation (6.15) cannot accurately capture the exact behavior of the soft gripper due to its inherent uncertainty structure [57]. To achieve a more accurate representation, the model in (6.9) can be modified by using a multiplicative uncertainty approach as in [138], defining a set of all possible plants for each finger as follows:

$$\Pi := \{(I + \Delta W_T)P \mid \forall \parallel \Delta \parallel_\infty \leq \gamma\} \tag{6.17}$$

Here, the transfer function $W_T \in \mathcal{RH}_\infty$ represents the spatial and frequency characteristics of the uncertainty. Δ denotes any unstructured and unknown yet stable function [138]. A general approach to defining the robustness weight function W_T is described below [26]:

$$\left| \frac{M_{ik}e^{j\phi_{ik}}}{M_i e^{j\phi_i}} - 1 \right| \leq |W_T(j\omega_i)|, i = 1, \ldots, m; k = 1, \ldots, n_r \tag{6.18}$$

The magnitude and phase values are assessed over a range of frequencies, denoted as ω_i (ranging from $i = 1$ to m), and the experiment is repeated n_r times. The notation (M_{ik}, ϕ_{ik}) refers to the magnitude-phase measurements corresponding to frequency ω_i and the kth experiment iteration, where $k = 1$ to n_r. Similarly, (M_i, ϕ_i) represents the magnitude-phase pairs for the nominal plant $P(s)$.

The following remark describes an important dependency of the uncertainty in SPAs:

Remark 3. *The single input (underactuated control) may lead to different motions of soft fingers with the same dimensional parameters due to the uncertainty of the soft materials. The deformation curves of some soft materials (Smooth-on Ecoflex series) exhibit high uncertainty when they have a slow deformation rate [16, 68]. In contrast, the curves demonstrate much less uncertainty when their deformation rate is high. Similarly, when a higher pressure changing rate is applied to soft fingers, they show a narrower uncertainty band, align more closely with nominal behaviors, and tend to have consistent motions. This property influences the performance of underactuated control of the multi-finger soft gripper (6.19) and helps achieve coordinated motions.*

Using the insight from the above remark, equation (6.17) can be redefined with respect to the operational speed ω_m. For simplicity, only two fingers are considered:

$$\Pi_H(\omega_m^H) := \left\{ \left(\begin{bmatrix} 1 & 0 \\ 0 & 1 \end{bmatrix} + \Delta \overbrace{\begin{bmatrix} W_{T1} & 0 \\ 0 & W_{T2} \end{bmatrix}}^{W_T^H} \right) \begin{bmatrix} P_1(s) \\ P_2(s) \end{bmatrix} \mid \|\Delta\|_\infty \leq \gamma \right\}$$

$$\Pi_L(\omega_m^L) := \left\{ \left(\begin{bmatrix} 1 & 0 \\ 0 & 1 \end{bmatrix} + \Delta \underbrace{\begin{bmatrix} W_{T1} & 0 \\ 0 & W_{T2} \end{bmatrix}}_{W_T^L} \right) \begin{bmatrix} P_1(s) \\ P_2(s) \end{bmatrix} \mid \|\Delta\|_\infty \leq \gamma \right\}$$

such that

$$\omega_m^H > \omega_m^L \implies \bar{\sigma}(W_T^H(j\omega_i)) < \bar{\sigma}(W_T^L(j\omega_i)).$$

where Π_H denotes the uncertain plant family with respect to high speed of actuation (ω_m^H) and Π_L defines the uncertain plants for low speed of actuation (ω_m^L). Thus, as the operational speed of the soft actuator increases, the variance in its behavior is reduced.

Controller Design and Analysis

If all the elements in $P(s)$ of (6.6) are the same(i.e., $P_1 = P_2 = ... = P_{n_y}$), the multiple systems will be coordinated automatically. However, the full system matrix of multiple soft fingers $P(s)$ which has different elements (i.e., $P_1 \neq P_2 \neq ... \neq P_{n_y}$) will be utilized to design the underactuated controller. The (6.6) for the desired output is re-formulated as

$$\begin{bmatrix} Y_{d1}(s) \\ \vdots \\ Y_{dn_y}(s) \end{bmatrix} = \begin{bmatrix} P_1(s) \\ \vdots \\ P_{n_y}(s) \end{bmatrix} U(s) \tag{6.19}$$

where $Y_d(s) \in \text{Im}_{\mathbb{R}(s)}(P)$. In (6.19), $Y_{di}(s)$ represents the desired output of $P_i(s)$, and $i = 1, ..., n_y$.

For the system described in (6.19), several types of controllers can be designed, including Model Predictive Control (MPC), iterative Linear Quadratic Regulator (iLQR), and Sliding Mode Control (SMC). Each of these controllers involves complex tuning during the design phase. In contrast, stable inversion, as presented in [59], offers a simpler alternative that achieves similar goals while providing the necessary robustness to handle uncertainties. Additionally, this approach allows for flexibility in adjusting the bandwidth of both the feedforward and feedback loops. This control structure, design methodology, and robustness margins are adaptable and will remain effective even if the system is modified to be square or overactuated by adding more actuators to the fingers. The algebraic framework of our controllers also facilitates the calculation of trackable trajectories (*Assumption 2. c.*).

The stable inversion is composed of the feedforward and feedback loop [59]. The feedforward controller is obtained by solving (6.19) to get $U(s)$ and the additional feedback loop aims to address the system perturbation of the mechatronic system as shown in Figure 6.3. Some theorems are introduced and will be implemented to design the algebraic control including the feedforward control and feedback loop.

Theorem 2. *(section III-B, [59]) Let $P(s)$ be non-square $(\text{rank}_{\mathbb{R}(s)}(P) = n_u < n_y)$, then there exists an $P^\dagger(s) := (P^T(s)P(s))^{-1}P^T(s)$ satisfying $P^\dagger(s)P(s) = I$. Besides, it is defined that $y_d(t)$ is the desired system response in the time domain and $y_d^a(t)$ is the system response by applying an approximate solution $U^a(s)$. Thus, an approximate solution $U^a(s)$ is defined as*

$$U^a(s) = H(s)P^\dagger(s)Y_d(s) \tag{6.20}$$

satisfying

    1) $H(s) \in \mathbb{R}(s)$
    2) $\| y_d^a(t) - y_d(t) \|_\infty < \infty \; for \; t \in [0, \tau]$
    3) $y_d^a(t) \approx y_d(t) \; for \; t \in (\tau, \infty)$
    4) $U^a(s) \in \mathcal{RH}_\infty$

Definition 1. *(section III-B, [59]) Let* ω_{cl} *denote the bandwidth (BW) of the system. So the filter is defined as*

    $H(j\omega) \approx I \Leftrightarrow \omega \ll \omega_{cl}$
    $H(j\omega) \approx 0 \Leftrightarrow \omega \gg \omega_{cl}$
    $H(j\omega) \not\approx \{0, I\} \Leftrightarrow \omega \; close \; to \; \omega_{cl}$

Remark 4. *The* $P^\dagger(s)$ *in (6.20) contains non-causal elements. To make it applicable to real systems, the* $H(s)$ *could be loop-shaping synthesis [138] or a low-pass filter [34] to re-shape the* $P^\dagger(s)$. *Considering a general case, a system would be minimal or non-minimal. Loop-shaping synthesis is applied to shape the (6.20). However, if the system is minimal as stated in the Assumption 2 and has a lower order, the low-pass filter, which is relatively more applicable, can be utilized to shape the (6.20). The order of the low-pass filter depends on the relative order (l) of* $P^\dagger(s)$. *The low-pass filter takes the form of* $\frac{a_0}{s^l + a_{l-1}s^{l-1} + \ldots + a_0}$. *The parameters* $a_0, \ldots a_{l-1}$ *in the equation are selected to define the cut-off frequency of the low-pass filter.*

Remark 5. *An alternative reason to apply* $H(s)$ *is that using the* $P^\dagger(s)$ *in (6.20) directly in the feedforward or feedback controllers can cause undesired high-frequency excitation. Thus, an appropriate selection of the either cut-off frequency of the low-pass filter or the bandwidth of the resulting complementary sensitivity function of the loop shaping can prevent this excitation. As demonstrated in the experimental part, there is a definite advantage of letting the bandwidth of* $H(s)$ *be as large as possible so that the better synchronization of multiple fingers be achieved due to the nonlinear nature of the material of soft fingers.*

The tracking error (with the perturbed term) can be compensated by using the output feedback as displayed in Figure 6.3. The u_{ff} is calculated based on the *Theorem 2*. It is assumed that the output of the real (uncertain) system can be measured such as sensors or observers. Since the nominal system output can be computed with the combined input u_c, we have the output difference $y_\Delta(t)$. With this output difference, we can compensate for the error by the following theorem.

Theorem 3. *[59] Consider the block diagram in Figure 6.3 with (6.17). Then the bounded* U_{fb} *yields* $\| y_d(t) - \tilde{y}(t) \|_\infty \to 0$ *iff* $\tilde{Y}(s) \in \text{Im}_{\mathbb{R}(s)}(P)$, *where* $y_d(t)$ *is the desired response and* $\tilde{y}$ *is the real system response.*
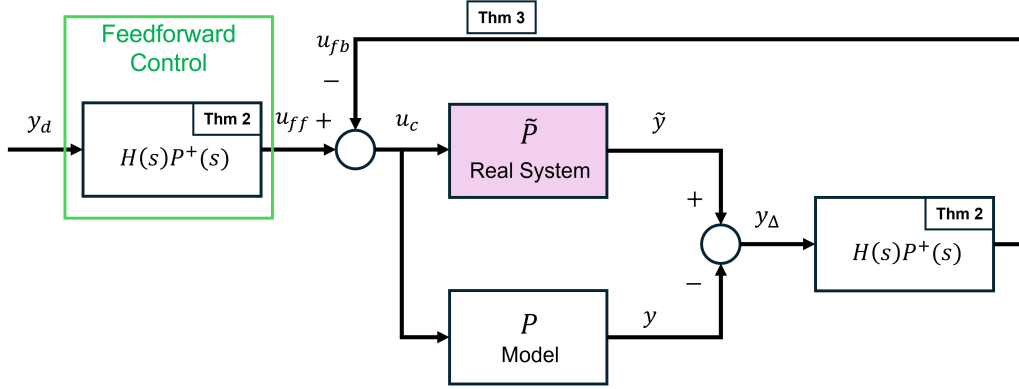
Figure 6.3: The block diagram of the proposed controller including the feedforward control
and feedback loop.

For notational simplicity, the ΔW_T is taken as Δ_P, and consider $\tilde{P}(s) \in \Pi$, $Y_d = PU_{ff}$,
and $U_c(s) := U_{ff} - U_{fb}$ (by referencing Figure 6.3)

$$\tilde{P}(s)U_c(s) = \tilde{Y}(s) = PU_c + \Delta_P PU_c \tag{6.21}$$

$$PU_{ff} + \Delta_P PU_{ff} - PU_{fb} - \Delta_P PU_{fb} = \tilde{Y}(s) \tag{6.22}$$
$$\Rightarrow PU_{fb} = \Delta_P PU_{ff} - \Delta_P PU_{fb} \tag{6.23}$$

The feedback loop will compensate for the model errors. The proof of *Theorem 2* and *3* are
given in [59].

The model inversion and feedback loop are introduced to achieve accurate tracking of
the system. The next problem is whether the system performance can be achieved by
underactuated control as depicted in (6.19). That is, multiple soft actuators are controlled
with a single input pressure. Here, the goal is to control the motions of the multi-finger
gripper to reach stable grasping [130]. The desired response of each finger is assigned as Y_d
in (6.19) and the $Y_d(s) \in \text{Im}_{\mathbb{R}(s)}(P)$. This problem will be shown to be solvable and the
solution to exist through mathematical inference. Since the $P(s)$ has full rank $= 1$, the $P(s)$
is invertible and exists left inverse matrix according to the *Theorem 2*. The pseudo-inverse
is $P^\dagger(s) = (P^T(s)P(s))^{-1}P^T(s)$. The controller is obtained by $U^a(s) = H(s)P^\dagger(s)Y_d(s)$.
Therefore, there exists input $U(s)$ that makes the $Y_d(s)$ achievable.
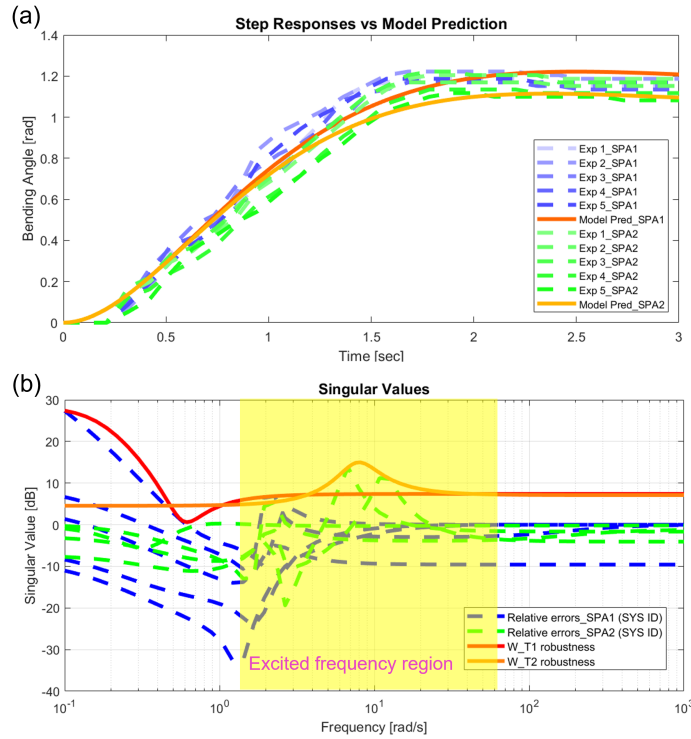
Figure 6.4: Several open-loop responses of both soft pneumatic actuators (soft fingers) are demonstrated in (a). The robustness weight selection of both soft fingers based on the modeling errors can be seen in (b).

6.4 Experimental Evaluation

In previous sections, the mechatronic system, specifically the multi-finger soft gripper, is introduced, alongside system dynamical models and control algorithms. Prior to experimentation, preliminary tests are conducted using MATLAB®/Simulink to assess the feasibility of the stable inversion algorithm. Subsequently, a series of experiments are executed to evaluate the practicality of the proposed control approach. An additional disturbance test is then performed to evaluate the robustness of the controller.

Preliminary Evaluations

Some definitions and assumptions are applied in Section 6.2 and 6.3. This subsection intends to evaluate whether the definitions and assumptions are valid before the simulations and experimentation.

Model Evaluation

The analytical model is built for the mechatronic system as $P(s)$ in (6.26). Based on the discussion in Section 6.3, a more accurate representation of the dynamical system can be achieved via multiplicative uncertainty form, while the nominal choice in (6.26) includes some errors or inaccurate representation due to lack of measurement and estimation capabilities. Equation (6.17) gives the explicit form of the multiplicative uncertainty over the nominal plant where the unstructured uncertainty is assumed to be bounded as $\|\Delta\|_\infty \leq 1$. Several step responses of both soft fingers are conducted to validate this boundedness assumption.

Figure 6.4 (a) demonstrates the repeated step responses of the two soft actuators, the first (blue lines) and second (green lines) element of the $P(s)$ in (6.26). The system performance varies due to the time-varying or unmeasurable properties of soft materials [130]. The singular value of the bounded constraint in (6.18) can be found in Figure 6.4 (b). The system perturbation of two soft actuators is bounded. Specifically, based on the (6.13), it is observed that $\| C_n - C_{nominal} \| \leq 14.3\%$ and $\| K_n - K_{nominal} \| \leq 5.9\%$ by performing system identification of the step responses in Figure 6.4 (a). The $C_{nominal}$ and $K_{nominal}$ are the average of the identified model of those multiple step responses. Two soft actuators, both elements of the $P(s)$ in (6.26), show a similar result. It is concluded that the perturbations of the two systems are bounded, confirming the validity of the model evaluation. This evaluation holds within the specific frequency range caused by the test input's excitation frequencies from 6 to 63 rad/s as the yellow region in Figure 6.4 (b), determined by performing the Fast Fourier transform on the input command as shown in Figure 6.4 (a).

Controllability Evaluations

Another preliminary evaluation is needed before the experimentation. The system equation of (6.5) should be controllable and observable to ensure that the system realization is minimal. Note that if the two fingers are identical, the realization is uncontrollable. In this case, the motion of the two fingers is always synchronized. If the controllability matrix $M_c = [A, \ BA, \ BA^2, \ \cdots]$ and the observability matrix $M_o = [C \ CA \ CA^2 \ \ldots]^T$ of (6.6) both have full rank, the full system is controllable and observable. Since the full system is controllable and observable, the system realization is also minimal. This evaluation matches the *Assumption 2. a.* The proposed control method is valid.

Uncertainty Band of Soft Finger

It is observed that the soft materials exhibit larger uncertainty as discussed in *Remark 3* Section 6.3. The experimental evaluation of this property is conducted and visualized in Figure 6.5 (a) and (b). The left finger in Figure 6.1 is used to conduct this evaluation. Two input commands with different motor speeds driving the syringe pump are applied to do step response tests of a soft finger. The slower-speed input command excites a larger uncertainty band. The standard deviation of the steady-state error is 2.41 deg (green lines), while that of higher-speed input command is 1.14 deg (blue lines). The input commands in
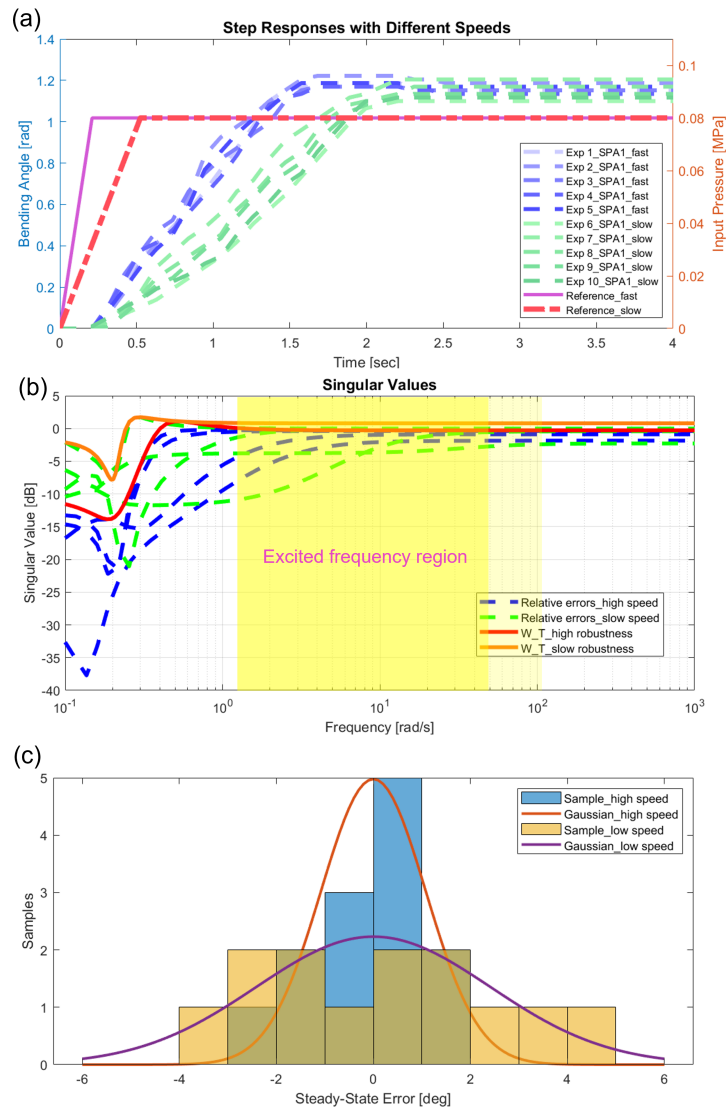
Figure 6.5: The step responses of different speeds of SPA1 (left finger in Figure 6.1) are shown in (a). The robustness weight selection of SPA1 with high and slow speeds based on the modeling errors can be seen in (b). The histogram of steady-state errors for SPA1 (left finger in Figure 6.1), at both high and low speeds, is illustrated in (c).

Figure 6.5 (a) are converted to the frequency domain using the Fast Fourier transform to validate the excited frequency region, as the yellow in Figure 6.5 (b). This soft actuator's frequency region spans from approximately 6 to 50 rad/s. Figure 6.5 (b) illustrates that the magnitude variations of the soft actuator converge at higher frequencies, approaching the nominal dynamics. These results confirm that the soft actuator demonstrates reduced

uncertainty and approximates nominal dynamics at higher speeds (or frequencies), consistent
with the observations in the time domain.

Furthermore, the histogram of steady-state errors for the left finger in Figure 6.1 is
depicted in Figure 6.5 (c). The distribution at high speed is more concentrated around the
nominal responses, whereas the distribution at low speed is more flattened. That further
proves that low-speed responses excite more uncertainty. The errors of the soft actuator at
low speed are more unpredictable, so the corresponding standard deviation is larger than
that at high speed. This property plays a vital role in the multiple soft finger underactuated
control since soft fingers have different dynamical models. Higher speeds may reduce the
uncertainty band and help coordinate multiple soft fingers within a soft gripper.

Simulation Results

Section 6.2 introduces the general case of the problem (6.6). The system matrix $P(s)$ com-
prises n_y elements. Simulations will be conducted on multi-finger soft gripper systems to
assess different scenarios, with n_y taking the value of 2 for $P(s)$. The simulations help us
understand if the controller can work and regulate the system outputs. Besides, the low pass
filter $H(s)$ of *Theorem 2* will be adjusted to achieve better tracking performance.

The simulation is performed on a two-finger gripper, which includes two soft actuators
(soft fingers) and a single syringe pump. The ideal desired output is selected as a step
response $Y_d = [\frac{0.333\pi}{s}, \frac{0.333\pi}{s}]^T$. As the elements in $P(s)$ are nonidentical in (6.26), the Y_d is
not in the image space of P and it can be factorized as [59]

$$Y_d = \underset{\text{Im}(P)}{proj}(Y_d) + res(Y_d) \tag{6.24}$$

$$\underset{\text{Im}(P)}{proj}(Y_d) = \sum_{n=1}^{r} \langle Y_d, q_i \rangle q_i \tag{6.25}$$

where $q_i s$ is defined in (6.1). The $res(Y_d)$ can be obtained by $Y_d - proj(Y_d)$ based on (6.24)
and (6.25). Note that the obtained desired output vector may lead to the collision of the two
soft fingers as Figure 6.1, but the simulation aims to check the performance of the control
algorithm. With the $res(Y_d)$, $proj(Y_d) = [0.303\pi/s, 0.357\pi/s]^T$ is in the range space of P.
The system equation is written as

$$\begin{bmatrix} \frac{0.303\pi}{s} \\ \frac{0.357\pi}{s} \end{bmatrix} = \begin{bmatrix} \frac{7.831}{s^3+2.66s^2+3.61s} \\ \frac{7.831}{s^3+2.45s^2+3.06s} \end{bmatrix} U(s) \tag{6.26}$$

The systems in (6.26) will have steady-state tracking errors, 0.030π (SPA 1) and -0.024π
rad (SPA 2) respectively compared to the desired reference ($\pi/3$ *rad*). The controller is
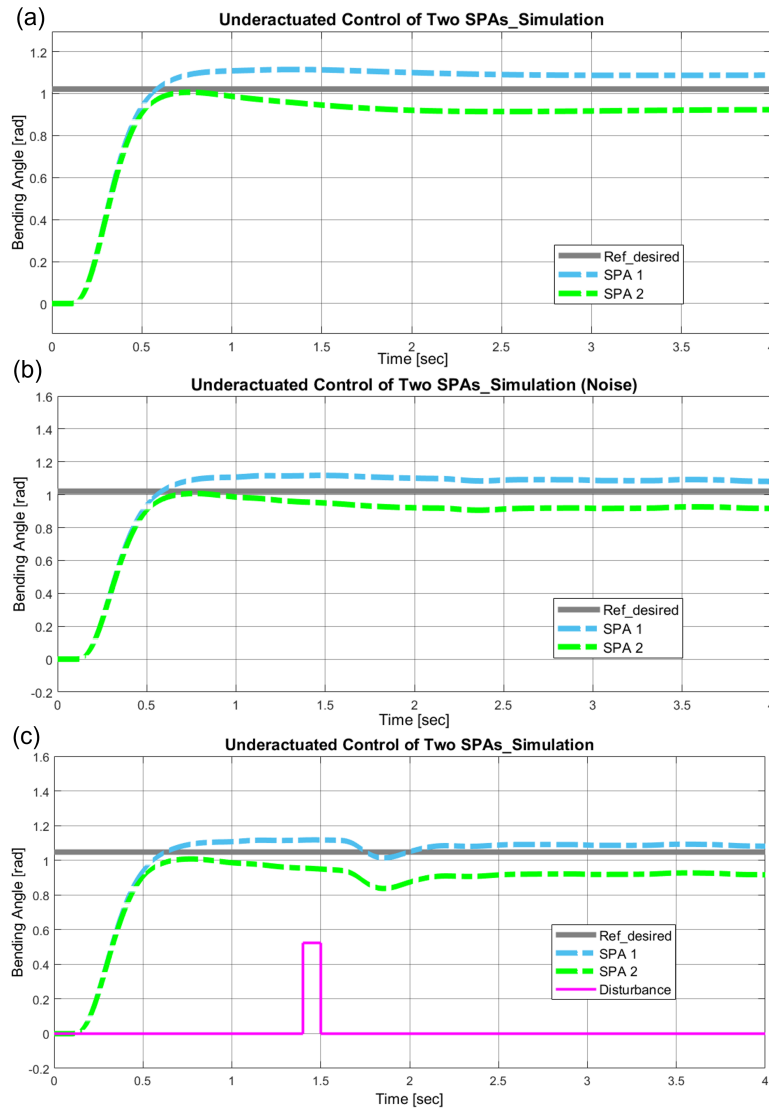
Figure 6.6: The simulation results of the two-finger gripper are shown in (a). The sensor noise and disturbance are considered and displayed in (b) and (c).

obtained based on the *Theorem 2* and *3*, so the $P^{\dagger}(s) = [\frac{s^3+2.66s^2+3.61s}{15.66},$ $\frac{s^3+2.45s^2+3.06s}{15.66}]$ and the $H(s)$ is designed by loop-shaping the element of $P^{\dagger}(s)$ with desired equation $4.8/s$, and $H(s) = \frac{1009s^3+2.52e5s^2+6.829e5s+1.027e6}{s^6+282.7s^5+6.14e3s^4+8.022e4s^3+4.335e5s^2+8.948e5s+1.027e6}$.

This controller is able to coordinate the motions of the two fingers within the soft gripper as in Figure 6.6 (a). The settling time of both fingers is approximately 0.6 *sec*, making the soft gripper comparable to traditional grippers. The tracking error of the two fingers is within

1 *deg* compared to the proj(Y_d). To further evaluate the performance of the controller, sensor noise and disturbance are added as Figure 6.6 (b) and (c). The feedback loop can compensate for the sensor noise as Figure 6.6 (b). The root-mean-square error (RMSE) of the sensor noise is around $\pm$ 2 *deg* [130]. The RMSE of the two fingers is within 0.5 *deg*, so the sensor noise does not affect the systems' output.

The disturbance here is regarded as the soft fingers are hitting by an external force. The results show that the controller is capable of adjusting the system back to the reference as Figure 6.6 (c). The amplitude of the errors for both fingers is within 0.1 *rad*, so the feedback control can handle the disturbance. The simulation results validate the *Theorem 3* and (6.23). The experimental results can be referenced in *Underactuated Control Tests* and *Disturbance Tests*.

The simulation results on two-finger soft grippers endorse the feasibility of the proposed controller algorithm. The motions of fingers are coordinated. These dynamics will be beneficial to grasping tasks when the soft gripper is applied to manipulate various objects. The controller will be applied to the real soft gripper to evaluate the applicability of this control algorithm.

Experimental Setup

Figure 6.1 illustrates both the experimental arrangement and the signal flow diagram. The two-finger soft gripper is used to conduct the experiments with a single syringe pump. The soft actuators are fabricated by molds as illustrated in Figure 6.2 (b). The motions of the soft fingers are driven by the syringe pump [126], which is actuated by a stepper motor. A DM320T digital stepper driver (StepperOnline, New York, NY) is utilized to trigger the stepper motor. An air pressure sensor (Walfront, Lewes, DE) with a sensing range of 0 to 80 *psi* is utilized to detect the air pressure for open-loop control. Additionally, each soft finger contains a flex sensor (Walfront, Lewes, DE) inside to monitor its bending angle, facilitating feedback control. The flex sensor is a resistive type sensor and has a sensing range of 100 *deg* and sensing error is approximately 2 *deg* (root-mean-square error). Both sensors are synchronized with Arduino MEGA 2560 (SparkFun Electronics, Niwot, CO), which is based on the Microchip ATmega 2560. The controller algorithms are programmed in MATLAB®/Simulink which is communicated with the Arduino MEGA 2560 to process feedback signals and generate control commands for the mechatronic system. The model and controller are discretized in the analytical software with a sampling time of 100 *ms*. The "Real System" in Figure 6.3 is replaced by the real soft gripper.

Open-loop & Closed-loop Tests

Prior to implementing the proposed controller, the open-loop tests attempt to visualize the open-loop responses of the soft fingers. The soft fingers have the same dimensional parameters such as height, width, length, etc. Nonetheless, their system parameters in (6.16) differ, resulting in distinct motions. In applications, the open-loop control results in
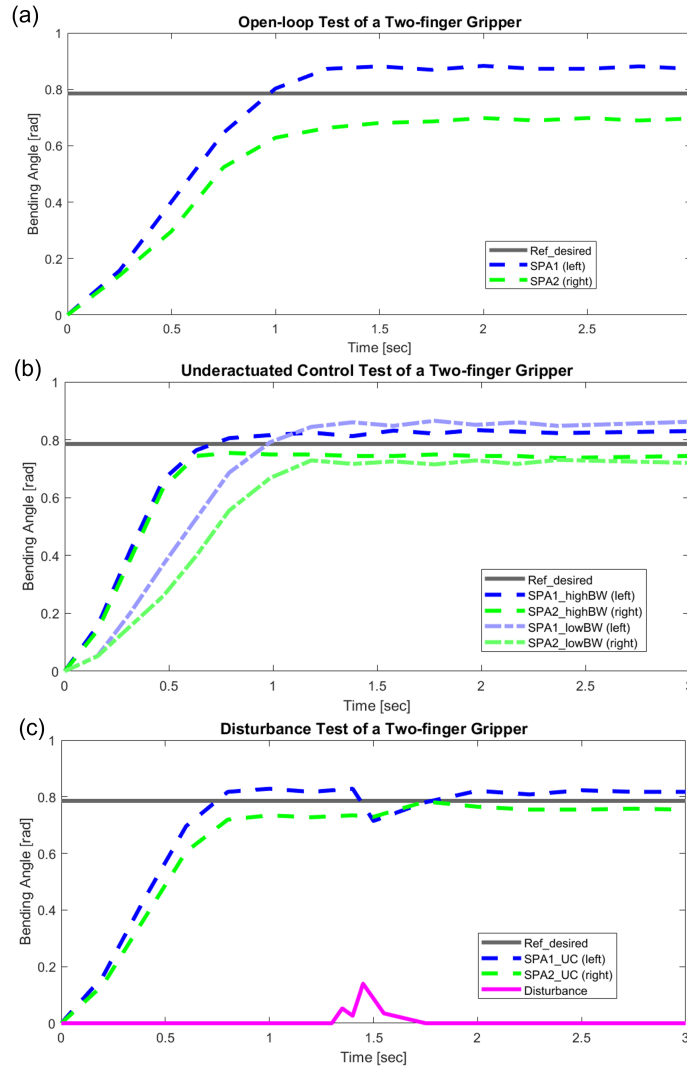
Figure 6.7: The visualization of the open-loop test of the two-finger gripper is displayed in (a). The responses of using the proposed controllers designed for different bandwidths are demonstrated in (b). The motions of the two fingers are coordinated compared to the results in (a). The disturbance test is depicted in (c) and the controller can handle the external disturbance.

inconsistent motions of multiple fingers which is not beneficial for manipulation tasks. The open-loop test results are illustrated in Figure 6.7 (a).

The desired reference is set as 45 deg ($\pi/4\ rad$) to avoid real collision between two fingers. Based on the (6.24) and (6.25), the desired references for left and right fingers are 48.24 and 40.86 deg, respectively. The blue dashed line represents the response of the left finger (SPA

1) in Figure 6.1 while the green dashed line denotes the right finger (SPA 2) in Figure 6.1. The left finger is active and responds faster. By contrast, the right finger has relatively slow responses. Their steady states are also different due to different system parameters of (6.16). The left finger reaches approximately 50 *deg* while the right finger reaches around 39.5 *deg*.

Underactuated Control Tests

The stable inversion algorithm in Section 6.3 is implemented to control the two fingers in this subsection. The system equation is similar to (6.26) in Section 6.4 and is described as

$$\begin{bmatrix} \frac{0.227\pi}{s} \\ \frac{0.268\pi}{s} \end{bmatrix} = \begin{bmatrix} \frac{7.831}{s^3+2.66s^2+3.61s} \\ \frac{7.831}{s^3+2.45s^2+3.06s} \end{bmatrix} U(s) \tag{6.27}$$

where $P^\dagger(s)$ and $H(s)$ are the same as shown in Section 6.4, and the desired reference is set as 45 *deg* ($\pi/4$ *rad*). According to the (6.24) and (6.25), the $Y_d = [0.25\pi/s, 0.25\pi/s]^T$ is factorized as proj(Y_d) and res(Y_d). The proj(Y_d) = $[0.227\pi/s, 0.268\pi/s]^T$ is in the range space of $P(s)$, and the steady-state tracking errors of systems in (6.27) are 0.023π and -0.018π *rad* respectively compared to the desired reference $\pi/4$ *rad*.

The result is demonstrated in Figure 6.7 (b). Two soft fingers reach their steady states at nearly the same time, and their tracking errors are below 1 *deg* compared to the proj(Y_d). The settling time is around 0.7 *sec*, which is better than our previous research by using an optimal controller [130]. The response time enables the soft gripper to be comparable to rigid grippers. Besides, their transient states are nearly synchronized with around 2 *deg* differences, which support the evaluation of *Uncertainty Band of Soft Finger*.

Additionally, the bandwidth of $H(s)$ affects the systems' responses, so another controller is designed whose $H(s)$ has narrower bandwidth. The $H(s)$ is designed by loop-shaping the element of P†(s) with desired equation $2/s$, and $H(s) = \frac{49.47s^3+1991s^2+4917s+6270}{s^6+51.21s^5+442.5s^4+2339s^3+6400s^2+9281s+6270}$. The experimental results are also shown in Figure 6.7 (b). The response of each finger is slower, and the settling time is around 1.1 *sec*. The error of each finger is larger compared to the performance of the controller with a larger bandwidth.

Due to the proposed controller, system response is quicker and reduce the uncertainty band of soft actuators. A previous work [130] utilized a syringe pump for each soft finger of the two-finger gripper to reach synchronization. However, one more syringe pump is needed compared to this research. If there are three-finger or four-finger grippers, more syringe pumps are required, which implies more costs, space, and weight. That makes the applications of the soft gripper setup more difficult.

Disturbance Tests

According to the *Theorem 3*, the feedback loop is designed to deal with the model errors or disturbances caused by external forces based on the *Theorem 3* ((6.21) and (6.23)). The
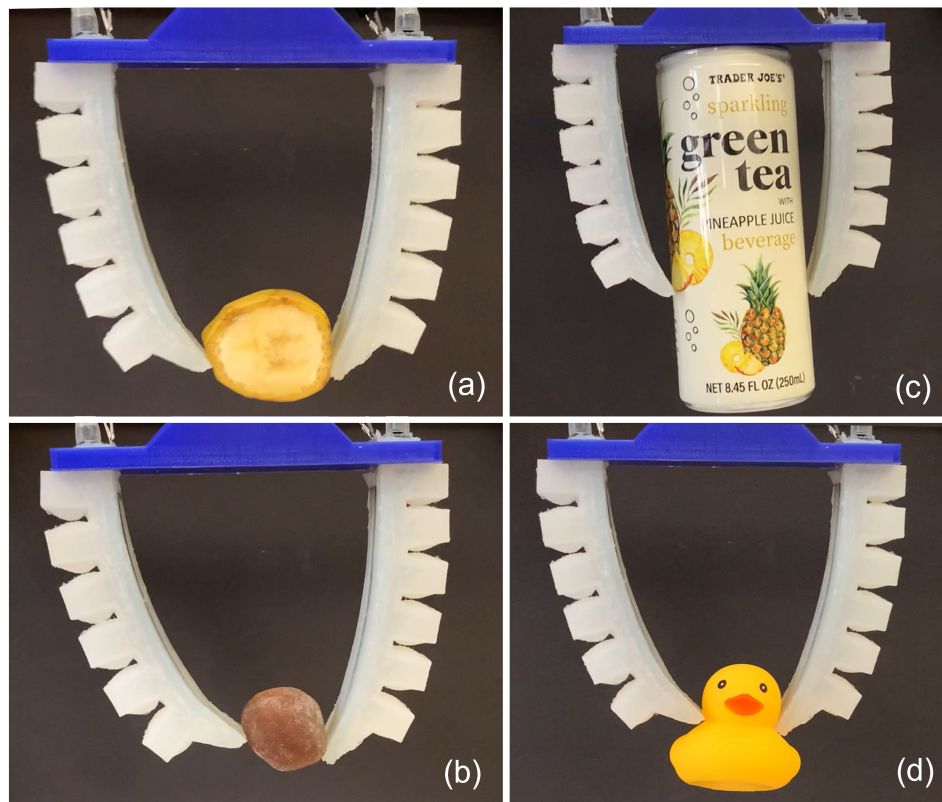
Figure 6.8: The two-finger soft gripper is used to grasp elastic objects such as a sliced banana (a), a mochi (b), an empty bottle (c), and a toy (d).

disturbance is generated by a human finger and is given at around t = 1.4 sec when the fingers arrive at the steady state as Figure 6.7 (c). The external force is only applied to the left finger. The proposed control algorithm is able to regulate the systems to the desired reference when the external force is applied. The experimental results support the *Theorem 3*.

Grasping Tests

The proposed control approach has been verified in the following subsections. The final test involves a grasping experiment using a two-finger gripper to handle various elastic objects. The results are illustrated in Figure 6.8. The soft gripper successfully manipulates items, including a sliced banana, a mochi, an empty bottle, and a toy with an underactuated control framework. Specifically, a single syringe pump is employed to control the multi-finger soft gripper.

6.5   Discussion and Summary

Discussion

The proposed control algorithms successfully coordinate the motions of two soft fingers within a soft gripper. The performance is validated by the real-world experimentation. However, if systems have identical model (i.e., $P_1 = P_2 = ... = P_{n_y}$ in (6.6)), those systems will automatically coordinate their motions given an input $U(s)$. Since the model of soft fingers are different (i.e., $P_1 \neq P_2 \neq ... \neq P_{n_y}$ in (6.6)), this approach is proposed to address this issue and coordinate their motions. Even if the soft fingers have the same dimensional parameters, their system models are different due to the properties of soft materials [16].

Furthermore, there is a limitation due to the hardware configuration of the soft gripper. The soft gripper has a parallel nature of multiple fingers driven by a single syringe pump. If the desired output function is out of the image space of $P(s)$, the proposed method is no longer valid. For instance, if the desired function of one finger is $\pi/4$ and another one is $-\pi/4$, the solution of the system (6.19) does not exist. The negative bending angle is out of the image space of this soft gripper.

The proposed approach sets the input-output relation characterized by $H(s)$, either a low-pass filter or designed by loop-shaping. The system responses are influenced by the $H(s)$. By enlarging the bandwidth of $H(s)$, the output moves toward the steady-state angle faster. Thus, the system responses are optimized by designing a suitable $H(s)$ as shown in both *Simulation Results* and *Underactuated Control Tests*. The simulation and experimental visualizations are depicted in Figure 6.6 (a) and Figure 6.7 (b). The steady-state angle of each finger comes closer to the desired angle, and as a result, better coordination is achieved.

The soft gripper, utilizing an underactuated control framework, effectively manipulates various elastic objects, as demonstrated in Figure 6.8. While other control strategies could potentially match the performance of this framework. For example, the two-finger soft gripper with finely tuned LQR controllers, which could achieve comparable response times and steady-state errors [130]. However, it requires additional air pumps. In contrast, the proposed control framework simplifies the mechatronic system by reducing the number of syringe pumps, thereby lowering costs and enhancing the applicability of the multi-finger soft gripper.

Summary

This chapter investigates the underactuated control of multiple fingers within a soft gripper, validating a controller designed with feedforward and feedback loops based on stable model inversion. The soft fingers are developed using an optimal design framework, and their dynamic models are derived from mechanical principles. The parameter-varying uncertainties in system models are examined both theoretically and experimentally. The proposed feedforward controller utilizes stable inversion of the system model, while the feedback loop addresses system perturbations. Simulation results demonstrate the effectiveness of the con-

trol algorithms in managing a two-finger gripper, and experimental validation confirming the controller's capability to coordinate motions effectively. The system achieves high-speed transient responses and minimal steady-state errors, even in the presence of disturbances. Grasping tasks further validate the control algorithms, which reduce the number of required inputs (air pumps), potentially benefiting the implementation of multi-finger soft grippers.

Chapter 7

Conclusion

7.1 Chapter Summary

Soft robotics has become an emerging field, and popular research topics include sensing, actuation, and control of soft robots. The dissertation, therefore, focuses on those common research topics and develops sensing, actuation, and control technologies for soft robots. Some functional soft devices and control algorithms are developed and successfully implemented in real-world scenarios. The summary of each chapter is discussed below.

Chapter 2 presents the development of a multifunctional soft tactile sensor designed by applying bio-inspired strategies. The soft sensor is able to detect contact force, contact location, and contact patterns. There are two layers inside the soft sensor. The bottom contains pieces of conductive fabric whose resistance value changes with the contact force. The resistance value is mapped to force by a machine learning approach. The top layer is a sensor array that can detect contact location, and another machine learning algorithm classifies the contact features.

Chapter 3 proposes an optimal model-based design approach for soft actuators that considers both kinematic and dynamic properties during the mechanical design stage. The model of pressure-to-force/torque and pressure-to-bending of soft actuators are developed by referencing nonlinear mechanics. Both models serve as the objective function of the optimization formulation. Moreover, the dynamic model for the soft actuator is created and used as another constraint in the optimization formulation, which aims to place the natural frequency in the desired range. Two optimization algorithms explore the optimal dimensional parameters and obtain almost the same design parameters. The soft actuator fabricated by those parameters is validated as having the optimal force/torque, bending angle, and natural frequency in the desired range.

Chapter 4 designs a syringe pump to drive the soft pneumatic actuator designed in chapter 3. The syringe pump intends to replace the air pump, which is bulky and hard to control. Instead, the syringe pump is relatively lightweight and easy to control since it is driven by a linear motor. The syringe pump comprises a commercial syringe, a linear

actuator, and 3D-printed components. Parametric analysis is conducted to select the suitable design parameter, such as the syringe size and the linear actuator. The best parameter set achieves a good response. Still, it leads to unexpected system vibration, so a set of suitable parameters is selected that achieves a fast response and does not have unexpected dynamics. The syringe pump is implemented to drive the soft actuator.

Chapter 5 discusses the modeling strategies for soft pneumatic actuators introduced in Chapter 3. The soft actuator exhibits nonlinearity; however, its dynamics can be approximated to linear ones within a range of 0–80 *deg*. The soft actuator can be simplified as a bending beam whose dynamics are close to a second-order equation. The nonlinear model has a similar form but has a nonlinear spring term. The linear model is valid with the range of 0–80 *deg*, while the nonlinear model is still valid when the bending exceeds 80 *deg*. This research focuses on using the soft actuators as fingers, so the linear model meets the requirements. If the soft actuator is applied for other purposes, the linear model is not adequate, and the nonlinear model should be used.

Chapter 6 develops the underactuated control algorithm of multiple soft fingers of a soft gripper via stable model inversion. Practically, the various fingers of a soft gripper can be coordinated by multiple syringe pumps, which occupy space, increase costs, and make the gripper hard to implement. This chapter improves this issue by developing underactuated control techniques via model inversion. The algorithms successfully control the motions of multiple fingers of a soft gripper with a single syringe pump and reduce the number of syringe pumps, reducing weight and saving space and costs. Another contribution of this project is the theoretical and experimental investigation of parameter-varying uncertainties in soft pneumatic actuators. The experiments demonstrate that the multiplicative uncertainty envelope changes with the operational speed of the soft actuators. The level of uncertainty change as their speed varies.

7.2 Future Works

Some open issues are raised during the study of this research. This subsection presents a couple of directions for future works.

Uncertainty of Soft Materials for Soft Device Design

The soft sensor introduced in Chapter 2 is functional but has limitations. The soft tactile sensor needs to be calibrated before implementation due to performance drift, which arises from the uncertain nature of soft materials. The uncertainty of soft materials results from the change in the microstructure. The bonding energy is relatively low compared to metals, so the bonding inside soft materials will easily break and re-generate during loading and unloading cycles [81]. If this phenomenon is transparent and can be predicted, it will help polish the soft device design and make uncertainty less uncertain.

Optimal Design of Soft Actuator Considering Multiple Metrics

Chapter 3 proposes an optimal design approach incorporating kinematic and dynamical properties in the loop. However, other properties, such as the weight and size of soft actuators, cannot be considered within the current framework. The optimal dimensional parameters are found by applying the proposed framework; however, those parameters may lead to weight increase or size increase, which are influenced by the dimensional parameters. For example, the weight equals its density times the volume, which is determined by height, width, and wall thickness. Thus, a revised framework that further includes weight and size in the loop will enhance the design of a soft pneumatic actuator.

Underactuated Control Algorithm Improvements

The proposed underactuated control algorithm in Chapter 6 successfully controls and coordinates the motions of multiple soft fingers within a soft gripper. Nonetheless, the algorithm has limitations. First, the desired output function must lie within the range space of the model matrix. Second, the current control framework suffers from a delay issue that slightly alters the control commands, causing the output function to fall outside the model's range space. This delay arises from two sources: the transmission time from the microcontroller to the soft fingers and the response delay of the soft actuators. The response delay is due to the soft materials used in the actuators; when pressurized, these actuators first expand their chambers before generating bending throughout the structure. The combination of the two issues leads to the failure of coordinated motions of multiple fingers. Therefore, the algorithm can be enhanced by addressing the delay issue and simplifying its implementation. Alternatively, learning-based approaches show potential to address this issue. For example, researchers could apply reinforcement learning to learn the desired output function in a simulator and then transfer it to real-world soft robots.

Bibliography

[1]   Gursel Alici et al. "Modeling and experimental evaluation of bending behavior of soft pneumatic actuators made of discrete actuation chambers". In: *Soft Robotics* 5.1 (2018), pp. 24–35.

[2]   Brian DO Anderson and John B Moore. *Optimal control: linear quadratic methods.* Courier Corporation, 2007, pp. 255–358.

[3]   E. N. Antoniou, A. I. G. Vardulakis, and Stavros Vologiannidis. "Numerical computation of minimal polynomial bases: A generalized resultant approach". In: *Linear Algebra and Its Applications* 405 (2005), pp. 264–278.

[4]   Costanza Armanini et al. "Soft robots modeling: A structured overview." In: *IEEE Transactions on Robotics* 39.3 (2023), pp. 1728–1748.

[5]   Milad Azizkhani, Mohammad Zareinejad, and Mohammad A. Khosravi. "Model reference adaptive control of a soft bending actuator with input constraints and parametric uncertainties". In: *Mechatronics* 84 (2022), p. 102800.

[6]   Jose Barreiros et al. "Self-Sensing Elastomeric Membrane for Haptic Bubble Arrray". In: *IEEE International Conference on Soft Robotics (RoboSoft)*. IEEE. 2020, pp. 229–236.

[7]   T. Beda. "An approach for hyperelastic model-building and parameters estimation a review of constitutive models." In: *European Polymer Journal* 50 (2014), pp. 97–108.

[8]   Charles M. Best et al. "A New Soft Robot Control Method: Using Model Predictive Control for a Pneumatically Actuated Humanoid". In: *IEEE Robotics and Automation Magazine* 23.3 (2016), pp. 75–84.

[9]   Stephen Boyd and Lieven Vandenberghe. *Convex Optimization.* Cambridge university press, 2004.

[10]   Leo Breiman. "Bagging predictors". In: *Machine Learning* (1996), pp. 123–140.

[11]   M. Brojan, T. Videnic, and F. Kosel. "Large deflections of nonlinearly elastic non-prismatic cantilever beams made from materials obeying the generalized Ludwick constitutive law." In: *Meccanica* 44 (2009), pp. 733–739.

[12] Richard H. Byrd, Jean Charles Gilbert, and Jorge Nocedal. "A Trust Region Method Based on Interior Point Techniques for Nonlinear Programming". In: *Mathematical Programming* 89.1 (2000), pp. 149–185.

[13] Hibbeler R. C. *Mechanics of Materials, 8th ed.* Pearson, New York, 2017, pp. 119–178.

[14] Chongjing Cao, Xing Gao, and Andrew T. Conn. "Soft Robotics: A Magnetically Coupled Dielectric Elastomer Pump for Soft Robotics (Adv. Mater. Technol. 8/2019)". In: *Advanced Materials Technologies* 4.8 (2019), p. 1900128.

[15] Guizhou Cao et al. "Model-based robust tracking control without observers for soft bending actuators". In: *IEEE Robotics and Automation Letters* 6.3 (2021), pp. 5175–5182.

[16] Jennifer C. Case, Edward L. White, and Rebecca K. Kramer. "Soft material characterization for robotic applications". In: *Soft Robotics* 2.2 (2015), pp. 80–87.

[17] Lisha Chen et al. "Design and modeling of a soft robotic surface with hyperelastic material." In: *Mechanism and Machine Theory* 130 (2018), pp. 109–122.

[18] John J. Craig. *Introduction to Robotics*. Pearson Prentice Hall, 2005.

[19] Ravinder S. Dahiya et al. "Tactile sensing—from humans to humanoids". In: *IEEE Transactions on Robotics* 26.1 (2010), pp. 1–20.

[20] Thiago Eustaquio Alves De Oliveira, Ana-Maria Cretu Cretu, and Emil M. Petriu. "Multimodal bio-inspired tactile sensing module". In: *IEEE Sensors Journal* 17.11 (2017), pp. 3231–3243.

[21] Cosimo Della Santina et al. "Dynamic control of soft robots interacting with the environment". In: *IEEE International Conference on Soft Robotics (RoboSoft)*. IEEE. 2018, pp. 46–53.

[22] Kahraman G Demir et al. "Computational and Experimental Design Exploration of 3D-Printed Soft Pneumatic Actuators". In: *Advanced Intelligent Systems* 2.7 (2020), p. 2000013.

[23] Julie Diani, Bruno Fayolle, and Pierre Gilormini. "A review on the Mullins effect". In: *European Polymer Journal* 45.3 (2009), pp. 601–612.

[24] R. S. Diteesawat et al. "Electro-pneumatic pumps for soft robotics". In: *Science Robotics* 6.51 (2021), eabc3721.

[25] Azadeh Doroudchi and Spring Berman. "Configuration Tracking for Soft Continuum Robotic Arms Using Inverse Dynamic Control of a Cosserat Rod Model". In: *IEEE International Conference on Soft Robotics (RoboSoft)*. IEEE. 2021, pp. 207–214.

[26] John C. Doyle, Bruce A. Francis, and Allen R. Tannenbaum. *Feedback control theory*. Courier Corporation, 2013.

[27] Alin Drimus et al. "Design of a flexible tactile sensor for classification of rigid and deformable objects". In: *Robotics and Autonomous Systems* 62.1 (2014), pp. 3–15.

[28] Dylan Drotman et al. "Application-driven design of soft, 3-D printed, pneumatic actuators with bellows". In: *IEEE/ASME Transactions on Mechatronics* 24.1 (2018), pp. 78–87.

[29] Khaled Elgeneidy, Niels Lohse, and Michael Jackson. "Bending angle prediction and control of soft pneumatic actuators with embedded flex sensors–a data-driven approach". In: *Mechatronics* 50 (2018), pp. 234–247.

[30] Yahya Elsayed et al. "Finite element analysis and design optimization of a pneumatically actuating silicone module for robotic surgery applications". In: *Soft Robotics* 1.4 (2014), pp. 255–262.

[31] Ronald S. Fearing. "Tactile sensing mechanisms". In: *The International Journal of Robotics Research* 9.3 (1990), pp. 3–23.

[32] A. C. Fischer-Cripps. *Introduction to Contact Mechanics.* Springer, New York, 2007.

[33] Jr Forney and G. David. "Minimal bases of rational vector spaces, with applications to multivariable linear systems". In: *SIAM Journal on Control* 13.3 (1975), pp. 493–520.

[34] Gene F. Franklin et al. *Feedback control of dynamic systems.* Vol. 4. Upper Saddle River: Prentice hall, 2002.

[35] Yang Gao et al. "Dielectric elastomer actuators based on stretchable and self-healable hydrogel electrodes". In: *Royal Society Open Science* 6.8 (2019), p. 182145.

[36] James Gareth et al. *An introduction to statistical learning: with applications in R.* Spinger, 2013.

[37] Thomas George Thuruthel et al. "Control Strategies for Soft Robotic Manipulators: A Survey". In: *Robotics and Autonomous Systems* 125 (2020), p. 103427.

[38] Giada Gerboni et al. "Feedback control of soft robot actuators via commercial flex bend sensors". In: *IEEE/ASME Transactions on Mechatronics* 22.4 (2017), pp. 1881–1888.

[39] Gregory J. Gerling and Geb W. Thomas. "The effect of fingertip microstructures on tactile edge perception". In: *First Joint Eurohaptics Conference and Symposium on Haptic Interfaces for Virtual Environment and Teleoperator Systems World Haptics Conference.* IEEE. 2005, pp. 63–72.

[40] Leila Gharavi, Mohammad Zareinejad, and Abdolreza Ohadi. "Dynamic Finite-Element analysis of a soft bending actuator". In: *Mechatronics* 81 (2022), p. 102690.

[41] Sushanta Ghuku and Kashi Nath Saha. "A review on stress and deformation analysis of curved beams under large deflection". In: *International Journal of Engineering and Technologies* 11 (2017), pp. 13–39.

[42] Kieran Gilday, Josie Hughes, and Fumiya Iida. "Sensing, actuating, and interacting through passive body dynamics: A framework for soft robotic hand design". In: *Soft Robotics* 10.1 (2023), pp. 59–173.

[43] Qinghua Guan et al. "Novel Bending and Helical Extensile/Contractile Pneumatic Artificial Muscles Inspired by Elephant Trunk". In: *Soft Robotics* 7.5 (2020), pp. 597–614.

[44] Seunghyun Han et al. "Use of deep learning for characterization of microfluidic soft sensors". In: *IEEE Robotics and Automation Letters* 3.2 (2018), pp. 873–880.

[45] Taimoor Hassan et al. "Finite-element modeling and design of a pneumatic braided muscle actuator with multifunctional capabilities". In: *IEEE/ASME Transactions on Mechatronics* 24.1 (2018), pp. 109–119.

[46] Bin He, Shuai Wang, and Yongjia Liu. "Underactuated robotics: a review". In: *International Journal of Advanced Robotic Systems* 16.4 (2019), pp. 284–297.

[47] Richard W. Hertzberg, Richard P. Vinci, and Jason L. Hertzberg. *Deformation and fracture mechanics of engineering materials.* John Wiley and Sons, 2010.

[48] Weiping Hu et al. "A structural optimisation method for a soft pneumatic actuator". In: *Robotics* 7.2 (2018), p. 24.

[49] Josie Hughes et al. "Sensorized phantom for characterizing large area deformation of soft bodies for medical applications". In: *IEEE International Conference on Soft Robotics (RoboSoft)*. IEEE. 2020, pp. 278–284.

[50] Josie Hughes et al. "Soft manipulators and grippers: a review". In: *Frontiers in Robotics and AI* 3 (2016), p. 69.

[51] Fumiya Iida and Cecilia Laschi. "Soft robotics: Challenges and perspectives". In: *Procedia Computer Science* 7.1 (2011), pp. 99–102.

[52] Nina G. Jablonski. *Skin: A natural history.* University of California Press, 2006.

[53] Sagar Joshi and Jamie Paik. "Pneumatic supply system parameter optimization for soft actuators". In: *Soft Robotics* 8.2 (2021), pp. 152–163.

[54] Jaewoong Jung et al. "Optically sensorized elastomer air chamber for proprioceptive sensing of soft pneumatic actuators". In: *IEEE Robotics and Automation Letters* 5.2 (2020), pp. 2333–2340.

[55] Tom Kalisky et al. "Differential pressure control of 3D printed soft fluidic actuators". In: *IEEE/RSJ International Conference on Intelligent Robots and Systems (IROS)*. IEEE. 2017, pp. 6207–6213.

[56] Manuel Keppler, Christian Ott Ott, and Alin Albu-Schäffer. "From underactuation to quasi-full actuation: Aiming at a unifying control framework for articulated soft robots". In: *International Journal of Robust and Nonlinear Control* 32.9 (2022), pp. 5453–5484.

[57] DongWook Kim, Myungsun Park, and Yong-Lae Park. "Probabilistic modeling and Bayesian filtering for improved state estimation for soft robots". In: *IEEE Transactions on Robotics* 37.5 (2021), pp. 1728–1741.

[58] Sangbae Kim, Cecilia Laschi, and Barry Trimmer. "Soft robotics: a bioinspired evolution in robotics". In: *Trends in Biotechnology* 31.5 (2013), pp. 287–294.

[59] Burak Kurkcu and Masayoshi Tomizuka. "Algebraic Control: Complete Stable Inversion with Necessary and Sufficient Conditions". In: *IEEE Transactions on Automatic Control* (2024 (Under revision)).

[60] Burak Kürkçü, Coşku Kasnakoğlu, and Mehmet Önder Efe. "Disturbance/uncertainty estimator based integral sliding-mode control". In: *IEEE Transactions on Automatic Control* 63.11 (2018), pp. 3940–3947.

[61] Cecilia Laschi et al. "Soft robot arm inspired by the octopus". In: *Advanced Robotics* 26.7 (2012), pp. 709–727.

[62] Kyungwoo Lee. "Large deflections of cantilever beams of non-linear elastic material under a combined loading". In: *International Journal of Non-Linear Mechanics* 37.3 (2002), pp. 439–443.

[63] Guozhen Li et al. "Skin-inspired quadruple tactile sensors integrated on a robot hand enable object recognition". In: *Science Robotics* 5.49 (2020), eabc8134.

[64] Sheng-Guan Lin and Jen-Yuan James Chang. "Enhanced Design of an Adaptive Anthropomorphic Finger through Integration of Modular Soft Actuators and Kinematic Modeling". In: *Robotics* 13.8 (2024), p. 116.

[65] Chih-Hsing Liu et al. "Topology Optimization Design and Experiment of a Soft Pneumatic Bending Actuator for Grasping Applications". In: *IEEE Robotics and Automation Letters* 7.2 (2022), pp. 2086–2093.

[66] Jianbin Liu et al. "Pneumatic soft arm based on spiral balloon weaving and shape memory polymer backbone". In: *Journal of Mechanical Design* 141.8 (2019), p. 082302.

[67] Amin Lotfiani et al. "Analytical modeling and optimization of a corrugated soft pneumatic finger considering the performance of pinch and power grasps". In: *Extreme Mechanics Letters* 44 (2021), p. 101215.

[68] Luc Marechal et al. "Toward a common framework and database of materials for soft robotics". In: *Soft Robotics* 8.3 (2021), pp. 284–297.

[69] Luca Massari et al. "A machine-learning-based approach to solve both contact location and force in soft material tactile sensors". In: *Soft Robotics* 7.4 (2020), pp. 409–420.

[70] Barbara Mazzolai et al. "Octopus-Inspired Soft Arm with Suction Cups for Enhanced Grasping Tasks in Confined Environments". In: *Advanced Intelligent Systems* 1.6 (2019), p. 1900041.

[71] Andrija Milojevic et al. "A novel simple, adaptive, and versatile soft-robotic compliant two-finger gripper with an inherently gentle touch". In: *Journal of Mechanisms and Robotics* 13.1 (2021), p. 011015.

[72] Stefano Mintchev et al. "A soft robot for random exploration of terrestrial environments". In: *IEEE International Conference on Robotics and Automation (ICRA)*. IEEE. 2018, pp. 7492–7497.

[73] Bobak Mosadegh et al. "Pneumatic networks for soft robotics that actuate rapidly". In: *Advanced functional materials* 24.15 (2014), pp. 2163–2170.

[74] Philip Moseley et al. "Modeling, design, and development of soft pneumatic actuators with finite element method". In: *Advanced Engineering Materials* 18.6 (2016), pp. 978–988.

[75] R. M. Murray, Z. Li, and S. S. Sastry. *A Mathematical Introduction to Robotic Manipulation*. CRC Press, Boca Raton, FL, 2017, pp. 234–241.

[76] Elizbar A. Nadaraya. "On Estimating Regression". In: *Theory of Probability and Its Applications* 9.1 (1964), pp. 141–142.

[77] Eduardo Navas et al. "Soft Grippers for Automatic Crop Harvesting: A Review". In: *Sensors* 21.8 (2021), p. 2689.

[78] Pham Huy Nguyen and Wenlong Zhang. "Design and computational modeling of fabric soft pneumatic actuators for wearable assistive devices." In: *Scientific Reports* 10.1 (2020), p. 9638.

[79] Jorge Nocedal and Stephen J. Wright. *Numerical Optimization*. Springer, 2006.

[80] O-larnnithipong Nonnarit and Armando Barreto. "Gyroscope drift correction algorithm for inertial measurement unit used in hand motion tracking". In: *IEEE Sensor Conference*. IEEE. 2016, pp. 1–3.

[81] Paul C. Painter and Michael M. Coleman. *Essentials of polymer science and engineering*. DEStech Publications, Inc., 2009.

[82] Yu Pang et al. "Epidermis microstructure inspired graphene pressure sensor with random distributed spinosum for high sensitivity and large linearity". In: *ACS Nano* 12.3 (2018), pp. 2346–2354.

[83] Wookeun Park, Seongmin Seo, and Joonbum Ba Ba. "Development of a sensorized hybrid gripper to evaluate grasping quality". In: *IEEE International Conference on Soft Robotics (RoboSoft)*. IEEE. 2019, pp. 149–154.

[84] Yong-Lae Park et al. "Hyperelastic pressure sensing with a liquid-embedded elastomer". In: *Journal of Micromechanics and Microengineering* 20.12 (2010), p. 125029.

[85] Kristin M de Payrebrune and Oliver M O'Reilly. "On constitutive relations for a rod-based model of a pneu-net bending actuator". In: *Extreme Mechanics Letters* 9 (2016), pp. 38–46.

[86] Panagiotis Polygerinos et al. "Soft robotics: Review of fluid-driven intrinsically soft devices; manufacturing, sensing, control, and applications in human-robot interaction". In: *Advanced Engineering Materials* 19.12 (2017), p. 1700016.

[87] Panagiotis Polygerinos et al. "Towards a soft pneumatic glove for hand rehabilitation". In: *IEEE/RSJ International Conference on Intelligent Robots and Systems*. IEEE. 2013, pp. 1512–1517.

[88] Elze Porte et al. "Characterization of Temperature and Humidity Dependence in Soft Elastomer Behavior". In: *Soft Robotics* 11.1 (2024), pp. 118–130.

[89] Kedar Potdar, Taher S. Pardawala, and Chinmay D. Dai. "A comparative study of categorical variable encoding techniques for neural network classifiers". In: *International Journal of Computer Applications* 175.4 (2017), pp. 7–9.

[90] Pietro Pustina, Cosimo Della Santina Santina, and Alessandro De Luca. "Feedback regulation of elastically decoupled underactuated soft robots". In: *IEEE Robotics and Automation Magazine* 7.2 (2022), pp. 4512–4519.

[91] Daniela Rus and Michael T Tolley. "Design, fabrication and control of soft robots". In: *Nature* 521.7553 (2015), pp. 467–475.

[92] Shankar Sastry. *Nonlinear systems: analysis, stability, and control*. Springer Science and Business Media, 2013, pp. 182–234.

[93] Andrew K. Schulz et al. "Elephant trunks use an adaptable prehensile grip". In: *Bioinspiration and Biomimetics* 18.2 (2023), p. 026008.

[94] David Siegel, Inaki Garabieta, and J. Hollerbach. "An integrated tactile and thermal sensor". In: *IEEE International Conference on Robotics and Automation (ICRA)*. IEEE. 1986, pp. 1286–1291.

[95] Erik H Skorina et al. "Adapting to flexibility: model reference adaptive control of soft bending actuators". In: *IEEE Robotics and Automation Letters* 2.2 (2017), pp. 964–970.

[96] Erik H Skorina et al. "Feedforward augmented sliding mode motion control of antagonistic soft pneumatic actuators". In: *IEEE International Conference on Robotics and Automation (ICRA)*. IEEE. 2015, pp. 2544–2549.

[97] Erik H Skorina et al. "Motion control of a soft-actuated modular manipulator". In: *2016 IEEE International Conference on Robotics and Automation (ICRA)*. IEEE. 2016, pp. 4997–5002.

[98] *Smooth-on/platinum-silicone*. https://www.smooth-on.com/category/platinum-silicone/. Accessed: 2023-09-07.

[99] Zhi Qiang Tang et al. "Model-based online learning and adaptive control for a "human-wearable soft robot" integrated system". In: *The International Journal of Robotics Research* 40.1 (2021), pp. 256–276.

[100] Zhiqiang Tang et al. "Meta-Learning-Based Optimal Control for Soft Robotic Manipulators to Interact with Unknown Environments". In: *IEEE International Conference on Robotics and Automation (ICRA)*. IEEE. 2023, pp. 982–988.

[101] Maxime Thieffry et al. "Control design for soft robots based on reduced-order model". In: *IEEE Robotics and Automation Letters* 4.1 (2018), pp. 25–32.

[102] Thomas George Thuruthel, Kieran Gilday, and Fumiya Iida. "Drift-free latent space representation for soft strain sensors". In: *IEEE International Conference on Soft Robotics (RoboSoft)*. IEEE. 2020, pp. 138–143.

[103] Thomas George Thuruthel et al. "Soft robot perception using embedded soft sensors and recurrent neural networks". In: *Science Robotics* 4.26 (2019), eaav1488.

[104] Thomas George Thuruthel et al. "Stable open loop control of soft robotic manipulators." In: *IEEE Robotics and Automation Letters* 3.2 (2018), pp. 1292–1298.

[105] Deepak Trivedi, Dustin Dienno, and Christopher D. Rahn. "Optimal, Model-Based Design of Soft Robotic Manipulators". In: *Journal of Mechanical Design* (2008), p. 091402.

[106] S. Emre Tuna. "Synchronization of linear systems via relative actuation". In: *Systems and Control Letters* 134 (2019), p. 104527.

[107] R. Valette et al. "The effect of viscosity, yield stress, and surface tension on the deformation and breakup profiles of fluid filaments stretched at very high velocities". In: *Journal of Non-Newtonian Fluid Mechanics* 263 (2019), pp. 130–139.

[108] Jiangbei Wang, Yanqiong Fei, and Wu Pang. "Design, modeling, and testing of a soft pneumatic glove with segmented pneunets bending actuators". In: *IEEE/ASME Transactions on Mechatronics* 24.3 (2019), pp. 990–1001.

[109] Tao Wang et al. "Parameter identification and model-based nonlinear robust control of fluidic soft bending actuators". In: *IEEE/ASME Transactions on Mechatronics* 24.3 (2019), pp. 1346–1355.

[110] Zhongkui Wang and Shinichi Hirai. "Chamber dimension optimization of a bellow-type soft actuator for food material handling". In: *IEEE International Conference on Soft Robotics (RoboSoft)*. IEEE. 2018, pp. 382–387.

[111] Zhongkui Wang, Keung Or, and Shinichi Hirai. "A dual-mode soft gripper for food packaging". In: *Robotics and Autonomous Systems* 125 (2020), p. 103427.

[112] Zhongkui Wang, Yuuki Torigoe, and Shinichi Hirai. "A prestressed soft gripper: design, modeling, fabrication, and tests for food handling". In: *IEEE Robotics and Automation Letters* 2.4 (2017), pp. 1909–1916.

[113] Geoffrey S. Watson. "Smooth regression analysis". In: *Sankhyā: The Indian Journal of Statistics, Series A* 26.4 (1964), pp. 359–372.

[114] Greg Welch and Gary Bishop. *An introduction to the Kalman filter*. 1995, pp. 127–132.

[115] G. Westling and R.S. Johansson. "Responses in glabrous skin mechanoreceptors during precision grip in humans." In: *Experimental Brain Research* 66 (1987), pp. 128–140.

[116] Bas Wijnen et al. "Open-Source Syringe Pump Library". In: *PLOS ONE* 9.9 (2014), e107216.

[117] James F. Wilson and U. Mahajan. "Flexible robot manipulators and grippers: Relatives of elephant trunks and squid tentacles". In: *Robots and Biological Systems: Towards a New Bionics?* (1993), pp. 475–494.

[118] James F. Wilson and U. Mahajan. "The mechanics and positioning of highly flexible manipulator limbs". In: *Journal of Mechanisms, Transmissions, and Automation in Design* 111.2 (1989), pp. 232–237.

[119] Matheus S Xavier, Andrew J Fleming, and Yuen K Yong. "Finite element modeling of soft fluidic actuators: Overview and recent developments". In: *Advanced Intelligent Systems* 3.2 (2021), p. 2000187.

[120] Matheus S Xavier, Andrew J Fleming, and Yuen Kuan Yong. "Nonlinear Estimation and Control of Bending Soft Pneumatic Actuators Using Feedback Linearization and UKF". In: *IEEE/ASME Transactions on Mechatronics* 27.4 (2022), pp. 1919–1927.

[121] Matheus S. Xavier, Andrew J. Fleming, and Yuen K. Yong. "Design and Control of Pneumatic Systems for Soft Robotics: A Simulation Approach". In: *IEEE Robotics and Automation Letters* 6.3 (2021), pp. 5800–5807.

[122] Zhexin Xie et al. "Octopus arm-inspired tapered soft actuators with suckers for improved grasping". In: *Soft Robotics* 7.5 (2020), pp. 639–648.

[123] S. Yahud et al. "Experimental validation of a tactile sensor model for a robotic hand". In: *Annual International Conference of the IEEE Engineering in Medicine and Biology Society*. IEEE. 2009, pp. 2300–2303.

[124] Youcan Yan et al. "Soft magnetic skin for super-resolution tactile sensing with force self-decoupling". In: *Science Robotics* 6.51 (2021), eabc8801.

[125] Wu-Te Yang, Bo-Hsun Chen, and Pei-Chun Lin. "A dual-arm manipulation strategy using position/force errors and Kalman filter". In: *Transactions of the Institute of Measurement and Control* 44.4 (2022), pp. 820–834.

[126] Wu-Te Yang, Motohiro Hirao, and Masayoshi Tomizuka. "Design, Modeling, and Parametric Analysis of a Syringe Pump for Soft Pneumatic Actuators". In: *IEEE International Conference on Advanced Intelligent Mechatronics(AIM)*. IEEE. 2023, pp. 317–322.

[127] Wu-Te Yang, Burak Kurkcu, and Masayoshi Tomizuka. "Optimized Design of a Soft Actuator Considering Force/Torque, Bendability, and Controllability via an Approximated Structure". In: *ASME Journal of Mechanical Design* 146.12 (2024), p. 123301.

[128] Wu-Te Yang, Hannah S. Stuart, and Masayoshi Tomizuka. "Mechanical Modeling and Optimal Model-based Design of a Soft Pneumatic Actuator". In: *IEEE International Conference on Soft Robotics (RoboSoft)*. IEEE. 2023, pp. 1–7.

[129] Wu-Te Yang and Masayoshi Tomizuka. "Design a Multifunctional Soft Tactile Sensor Enhanced by Machine Learning Approaches". In: *ASME Journal of Dynamic Systems, Measurement, and Control* 144.8 (2022), p. 081006.

[130] Wu-Te Yang et al. "Control of Soft Pneumatic Actuators with Approximated Dynamical Modeling". In: *IEEE International Conference on Robotics and Biomimetics (ROBIO)*. IEEE. 2023, pp. 1–8.

[131] Wu-Te Yang et al. "Nonlinear Modeling for Soft Pneumatic Actuators via Data-Driven Parameter Estimation". In: *IEEE/ASME International Conference on Advanced Intelligent Mechatronics (AIM)*. IEEE. 2024.

[132] Sina Youssefian, Nima Rahbar, and Eduardo Torres-Jara. "Contact behavior of soft spherical tactile sensors". In: *IEEE Sensors Journal* 14.5 (2013), pp. 1435–1442.

[133] Shadab Zaidi et al. "Actuation Technologies for Soft Robot Grippers and Manipulators: A Review". In: *Current Robotics Reports* (2021), pp. 1–15.

[134] Hongying Zhang et al. "Design and development of a soft gripper with topology optimization". In: *IEEE/RSJ International Conference on Intelligent Robots and Systems (IROS)*. IEEE. 2017, pp. 6239–6244.

[135] Qi Zhang et al. "A novel approach for flexible manipulator conducting screwing task based on robot–environment contact classification". In: *Proceedings of the Institution of Mechanical Engineers, Part C: Journal of Mechanical Engineering Science* 235.8 (2021), pp. 1357–1367.

[136] Yue Zhang et al. "Robust control of dielectric elastomer smart actuator for tracking high-frequency trajectory". In: *IEEE Transactions on Industrial Informatics* 20.1 (2023), pp. 224–234.

[137] Jianshu Zhou et al. "Design, Modeling, and Control of Soft Syringes Enabling Two Pumping Modes for Pneumatic Robot Applications". In: *EEE/ASME Transactions on Mechatronics* (2024).

[138] Kemin Zhou and John Comstock Doyle. *Essentials of robust control*. Vol. 104. Upper Saddle River, NJ: Prentice hall, 1998.

[139] Yitong Zhou and Haonan Li. "A scientometric review of soft robotics: Intellectual structures and emerging trends analysis (2010–2021)". In: *Frontiers in Robotics and AI* 9 (2022), p. 868682.

[140] Bowen Zhu et al. "Microstructured graphene arrays for highly sensitive flexible tactile sensors". In: *Small* 10.18 (2014), pp. 3625–3631.

[141] Renjie Zhu et al. "Soft Robots for Cluttered Environments Based on OrigamiAnisotropic Stiffness Structure (OASS) Inspired by DesertIguana". In: *Advanced Intelligent Systems* (2023), p. 2200301.

[142]   Zheming Zhuang et al. "Design and Manufacture of Pneumatically Actuated Flexible Hand". In: *International Conference on Control and Robotics Engineering (ICCRE)*. IEEE. 2022, pp. 16–20.